Structural characterization of membrane protein complexes by single-particle cryo-EM

Dissertation
zur Erlangung des Doktorgrades
der Naturwissenschaften

vorgelegt beim Fachbereich 14
Biochemie, Chemie, Pharmazie
der Johann Wolfgang Goethe - Universität
in Frankfurt am Main

von
Joana S. Sousa
aus Lissabon, Portugal

Frankfurt am Main (2019)
(D 30)

Vom Fachbereich 14 Biochemie, Chemie und Pharmazie der Johann Wolfgang Goethe – Universität als Dissertation angenommen.

Dekan: Prof. Dr. Clemens Glaubitz

1. Gutachter: Prof. Dr. Volker Dötsch

2. Gutachter: Prof. Dr. Werner Kühlbrandt

Datum der Disputation

Part of this work was published in the following articles:

Sousa, J. S., Mills, D. J., Vonck, J., & Kühlbrandt, W. (2016). Functional asymmetry and electron flow in the bovine respirasome. *Elife*, *5*, e21290.

Sousa, J. S., Calisto, F., Langer, J. D., Mills, D. J., Refojo, P. N., Teixeira, M., Kühlbrandt, W., Vonck, J. & Pereira, M. M. (2018). Structural basis for energy transduction by respiratory alternative complex III. *Nature communications*, *9*.

Sousa, J. S., D'Imprima, E., & Vonck, J. (2018). Mitochondrial respiratory chain complexes. In *Membrane Protein Complexes: Structure and Function* (pp. 167-227). Springer, Singapore.

Sousa, J. S., & Vonck, J. (2019). Respiratory supercomplexes III_2IV_2 come into focus. *Nature structural & molecular biology*, *26*(2), 87.

Table of contents

I. Summary

Electron microscopy (EM) demarcates itself from other structural biology techniques by its applicability to a large range of biological objects that spans from whole cells to individual macromolecules. In single-particle cryo-EM, frozen-hydrated samples, prepared by vitrification with liquid ethane, retain macromolecules in a medium that approximates their natural aqueous environment and that, in this way, preserves high-resolution structural information. Nonetheless, the sensitivity of biological specimens to the high-energy electron beam introduces restrictions on the total dose that can be used during imaging while avoiding significant radiation damage. Consequently, the signal-to-noise ratio attained in each individual image is very low, and structures with high-resolution detail must be recovered by averaging thousands of projections in random orientations. This is achieved through the use of image processing algorithms capable of aligning and classifying particle images through the evaluation of cross-correlation functions between each particle and a reference.

In recent years, several innovations took place in the field of single-particle cryo-EM, among which the development of direct electron detectors must be highlighted. Direct electron detectors have a better detective quantum efficiency (DQE) than both photographic film and CCD cameras, and offer a fast readout, compatible with the acquisition of movie stacks. Additionally, new image processing software has become available, with more sophisticated algorithms and designed to take advantage of the specific characteristics of the movies produced with direct electron detectors. These technological advances in both hardware and software catalyzed a revolution in single-particle cryo-EM, which is now routinely used for the determination of near-atomic structures. As a result, the range of macromolecules accessible to cryo-EM has increased drastically, as targets that were unsuitable before for imaging due to their small dimensions can now be adequately visualized and refined to high-resolution.

During my doctoral work, I have used single-particle cryo-EM to structurally characterize challenging membrane proteins, with a strong emphasis on protein

complexes from aerobic respiratory chains. In chapter I of this thesis, I present my results on the bovine respirasome, a mitochondrial supercomplex composed of complexes I, III and IV. Chapter II is dedicated to the analysis of the structure of alternative complex III (ACIII) from *Rhodothermus marinus*, a bacterial quinol:cytochrome *c*/HiPIP oxidoreductase unrelated to the canonical cytochrome bc_1 complex (complex III). In addition, in chapter III I describe the structure of KimA, a high-affinity potassium transporter that drives the transport of its substrate by using the energy stored in the form of a proton gradient. These three membrane proteins, with molecular weights ranging from 140 kDa to 1.7 MDa, illustrate the possibilities and limitations faced in single-particle cryo-EM.

The aerobic respiratory chain is responsible for the generation of a transmembrane difference of electrochemical potential that is then used by ATP synthase for the production of ATP or for driving solute transport over the membrane. They catalyze the transfer of electrons from a substrate, such as NADH or succinate, to molecular oxygen and use the chemical energy released in these redox reactions to drive the translocation of protons, or in some cases sodium ions, to the intermembrane space in mitochondria or the periplasm in bacteria.

In mitochondria, the respiratory chain is composed of four complexes: complex I (NADH:ubiquinone oxidoreductase), complex II (succinate dehydrogenase), complex III (cytochrome bc_1 complex) and complex IV (cytochrome *c* oxidase). While it was for a long time believed that these complexes existed as single entities in the membrane, the use of milder procedures for protein purification and analysis revealed that respiratory complexes associate into well-ordered structures, known as supercomplexes. These have been proposed to offer different structural and functional advantages that are still controversial, including substrate channeling, stabilization of individual complexes and reduction of reactive oxygen species (ROS) production. The most thoroughly studied respiratory supercomplex has been the respirasome, conserved in higher eukaryotes and composed of one copy of complex I, a complex III dimer and one complex IV. By single-particle cryo-EM analysis, I retrieved a 9 Å map of the

respirasome from *Bos taurus*, which allowed the accurate docking of atomic models of the three component complexes. The structure shows that complex III associates to the concave side of the membrane arm of complex I, while complex IV is located between the end of the complex I hydrophobic arm and complex III. Several defined protein-protein contacts are observed between the component complexes, which are mediated predominantly by supernumerary subunits and close to the membrane surfaces. The interactions established between complex I and complex III are extensive and may support the argument that the association of complex I into supercomplexes is required for the stabilization or even the biogenesis of this complex.

The respirasome map reported here displays a clear density for the iron-sulfur domain in one protomer of the obligatory complex III dimer, while in the other protomer this is not resolved, in good agreement with the large movement that the domain undergoes during electron transfer from quinol to cytochrome *c*. This structural asymmetry reflects the distinct functional states of the two protomers and advocates for a preferential catalysis of quinol oxidation in the respirasome by the inner protomer of complex III. Interestingly, the quinol-binding site of the inner, active protomer of complex III faces the quinone channel of complex I, which is approximately 11 nm away. Hence, our map suggests that in the respirasome diffusion of quinol from complex I to the closest quinol oxidation site is favored, providing new support for a kinetic advantage for respiratory supramolecular assemblies.

In bacteria, respiratory chains can differ significantly in composition and organization, and canonical complexes may be replaced or complemented by different enzymes with similar activity. This is the case for ACIII, a quinol:cytochrome *c*/HiPIP oxidoreductase structurally unrelated to the canonical cytochrome bc_1 complex. ACIII is widespread in bacteria and can integrate both respiratory and photosynthetic electron transfer chains. The *act* gene cluster is composed of six to eight genes, which encode one pentahemic and one monohemic *c*-type cytochrome (ActA and ActE, respectively), a large soluble subunit with binding sites for three [4Fe-4S] clusters and one [3Fe-4S] cluster (ActB, which in some cases is split into two smaller subunits, ActB1 and ActB2),

three integral membrane subunits with ten (ActC and ActF) or two (ActD) predicted transmembrane helices and one supernumerary subunit believed to span the membrane with one transmembrane helix (ActG). We have determined a 3.9 Å map of ACIII from *Rhodothermus marinus* by single-particle cryo-EM and modeled *de novo* seven of the eight subunits present in the complex, including a newly-identified subunit (ActH). In addition, a small population of particles was identified during 3D classification and refined into a 20 Å resolution map with a large density associated to the transmembrane domain of ACIII. This map was assigned to an ACIII-*caa₃* supercomplex, previously reported to exist in *Rhodothermus marinus* membranes.

ACIII is an L-shaped complex with a large periplasmic domain composed of ActA, ActB, ActE, ActH and an unknown small subunit, a transmembrane domain with 23 helices (10 of ActC, 10 of ActF, 2 of ActD and 1 of ActA), and a small cytoplasmic domain formed by the N- and C-terminal residues of ActC, ActD and ActF. The complex harbors a single quinol-binding site, located within ActC. In the periplasmic domain, six c-type hemes and four iron-sulfur clusters form two electron transfer wires that bifurcate from the [3Fe-4S] cluster in ActB. Together with the available biochemical data, our structure points to the [3Fe-4S] cluster as the primary electron acceptor, which oxidizes quinol to quinone. Electrons are then carried by the heme wire for reduction of one of the electron carriers (cytochrome c and HiPIP) or the caa_3 oxygen reductase. The energy released during oxidation of quinol by ACIII is sufficient to translocate up to four protons across the membrane, and two putative proton pathways were identified in the ACIII structure. This observation suggests that ACIII contributes to the transmembrane difference of electrochemical potential as a redox-driven proton pump.

Secondary active transporters energize the transport of their substrate through the dissipation of the electrochemical gradient of a co-substrate. KimA is a high-affinity potassium uptake system present in many bacteria and a member of the KUP/HAK/KT family of potassium secondary active transporters. Our biochemical characterization of KimA shows that this transporter operates in a proton-dependent manner and is regulated by the secondary messenger cyclic

di-AMP. Using single-particle cryo-EM and a detergent-free solubilization procedure by treatment with styrene-maleic acid (SMA) co-polymer, we determined the structure of KimA from *Bacillus subtilis* at 3.7 Å resolution. KimA is a homodimer with two membrane domains positioned at an angle of approximately 130° and a C-terminal cytoplasmic domain. Formation of the dimer is mediated by the soluble domains of each monomer, which are located below the transmembrane domain of the opposite monomer and that together form a continuous 10-stranded β-sheet enclosed by 8 α-helices. This cytoplasmic domain is proposed to bind cyclic di-AMP for inhibition of the transport, when in the presence of high concentrations of potassium ions.

The membrane domain of the KimA monomer is composed of 12 transmembrane helices, where the first ten adopt a typical LeuT fold in an inward-facing occluded state. Our structure allowed the identification of a putative potassium-binding site between transmembrane helices 1, 3, 6, 8 and 10, as well as of residues possibly responsible for the proton coupling.

The studies conducted during this doctorate on the respirasome and ACIII elucidate different strategies used for energy conservation, and emphasize the relevance of respiratory supercomplexes in both eukaryotes and prokaryotes. Further, the structure of KimA constitutes the first step towards the structural characterization of the large family of potassium transporters KUP/HAK/KT. Collectively, this work illustrates the invaluable contribution of single-particle cryo-EM to the study of membrane proteins.

II. Zusammenfassung

Die Elektronenmikroskopie (EM) unterscheidet sich von anderen Methoden der Strukturbiologie in ihrer Eignung für eine große Bandbreite biologischer Proben, von ganzen Zellen bis hin zu einzelnen Makromolekülen. In der Kryo-EM werden im Gebiet der Einzelpartikelanalyse durch Vitrifizierung Proben in einem Zustand festgehalten, der annähernd der natürlichen, wässrigen Umgebung der Makromoleküle entspricht, und auf diese Weise deren strukturelle Details in ihrer atomaren Auflösung konserviert. Dennoch limitiert die Empfindlichkeit biologischer Proben gegenüber einem Elektronenstrahl von hoher Energie und die daraus resultierenden Strahlungsschäden die maximal verwendbare Dosis, der ein solches Objekt während der Datenaufnahme ausgesetzt werden kann. Das in jedem einzelnen Bild erreichbare Signal-Rausch-Verhältnis ist daher sehr gering, so dass die Rekonstruktion hochaufgelöster Strukturen die Mittelung über Tausende von Projektionen zufälliger Orientierungen erfordert. Hierzu wird auf Algorithmen zurückgegriffen, die in der Lage sind, durch die Verwendung von Kreuzkorrelationsfunktionen zwischen den aufgenommen Partikeln und Referenzmodellen die Einzelabbildungen gegeneinander auszurichten und zu klassifizieren.

Aus einer Reihe technischer Innovationen im Gebiet der Einzelpartikel-Kryo-EM (in der Folge kurz Kryo-EM) innerhalb der letzten Jahre sticht die Entwicklung von Direktelektronendetektoren hervor. Diese Detektoren verfügen über eine bessere Effizienz bei der Quantendetektion als photographischer Film und CCD-Kameras, und bieten dazu eine hohe Auslesegeschwindigkeit, die die Aufnahme ganzer Serienbildstapel ermöglicht. Außerdem wurden neue Programme zur Datenanalyse entwickelt, die Algorithmen verwenden, die darauf zugeschnitten wurden, die besonderen Vorteile der Aufnahme solcher Bildstapel mittels Direktelektronendetektoren auszunutzen. Diese technologischen Fortschritte auf Software- wie auf Hardwareebene mündeten in einer Revolution in der Kryo-EM, die nunmehr häufig die Methode der Wahl ist bei der Aufklärung von Strukturen bis hin zu atomarer Auflösung. Zusätzlich ist das Spektrum der Makromoleküle, die für eine solche Analyse in Frage kommen, drastisch gestiegen, so dass sogar vormals wegen ihrer zu geringen Größe ungeeignete

Objekte zufriedenstellend abgebildet und mit sehr hoher Auflösung rekonstruiert werden können.

Während meiner Doktorarbeit habe mit Hilfe der Kryo-EM die Strukturen unterschiedlicher Membranproteine bestimmt, insbesondere Proteinkomplexe aerober Atmungsketten. In Kapitel I dieser Arbeit stelle ich meine Ergebnisse zum Respirasom aus *Bos taurus* vor, einem mitochondrialen Superkomplex bestehend aus den Komplexen I, III und IV. Kapitel II widmet sich der Strukturaufklärung des Alternativen Komplex III (ACIII) aus *Rhodothermus marinus*, einer bakteriellen Chinol:Cytochrom *c*/HiPIP-Oxidoreduktase ohne Verwandtschaft zum Cytochrom bc_1-Komplex (Komplex III). Schließlich beschreibe ich in Kapitel III dieser Dissertation die Struktur von KimA, einem hochaffinen Kaliumtransporter, dessen Substrattransport aus Energie angetrieben wird, die in Form eines Protonengradienten gespeichert ist. Diese drei Membranproteine mit molekularen Massen von 140 kDa bis 1,7 MDa illustrieren beispielhaft die Möglichkeiten und Grenzen der Kryo-EM.

Aerobe Atmungsketten sind verantwortlich für den Aufbau einer elektrochemischen Potenzialdifferenz über Membranen hinweg, die dann durch ATP-Synthasen für die Produktion von ATP oder als treibende Kraft für den Transport unterschiedlicher Stoffe durch Membranen dient. Sie katalysieren den Transfer von Elektronen von einem Substrat wie NADH oder Succinat auf molekularen Sauerstoff, und benutzen die durch diese Redoxreaktionen freiwerdende chemische Energie zur Überführung von Protonen oder in anderen Fällen Natriumionen in den Intermembranraum von Mitochondrien oder in das Periplasma bei Bakterien.

In Mitochondrien ist die Atmungskette aus vier Komplexen aufgebaut: Komplex I (NADH:Ubichinon-Oxidoreduktase), Komplex II (Succinat-Dehydrogenase), Komplex III (Cytochrom bc_1) und Komplex IV (Cytochrom *c*-Oxidase). Lange Zeit wurde angenommen, dass die Komplexe vereinzelt in der Membran vorkommen. Durch schonendere Methoden der Proteinaufreinigung und der Analytik wurde jedoch deutlich, dass die Atmungskettenkomplexe sich zu wohldefinierten Verbünden, sogenannten Superkomplexen, zusammenfügen. Noch stark

umstritten sind die dieser Anordnung zugeschriebenen, verschiedenen strukturellen und funktionalen Vorteile wie das *Substrate Channeling*, die Stabilisierung der einzelnen Komplexe und die Limitierung der Produktion reaktiver Sauerstoffspezies. Der am intensivsten erforschte respiratorische Superkomplex ist das sogenannte Respirasom, das in höheren Eukaryoten konserviert ist und aus Komplex I, einem Dimer von Komplex III und aus Komplex IV besteht. Durch Kryo-EM rekonstruierte ich vom Respirasom des Hausrinds *Bos taurus* eine Dichtekarte mit einer Auflösung von 9 Å, was das präzise Hineinsetzen atomarer Modelle von allen drei Einzelkomplexen ermöglichte. Die Struktur zeigt, dass sich Komplex III an die konkave Seite der Membrandomäne von Komplex I anfügt, während sich Komplex IV zwischen das Ende des hydrophoben Arms von Komplex I und Komplex III lagert. Diverse, spezifische Kontaktstellen zwischen den Einzelkomplexen beruhen auf direkte Proteinkontakte, die hauptsächlich durch zusätzliche Untereinheiten und nah der Membranoberfläche zustande kommen. Zwischen Komplex I und Komplex III sind solche Verbindungen zahlreich und stützen somit die Hypothese, dass die Ausbildung eines Superkomplexes für die Stabilisierung von Komplex I nötig ist, oder gar für seine Biogenese.

Die hier beschriebene Dichtekarte des Respirasoms zeigt deutlich die Eisen-Schwefel-Domäne in einem Protomer des Komplex III-Dimers, während sie im anderen Protomer nicht zu erkennen ist, was mit den großen Bewegungen übereinstimmt, die diese Domäne während des Elektronentransfers vom Chinol zum Cytochrom *c* durchläuft. Diese strukturelle Asymmetrie spiegelt die unterschiedlichen funktionellen Zustände der zwei Protomere wider und deutet auf eine vorwiegend im inneren Protomer von Komplex III stattfindende Katalyse der Chinoloxidation im Respirasom hin. Damit übereinstimmend zeigt die Chinol-Bindestelle des inneren, aktiven Protomers von Komplex III in die Richtung des Chinon-Kanals von Komplex I, der ungefähr 11 nm entfernt liegt. Folglich deutet unsere Dichtekarte darauf hin, dass der Aufbau des Respirasoms auf die Diffusion des Chinols vom Komplex I zur nächstgelegenen Chinoloxidationsstelle zugeschnitten ist, so dass auch aus kinetischen

Gesichtspunkten die Ausbildung respiratorischer Superkomplexe Vorteile mit sich bringt.

In Bakterien ist eine Vielfalt an Atmungsketten verschiedener Zusammensetzung vorzufinden, die vom typischen Aufbau stark abweichen, und in denen die Standardkomplexe durch Enzyme ähnlicher Aktivität ersetzt oder ergänzt werden. Dies ist der Fall bei ACIII, einer alternativen Chinol:Cytochrom c/HiPIP-Oxidoreduktase, die strukturell nicht verwandt ist mit dem Cytochrom bc_1-Komplex. ACIII ist in Bakterien weit verbreitet und kann Bestandteil sowohl respiratorischer als auch photosynthetischer Elektronentransferketten sein. Der *act*-Gencluster besteht aus sechs bis acht Genen, welche für je ein Cytochrom c mit fünf bzw. einer Häm-Gruppe (ActA bzw. ActE) kodieren, einer großen, löslichen Untereinheit mit Bindestellen für drei [4Fe-4S]-Cluster und ein [3Fe-4S]-Cluster (ActB, welches in manchen Fällen auf zwei kleinere Untereinheiten ActB1 und ActB2 aufgeteilt ist), drei Membranproteinunter-einheiten mit zehn (ActC und ActF) oder zwei (ActD) vorhergesagten Transmembranhelices, und in einigen Fällen eine zusätzliche Untereinheit, von der angenommen wird, dass sie eine Transmembranhelix besitzt (ActG). Wir haben eine Dichtekarte von 3,9 Å Auflösung von ACIII aus *Rhodothermus marinus* durch Kryo-EM rekonstruiert, und eine Struktur mit sieben der acht Untereinheiten des Komplexes, einschließlich einer zuvor unbekannten Untereinheit (ActH), *de novo* gebaut. Außerdem entdeckten wir im Zuge der 3D-Klassifizierung eine kleinere Gruppe an Partikeln, deren Dichtekarte bis zu einer Auflösung von 20 Å rekonstruiert werden konnte. In ihr schloss sich an die Transmembrandomäne von ACIII ein großer Bereich an zusätzlicher Dichte an, so dass diese Partikel als ACIII-caa_3-Superkomplexe identifiziert wurden, von deren Existenz in *Rhodothermus marinus* bereits berichtet worden war.

ACIII ist ein Komplex in der Form eines L, bestehend aus einer großen, periplasmatischen Domäne, die aus ActA, ActB, ActE und ActH sowie aus einer unbekannten, kleinen Untereinheit zusammengesetzt ist, einer Transmembran-domäne mit 23 Helices (10 von ActC, 10 von ActF, 2 von ActD und 1 von ActA) sowie einer kleinen, cytoplasmatischen Domäne, die von den N- und C-terminalen Resten von ActC, ActD und ActF gebildet wird. Im Komplex befindet

sich innerhalb von ActC seine einzige Chinol-Bindestelle. In der periplasmatischen Domäne bilden sechs *c*-Typ-Häme und vier Eisen-Schwefel-Cluster zwei Pfade zum Elektronentransfer aus, die sich ab dem [3Fe-4S]-Cluster in ActB aufspalten. Zusammen mit den biochemischen Daten deutet unsere Struktur darauf hin, dass das [3Fe-4S]-Cluster als der erste Elektronenakzeptor derjenige ist, der Chinol zu Chinon oxidiert. Die Elektronen werden dann entlang des Häm-Pfads geleitet, um einen der Elektronentransporter (Cytochrom *c* und HiPIP) oder die *caa*₃-Sauerstoff-Reduktase zu reduzieren. Die bei der Oxidation von Chinol durch ACIII freiwerdende Energie reicht aus, um bis zu vier Protonen über die Membran zu befördern, und zwei potentielle Kanäle für die Protonen wurden innerhalb der ACIII-Struktur ausgemacht. Diese Beobachtung legt die Vermutung nahe, dass ACIII eine redox-angetriebene Protonenpumpe ist.

Sekundär-aktive Transporter ziehen die für ihren Substrattransport nötige Energie aus seiner Kopplung an die Bewegung eines Ko-Substrates in Richtung des Gefälles dessen elektrochemischen Gradienten. KimA ist ein hochaffines System zur Kaliumaufnahme in vielen Bakterien und gehört zur KUP/HAK/KT-Familie der sekundär-aktiven Kaliumtransporter. Unsere biochemische Charakterisierung von KimA zeigt, dass dieser Transporter protonenabhängig funktioniert und durch den *Second Messenger* zyklisches di-AMP reguliert wird. Mit Hilfe der Kryo-EM und einer Detergens-freien Solubilisierungsmethode, der Behandlung mit Styrol-Maleinsäure-(SMA)-Kopolymeren, konnten wir die Struktur von KimA aus *Bacillus subtilis* zu einer Auflösung von 3,7 Å bestimmen. KimA ist ein Homodimer, das aus einer cytoplasmatischen Domäne und zwei Membrandomänen besteht, die in einem Winkel von ca. 130° zueinander stehen. An der Bildung des Dimers sind maßgeblich die löslichen Bereiche beider Monomere beteiligt, welche unterhalb der Membrandomäne des jeweils anderen Monomers ineinander verschränkt angeordnet sind, und zusammen ein durchgehendes 10-strängiges β-Faltblatt, umgeben von 8 α-Helices, ausbilden. Es wird vermutet, dass zyklisches di-AMP an diese cytoplasmatische Domäne bindet und den Transport inhibiert, sobald hohe Konzentrationen an Kaliumionen vorliegen.

Im KimA-Monomer besteht die Membrandomäne aus 12 Transmembranhelices, von denen die ersten zehn eine typische LeuT-Faltung in einem *inward-facing occluded-state* genannten Zustand annehmen. Unsere Struktur erlaubte uns die Identifizierung einer möglichen Kaliumbindestelle zwischen den Transmembranhelices 1, 3, 6, 8 und 10, sowie der möglicherweise für die Kopplung an den Protonentransport verantwortlichen Reste.

Die während dieser Doktorarbeit durchgeführte Forschung am Respirasom und an ACIII zeigen verschiedene Strategien der Energiespeicherung auf, und unterstreichen die Bedeutung von respiratorischen Superkomplexen sowohl in Eukaryoten als auch Prokaryoten. Zusätzlich dazu stellt die Struktur von KimA den ersten Schritt dar auf dem Weg hin zu einer strukturellen Charakterisierung einer großen Familie der Kaliumtransporter, KUP/HAK/KT. Insgesamt veranschaulicht diese Arbeit den unermesslichen Beitrag der Kryo-EM bei der Erforschung von Membranproteinen.

1. INTRODUCTION

The expression "seeing is believing" clearly illustrates how humans are a visual-centric species. Accordingly, also in science direct visual input is extremely valuable. In the field of structural biology, complex biological processes are investigated by "looking" at the molecular structure of proteins, RNA and DNA, as their function closely relates with a specific three-dimensional arrangement. Three major techniques are used for the structural analysis of biological macromolecules: nuclear magnetic resonance (NMR), x-ray crystallography and electron microscopy (EM; Figure 1). EM can be used to visualize structures within a wide scale range, from small macromolecular assemblies to cell components. Modern cryo-EM techniques include electron tomography (and subtomogram averaging), electron crystallography, micro-electron diffraction (micro-ED), helical reconstruction and single-particle analysis.
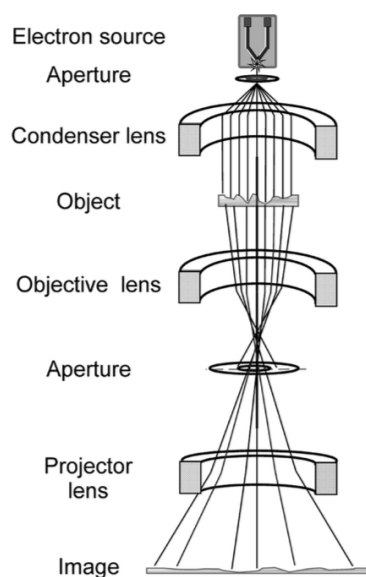
Figure 1. Schematic representation of an electron microscope. Standard electron sources include tungsten filaments, LaB_6 crystals and field emission guns (FEG), where the latter provides the most coherent and brightest beam. The electrons are then accelerated through voltages of 100 to 300 kV (wavelengths from 3.7 to 2 pm, respectively) and converted into a parallel beam by the condenser lenses. The image formed upon incidence of the electron beam in the sample is further magnified by the objective and projector lenses, before being recorded on photographic film or a digital camera. Reproduced with permission from Orlova et al. (2011). Copyright © 2011 American Chemical Society.

1.1. Electron microscopy in structural biology

After the development of the first electron microscope in the 1930's (Ruska, 1987), it quickly became evident that imaging of biological specimens presented several challenges. A major problem concerned the preservation of a hydrated sample under the high vacuum in the electron column. This was first addressed in the negative-staining method, where the sample is embedded in a layer of heavy metal salts, such as uranium, molybdenum or tungsten (Brenner and Horne, 1959). Negative-staining enhances contrast substantially and allows a quick assessment of the protein's dimensions and shape and sample's homogeneity, and is still largely used today in the initial stages of sample optimization. However, the technique only reveals the solvent-excluding surface and it is limited to low resolution, correlated with the grain size of the stain. A later method used embedment in glucose, a non-volatile medium that approximates the natural aqueous environment of biological specimens (Unwin and Henderson, 1975). While this approach preserves high-resolution detail, the attained contrast is very low as the scattering density of glucose approximates the one of proteins. For this reason, it is virtually impossible to use glucose embedding for imaging of individual particles and the method was restricted to studies with 2D crystals. A better alternative entailed the preparation of frozen-hydrated samples, which would prevent specimen collapse while preserving high-resolution structural information and provide an improved contrast while imaging the biological object itself, and not a contrasting agent. Attempts to freeze biological samples with liquid nitrogen lead to the formation of ice crystals, which damage the macromolecules and strongly diffract electrons, obscuring the signal of the biological material. In the early 1980's, Dubochet and co-workers established a method that allowed biological samples to be trapped in a thin film of vitreous ice upon rapid freezing with liquid ethane or propane (Adrian et al., 1984; Dubochet et al., 1988). This method was a groundbreaking development in the field and today is used routinely (see 1.4.1. Sample preparation).

A second major obstacle in the study of biological material by EM regards radiation damage by the high-energy electron beam, and the consequent low

dose – and signal-to-noise ratio (SNR) – of an individual image. Cooling of the specimen with liquid nitrogen or helium reduces this effect (Fujiyoshi, 1998; Stark et al., 1996), but visualization of high-resolution structural information is only possible through averaging over multiple copies of the same object. Such a strategy can be accomplished with crystals, where the signal of thousands of orderly packed, identical proteins compensates for the damage suffered by individual molecules. Using electron crystallography, Henderson and collaborators showed for the first time that structures at atomic resolution can be obtained with an EM by imaging 2D crystals with low doses and combining the phases from the images with the amplitudes from the diffraction pattern (Henderson et al., 1990). Several atomic structures were produced using this method (Kühlbrandt et al., 1994; Murata et al., 2000; Nogales et al., 1998), but the difficulties associated with the growth of good quality 2D crystals hindered a broader use of the technique. As an alternative, Frank proposed that by computationally aligning and merging images of many identical, single macromolecules the SNR can be equally enhanced, with no need for crystallization (Frank, 1975); the alignment of images of unstained and non-crystalline particles, with very low SNR, was the ultimate obstacle to recover high-resolution structural data from isolated particles. Frank showed that these low-dose images could be aligned to high accuracy by cross-correlation functions (Frank, 1975) and, together with Marin van Heel, developed a method for classification based on orientation and structural features (van Heel and Frank, 1981). Collectively, these developments created the framework for cryo-EM single-particle analysis.

Notwithstanding the short wavelength of electrons (2 pm at 300 kV), which in theory would allow imaging at very high resolutions, many other factors hamper the achievable resolution when imaging biological specimens. Apart from the radiation damage that builds up during the exposure of the sample to the electron beam and low SNR, the specimen also undergoes movements when irradiated, which blur the image. Beam coherence and spherical and chromatic aberrations are also important, specific to the microscope. Other limiting factors can be minimized by an appropriate microscope alignment, such as the

astigmatism resulting from an asymmetry in the electromagnetic field from the lenses and the coma originating from beam tilt (Orlova and Saibil, 2011). From a computational point of view, resolution is limited by the accuracy of alignment of individual images and the capability to classify the particles according to compositional and conformational variability in heterogeneous samples. Despite the potential of single-particle cryo-EM, for several decades these practical challenges largely limited the determination of atomic structures and restricted the method to the analysis of large macromolecules. Recent advances included the development of direct electron detectors (see 1.3. Direct electron detectors) and of new processing algorithms (see 1.4.3. Image processing) as well as automation (see 1.4.2. Data collection). These technological innovations drastically changed the scenario and elevated single-particle cryo-EM to a position that rivals today x-ray crystallography. The method impacted profoundly on the study of integral membrane proteins; since the first structure of the TRPV1 ion channel at 3.4 Å obtained in 2013 (Cao et al., 2013a; Liao et al., 2013) the number of near-atomic structures of membrane proteins determined by single-particle cryo-EM has grown rapidly, accounting for more than 28% of those released in 2018. The resolutions achieved also continue to improve, with the best maps of soluble protein complexes reaching now 1.65 Å (Zivanov et al., 2018).

1.2. Image formation in electron microscopy

In transmission electron microscopy (TEM), a 2D projection of the object is formed by interaction of the electrons emitted by the electron source with the sample (Figure 2). This image is then magnified by a series of electromagnetic lenses. The electrons that do not interact with the specimen and, therefore, are not deflected are said to be unscattered. On the other hand, each incident electron that interacts with the sample is scattered either elastically, meaning without energy loss, or inelastically, when energy is transferred from the electron to the sample. The ratio between inelastic and elastic scattering depends primarily on the atomic number of the atoms, with more inelastic
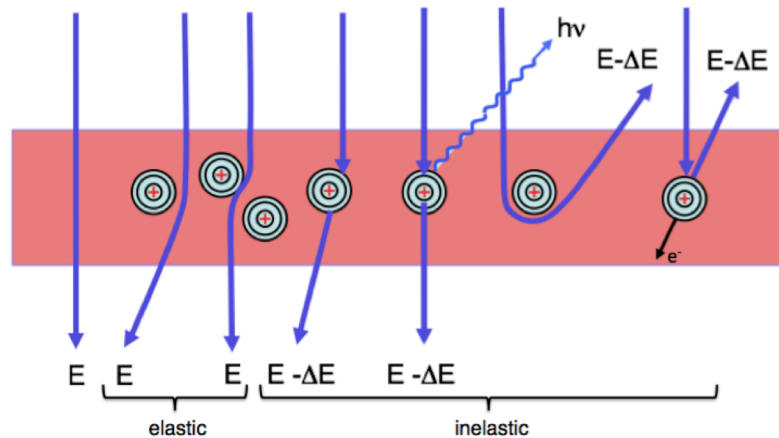
Figure 2. Schematic representation of the nature of the interactions between electrons and the specimen. Reproduced with permission from Werner Kühlbrandt's lecture notes.

events taking place when imaging light atoms that compose biological material (Glaeser, 2016). Elastic events provide most of the constructive image information, while inelastic events contribute to noise and alter the structure of the specimen, resulting in what is known as radiation damage. Inelastic scattering cannot be suppressed, but different strategies are in place to reduce its undesirable effects on the image, including the use of apertures that prevent electrons scattered at high angles from reaching the image plane and energy filters that selectively remove electrons of lower energy, by taking advantage of the fact that electrons with different wavelength can be deflected along different paths. To contribute to the image productively an electron must also be deflected only once and so multiple scattering events must be reduced by use of higher voltages and thinner samples (Glaeser, 2016). The thickness of the sample is equally restricted by the penetration of the beam into the specimen and, when aiming for high resolution, by the beam depth of focus (focus gradient along the z-axis) (Zhang and Zhou, 2011).

Despite the high percentage of inelastic events generated by biological samples, these rarely absorb electrons and for this reason produce very low amplitude contrast (Orlova and Saibil, 2011). Simultaneously, these specimens are weak phase objects; that is to say, they are weak electron scatters and the phase shift introduced in electrons elastically deflected is also very small. To increase

contrast, a phase shift between unscattered and scattered electrons must be induced, which converts the imperceptible phase contrast into amplitude contrast (Figure 3). Such phase shift is produced by the lens aberrations and by the image defocus (distance of the image plane to the true focal plane) that can be adjusted to produce the desired contrast (Frank, 2006).

Due to the microscope aberrations and the use of defocus to enhance contrast (Figure 4a,b), the TEM images are 2D projections of the object convoluted by a contrast transfer function (CTF). The CTF is a frequency-dependent sine function that modulates both amplitudes and phases, determining for each frequency whether the contrast is positive, negative or zero. Most of the parameters that define the CTF of an image are characteristic of the microscope (lens aberration, beam coherence, mechanical instabilities, among others), with exception of the image defocus. Higher defocus values increase the frequency of the oscillations in the CTF (Figure 4c) and, therefore, by combining images with different defoci the information at the zeros of the function is recovered in the final reconstruction. The CTF is also dampened towards high-resolution frequencies in a
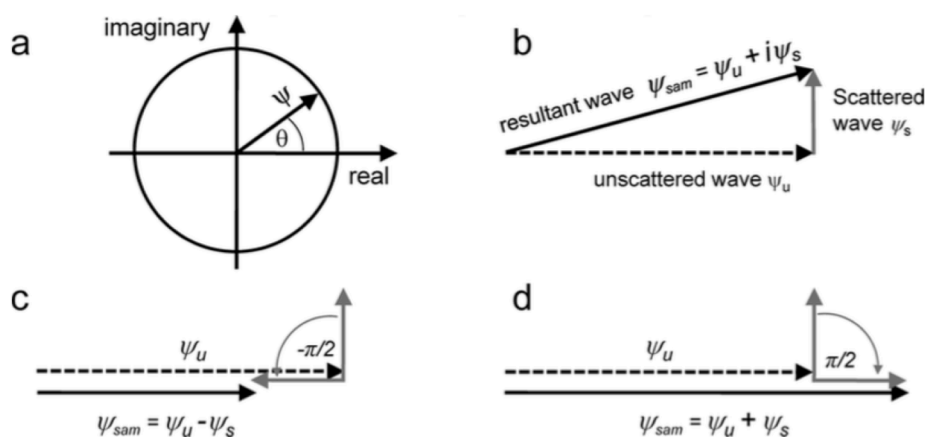
Figure 3. Graphical representation of phase contrast. **(a)** Complex plane representation of a wave vector Ψ with phase θ. **(b)** Vector representation illustrating the small difference in amplitude between the unscattered (Ψ_u) and the transmitted (Ψ_{sam}) waves. **(c)** Vector representation of negative phase contrast and **(d)** positive phase contrast, where the scattered wave undergoes a $\pm\pi/2$ phase shift that decreases or increases, respectively, the amplitude of the resultant wave. Reproduced with permission from Orlova et al. (2011). Copyright © 2011 American Chemical Society.
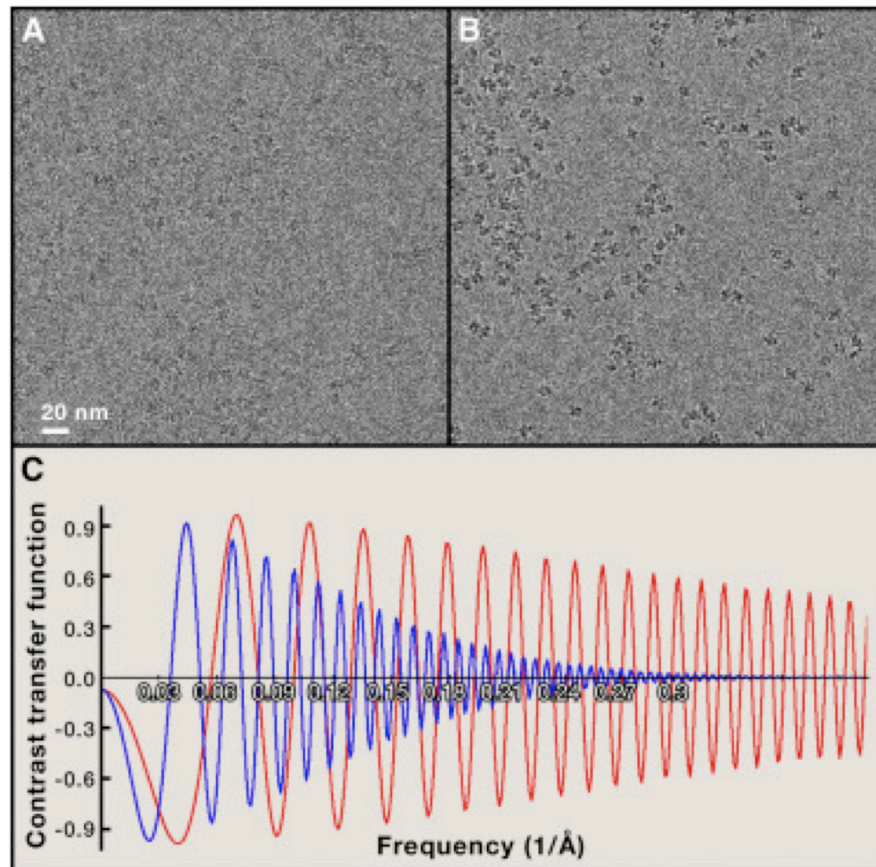
Figure 4. Effect of defocus on image contrast and CTF. **(a, b)** Images of human transferrin receptor at 1.2 μm and 3.0 μm, respectively. **(c)** Simulated CTF at a defocus of 1.2 μm (red) and 3.0 μm (blue), with an acceleration voltage of 200 kV and angular spread of 0.07 mrad. Reproduced with permission from Cheng (2015). Copyright © 2015 Elsevier Inc.

defocus-dependent manner due to the partial coherence of the beam and its energy spread. To restore the true projection of the object, the effects of the CTF must be reversed; the CTF is determined from the microscope parameters and the defocus estimated from the image (see 1.4.3. Image processing). Nonetheless, the accuracy to which the defocus can be estimated is limited, with small errors becoming significant at high frequencies, and ultimately the CTF will determine the attainable resolution. For this reason, the defocus range used during data collection must be carefully selected in order to enhance the contrast while being able to recover the signal at high-resolution frequencies.

1.3. Direct electron detectors

The performance of any given electron detector can be rated by three parameters: the modulation transfer function (MTF), which echoes the ability to conserve contrast at a given frequency; the noise power spectrum (NPS), which correlates with the transmission of input noise at different frequencies; and the detective quantum efficiency (DQE), an overall measure of the detector's efficiency that reflects how much the original signal is degraded by noise added during signal transduction and that is defined as the ratio between the SNR of the output and input signals (McMullan et al., 2016). Optimization of the latter is critical in cryo-EM methods, in which imaging is done with very low doses and SNR is low. Before the development of direct electron detectors, photographic film composed of silver halide crystals embedded in a gelatin matrix was the preferred electron detector in EM, with a DQE of 30-35% at half Nyquist (half of the maximum spatial frequency, also known as Nyquist frequency and defined as the reciprocal of twice the pixel size) (McMullan et al., 2009a). The use of film introduced several laborious and rate-limiting steps, related to the transfer of water-adsorbed films into the microscope vacuum and the need for developing, fixing, drying and digitizing them.

Digital detectors were first used in electron microscopes in the 1990's, in the form of charge-coupled devices (CCD; Figure 5a) (Krivanek and Mooney, 1993). Since CCDs are damaged by direct incidence of electrons, a phosphor scintillator is used to convert electrons to photons, which are then transmitted by fiber optics to the CCD and translated into an electrical charge and electronic signal. The images obtained with CCDs are degraded by the noise added during electron-to-photon conversion, where one electron event is delocalized in a photon "cloud", and by electron scattering in the scintillator. Therefore, even though these devices allow high image throughput and an immediate assessment of sample and image quality, they perform poorly at high frequencies and increasing voltages, with a DQE of only 7-10% at half Nyquist, at 300 kV (McMullan et al., 2009a).

Direct electron detectors (Figure 5a), also known as direct detection devices (DDD), became commercially available in 2012. They were unquestionably the key to the resolution revolution that took place in single-particle cryo-EM, as their benefits far surpass a simple improvement in DQE. Direct electron detectors are radiation-hard and implement metal-oxide-semiconductor (CMOS) technology, where each pixel contains a photo detector and amplifier, allowing fast readout (Booth and Mooney, 2013; McMullan et al., 2016). The electrons are detected directly and with high precision by a silicon-doped monolayer. Furthermore, electron backscattering is substantially reduced by backthinning of the sensor (Figure 5b). These advances contribute to the better DQE of direct electron detectors, which exceeds that of film at all spatial frequencies (McMullan et al., 2014).

Imaging with direct electron detectors can be performed in two modes. In integrating mode, the overall energy deposited in each pixel throughout the exposure is read out to provide the image. However, the energy deposited by
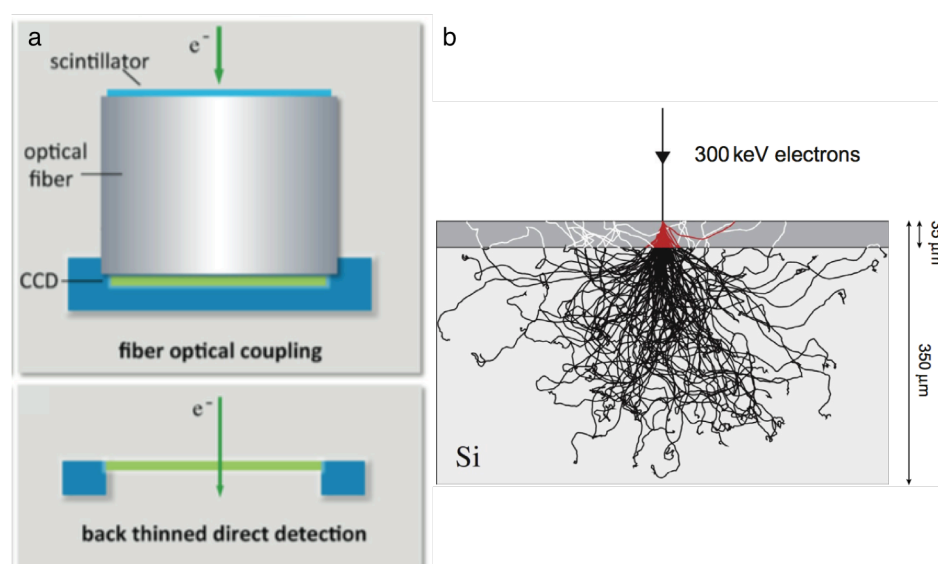
Figure 5. (a) Comparison between a CCD camera (top) and a direct electron detector (bottom). **(b)** Schematic of 300 kV electron trajectories in silicon that contribute to the recorded signal before (white tracks) and after (red tracks) backthinning. Adapted from Booth et al. (2013) and reproduced from McMullan et al. (2009) with permission. Copyright © 2013 John Wiley & Sons, Ltd. and © 2009 Elsevier B.V.

each electron can vary substantially, limiting the DQE of the cameras operating in this way. In counting mode (Figure 6), each primary electron event is registered individually in a frame, assigned to a single pixel by evaluating the charge distribution among adjacent pixels and replaced by an idealized single count. This approach reduces noise and improves DQE several fold. To avoid coincidence loss, when two or more electrons hit one pixel or adjacent pixels within one frame and are registered as a single event, imaging is done at low electron fluxes and high frame rates. Some cameras can also operate in super-resolution mode (Figure 6), when the point of impact for an incident electron can be determined to subpixel accuracy, practically reducing the Nyquist frequency to half of that imposed by the physical pixel size of the detector.
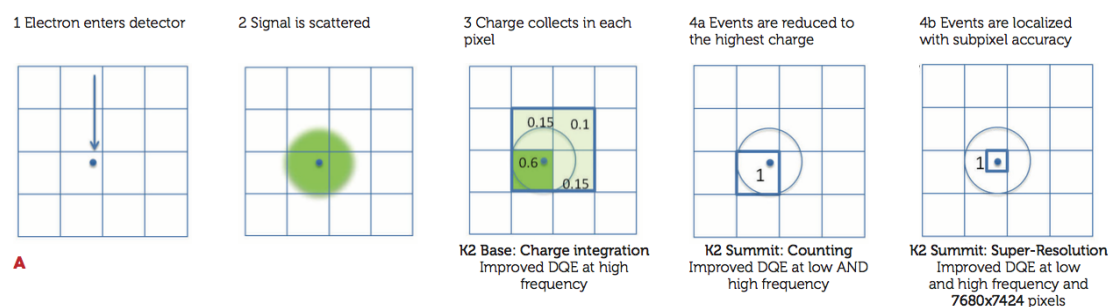
Figure 6. Schematic representation of electron detection in counting and super-resolution modes. Adapted with permission from Booth et al. (2013). Copyright © 2013 John Wiley & Sons, Ltd.

Additionally, the fast readout of these cameras allows to record each micrograph as a movie stack. The usage of movies in single-particle cryo-EM drove several developments in image processing, e.g. for correction of beam-induced motion and consequent minimization of image blurring (Bai et al., 2013; Brilot et al., 2012; Li et al., 2013) and for reduction of noise introduced by radiation damage while maximizing dose (Grant and Grigorieff, 2015a; Scheres, 2014) (see 1.4.3.1. Movie pre-processing).
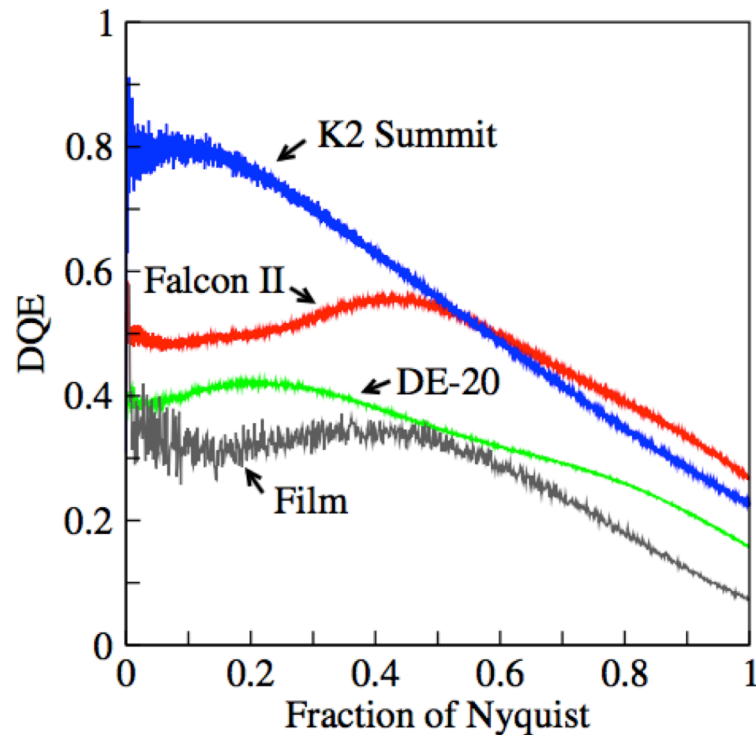
Figure 7. DQE plots for several of the commercially available electron detectors. Reproduced with permission from McMullan et al. (2014). Copyright © 2014 Elsevier B.V.

Currently available direct electron detectors include: the Falcon cameras I, II and III, the first two of which are restricted to integrating mode, while the latter can be used in either integrating or counting modes; the K2 Summit and K3 IS cameras that are mostly used in counting mode; and the DE-20 and DE-64 that operate in integrating or counting mode, respectively (Figure 7).

1.4. Single-particle cryo-EM

1.4.1. Sample preparation

In the initial stages of a project, samples of purified protein are screened by negative-stain electron microscopy (Ohi et al., 2004). This quick and inexpensive strategy permits the identification of suitable samples for high-resolution structural analysis, meaning a protein preparation that is stable, monodisperse and free of aggregates. In this method, a droplet of protein solution is applied to

a carbon-coated copper grid and embedded in a heavy metal salt solution, which is then blotted to a thin film (Figure 8a). To hydrophilize the carbon film and allow the aqueous solution to spread, the grid is glow-discharged, where air is ionized at low-pressure, rendering the film surface negatively charged. The most commonly used stain is uranyl acetate due to its high contrast and high stability during storage over long periods. Nevertheless, since stains are not inert, specific cases may require other stains with different charge, pH or grain size, e.g. uranyl formate or ammonium molybdate. Negative-staining data can also be processed into a first 3D reconstruction, which may be used as an initial model during structure determination by cryo-EM. However, one must be aware of possible distortions in negatively-stained structures, which result from flattening or incomplete stain embedding.

Cryo-EM specimens are prepared by the vitrification procedure developed by Dubochet and colleagues (Adrian et al., 1984; Dubochet et al., 1988). In this method, 3 to 4 µl of protein solution are applied to a grid covered by a holey carbon or gold film, blotted to a thin film sustained over the holes by surface tension forces and quickly plunged into a liquid cryogen, such as ethane or propane (Figure 8b). As the cryogen has a high heat capacity and is kept close to its freezing temperature by cooling with liquid nitrogen, and the film thickness is reduced to less than 3 µm, the sample is cooled by approximately 200 K in less then 10^{-4} seconds, reaching the cooling rates required to freeze water in an amorphous state. As for negative-staining, the grid must be rendered hydrophilic by glow discharge or by a specific plasma treatment, where defined gas mixtures like argon:oxygen are used instead of air (Passmore and Russo, 2016).

Several plungers are commercially available for freezing of cryo-EM grids, which are operated manually or semiautomatically and with which a series of parameters are controlled for reproducibility, e.g. temperature, humidity, blotting time and blotting force. However, preparation of cryo-EM grids still largely depends on user expertise and is highly variable. For this reason, efforts towards completely automated plungers have been taken in recent years (Razinkov et al., 2016). Moreover, several strategies can be employed with the
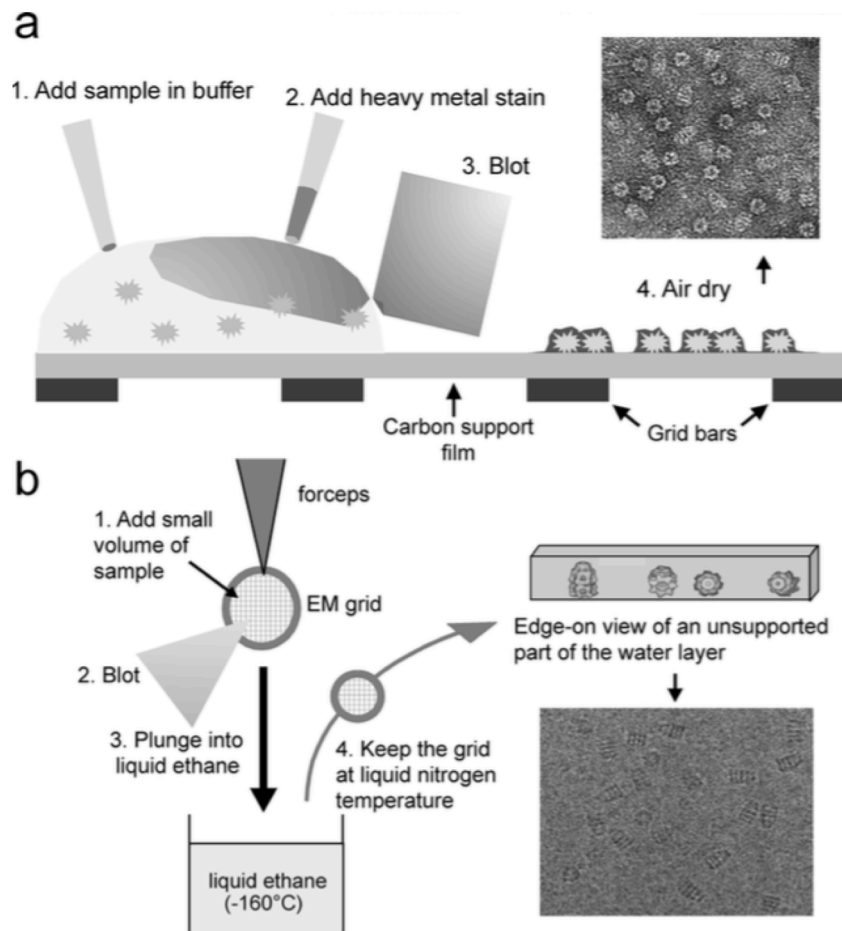
Figure 8. Preparation of specimens for **(a)** negative-staining EM and **(b)** cryo-EM. Reproduced with permission from Orlova et al. (2011). Copyright © 2011 American Chemical Society.

plungers to freeze the sample in different time frames and achieve what is known as time-resolved cryo-EM.

Different types of grids can be used in cryo-EM that may vary in the type of mesh, hole array and in the support material. The most widely used grids are composed of a copper mesh that supports a perforated carbon foil. As an alternative, grids where both the mesh and the foil are made of gold have become increasingly popular due to improved stability and reduced beam-induced movement during imaging (Russo and Passmore, 2014). The holes in the foil may be of an undefined shape and size as in lacey carbon, or circular and elliptical, in several sizes and arranged according to a regular or irregular array.

Preparation of an ideal cryo-EM specimen requires optimization of several parameters; the most critical are thickness of the aqueous film and particle distribution and orientation (Orlova and Saibil, 2011; Passmore and Russo, 2016). In order to ensure maximum contrast, the ice layer should be only slightly thicker than the longest axis of the protein but not too thin, as this would exclude the particles from the ice or induce preferred orientations. Ice thickness can be optimized by adjusting blotting conditions, but also through plasma treatment of the grid or by addition of detergents. Additionally, contrast can be enhanced by choosing a buffer composition that reduces background, such as detergent-free systems for membrane proteins.

For cryo-EM, particles must be embedded in the vitrified buffer over the holes, but this can be challenging with proteins that preferentially adsorb to the foil. Furthermore, in order to obtain a 3D structure with isotropic resolution a fine coverage of views in all possible directions is required, which is only achievable if the particles adopt random orientations in the ice layer. Preferred orientation can result from either interactions of the protein with surfaces (supporting surfaces or the air-water interface) or by restrictions imposed by ice thickness, when the layer is too thin to accommodate views along the longer axis of the protein. A suitable particle distribution and orientation can be achieved by tweaking buffer composition and plasma conditions, by addition of detergents, by modification of the protein surface charges through crosslinking or by use of alternative surfaces by back-coating of the foil with a thin layer of carbon, graphene or graphene oxide. However, it is important to notice that many of these approaches will have an impact on the image contrast.

During the formation of the thin layer of vitrified buffer, the protein particles are exposed to conditions and surfaces that may deteriorate the sample quality. Among these, contact with the air-water interface is the most problematic, as it can result not only in preferential orientation, but also (partial) denaturation of the protein (D'Imprima et al., 2018; Noble et al., 2018). These interactions may be altered by modifying the buffer and minimized by the use of faster plungers that reduce the period over which particles diffuse within the thin aqueous layer and, therefore, the probability of their adsorption to the air-water interface.

1.4.2. Data collection

The experimental conditions for data acquisition largely depend on the stage of the project and, ultimately, on the resolution required to answer the biological question. Typically, negative-stain electron microscopy is performed in "low-end" microscopes, operating at 120 kV, with electron sources of lower coherence (tungsten filaments and LaB_6 crystals). On the other hand, cryo-EM grids are normally imaged in mid-range and high-end microscopes, with highly coherent electron sources (FEG) and operating at higher voltages, which reduce multiple scattering, specimen charging and Ewald sphere curvature, and increase the beam penetration. For high-resolution cryo-EM, microscopes with acceleration voltages of 300 kV have been preferred, but recent reports show that atomic structures can also be obtained with 200 kV microscopes (Herzik et al., 2017), which produce a slightly higher image contrast. Any microscope must be properly aligned prior to data collection, and it is of utmost importance for high-resolution imaging to assure a parallel beam, coma-free alignment and astigmatism-free image.

In addition to microscope alignment, appropriate imaging conditions must be defined for each project. Since the maximum attainable resolution is limited to twice the pixel size, as stipulated by the Nyquist theorem, using a suitable magnification is essential. The pixel size should thus be selected in a way that the Nyquist frequency is smaller than the target resolution, while the field of view is maximized for an efficient data collection. Likewise, image contrast must be optimized by choosing an adequate objective aperture, defocus range and total electron dose. The former contributes to the amplitude contrast by removing electrons scattered at high angles, but should not be smaller than 70 μm or 100 μm, as it introduces a resolution cutoff. Defocus, as mentioned before, should be kept as low as possible, in a tradeoff between contrast and restorable high frequency signal. The total dose used per micrograph was limited to values between 10 and 20 $e^-/Å^2$ prior to the development of direct electron detectors due to radiation damage; today, thanks to the acquisition of movie stacks and new image processing strategies (see 1.4.3.1. Movie pre-processing), the total

electron dose is chosen in service of efficiency, balancing SNR with exposure time and micrograph file size.

Several decisions must be taken also concerning the camera used for image recording. CCD cameras are conventionally used in negative-stain EM but are limited to low-resolution structural studies. For high-resolution single-particle cryo-EM DDDs are the detectors of choice. Some of these cameras can be used together with energy filters that improve SNR (see 1.2. Image formation in electron microscopy) and while most of them operate in either integrating or counting mode, others can be used in both ways. In these cases, the decision is between faster image acquisition (integrating mode) and a better DQE (counting mode). Each camera has an optimal dose rate. This parameter becomes critical when working in counting mode, as operating with too high a dose rate will result in coincidence loss and consequently a worse DQE. Before image recording, a gain (and hardware dark) reference must be acquired at a dose rate that matches the one used in the subsequent data collection. During long data collection, microscope alignments and camera reference images may have to be reset. Finally, the number of movie frames and the length of each frame must be decided in terms of the total dose and amount of stage drift and beam-induced movement; ideally, each frame should contain enough signal for proper alignment during image pre-processing routines and minimal in-frame movement.

A data collection scheme can also be designed to overcome problems with the specimen, as in the case of preferred orientations. One strategy to mitigate the anisotropy in a 3D structure consists in imaging the specimen after tilting it by an appropriate degree (Tan et al., 2017). In the case of very small proteins, a phase plate can be used, which enhances contrast by introducing phase shift between the scattered and unscattered electrons and, in this way, allows imaging close to focus (Danev and Baumeister, 2016). Automated single particle data collection became widely used in the acquisition of high quality images during the last few years and has speeded up this step greatly (Cheng et al., 2016) (Figure 9). The benefits of automation are also extending to microscope
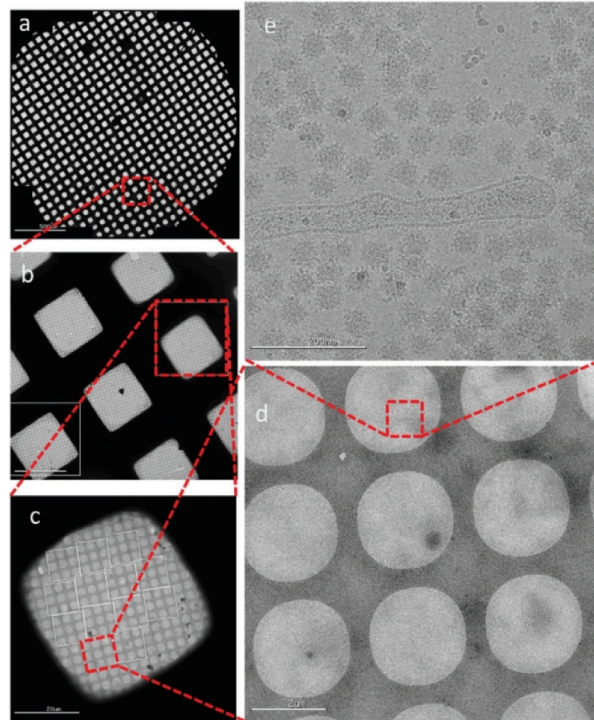
Figure 9. Images of a cryo-EM grid at different magnifications indicative of how imaging areas are targeted hierarchically during automatic data collection. **(a)** Atlas of the hole grid. **(b)** Magnified region of the atlas for square selection. **(c)** Individual grid square. **(d)** Holes. **(e)** Micrograph. Reproduced with permission from Wang et al. (2014). Copyright © 2014 CompareNetworks, Inc.

alignment and will probably increase further as new software packages are developed.

1.4.3. Image processing

Recovering the three-dimensional structure of a biological sample from the two-dimensional TEM images requires intricate methods and processing schemes. The primary steps in this workflow include pre-processing of movie stacks, CTF determination and correction, particle picking, generation of initial models, image alignment and classification, structure reconstruction and refinement, resolution assessment, B-factor sharpening and, finally, map validation and interpretation (Figure 10).
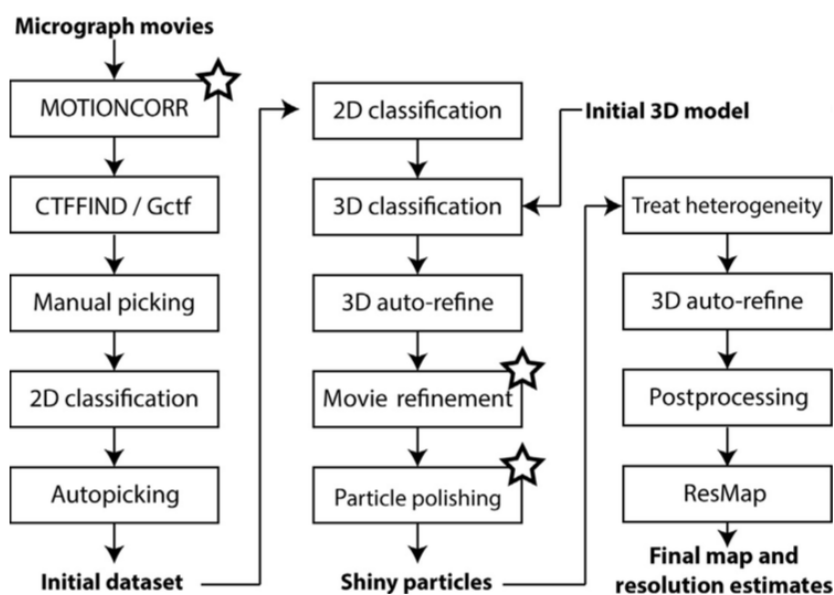
Figure 10. Schematic representation of a typical image processing workflow for single-particle analysis. Some of the steps are referred by the name of common programs used in the field. Reproduced with permission from Scheres (2016). Copyright © 2016 Elsevier Inc.

1.4.3.1. Movie pre-processing

The acquisition of movie stacks with the recently introduced direct electron detectors and new image processing procedures have both contributed to the resolution revolution in single-particle cryo-EM. First of all, pre-processing of movies aims to correct for the specimen movement resultant from mechanical drift and beam-induced motion. This is accomplished by aligning each individual frame, with a minimal amount of movement, to "neighboring" frames or an average of all frames using cross-correlation functions. Programs may conduct alignment of the whole-frame, but also of smaller "tiles", such as in the case of the programs Unblur (Grant and Grigorieff, 2015a) or MotionCor2 (Zheng et al., 2016). The movement of particles in one micrograph is nonetheless anisotropic; motion correction of individual particles is challenging due to the limited signal, but can be performed at later stages of the workflow by marginalizing over running averages of multiple particle movie frames (particle polishing routine in Relion; Figure 11a). This procedure also considers local patterns by analyzing

neighboring particles and may enforce straight tracks or a prior for spatial coherence and temporal smoothness (Scheres, 2014; Zivanov et al., 2018).

On the other hand, dose fractionation within the movie stack generates frames with different levels of radiation damage: early frames contain high-resolution information, but as chemical bonds are progressively broken the later frames accumulate high-frequency noise, while retaining relevant low-frequency signal that aids SNR and, consequently, image alignment. In order to recover all the useful information enclosed in each frame and minimize the noise resultant from radiation damage, dose-weighting schemes are used that filter each frame in a frequency- and dose-dependent manner (Grant and Grigorieff, 2015a; Scheres, 2014). "Dose-filtering" might be performed with B-factors previously established for a given electron dose, as in MotionCor2 and Unblur, or determined from the data itself by reconstructing single-frame maps, as during particle polishing (Figure 11b).
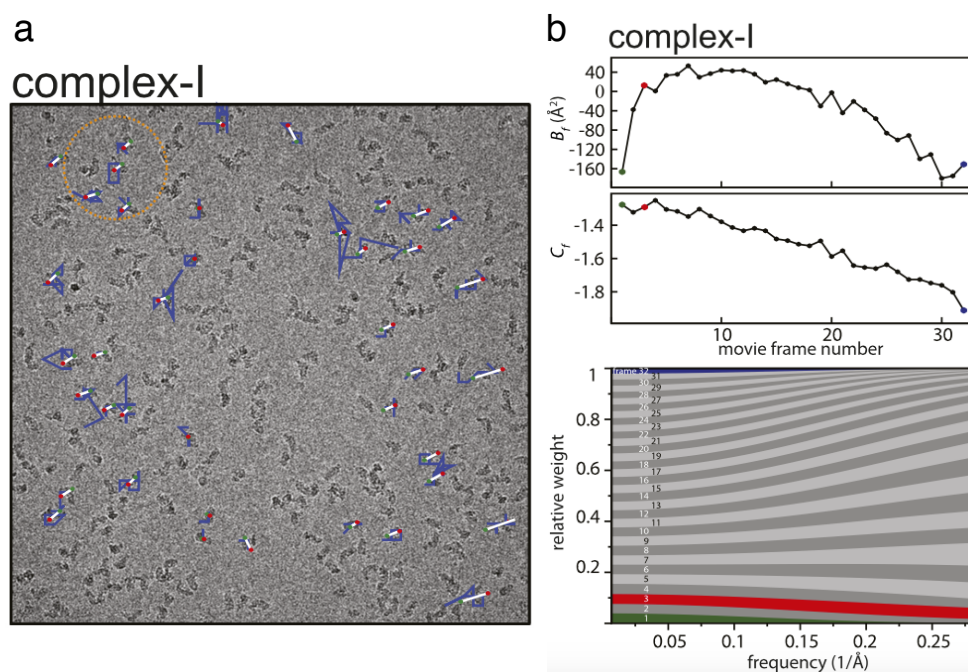
Figure 11. Particle polishing within Relion. **(a)** Beam-induced movement tracks for individual particles (blue) and linear fit used for correction (white). **(b)** B-factors used for "dose-filtering" of the movie stacks. Adapted with permission from Scheres (2014).

Lastly, for some microscopes and magnifications, anisotropic magnification distortions might be significant, producing a pixel size that varies with direction (Grant and Grigorieff, 2015b). This effect becomes critical with large particles and can limit the resolution of the 3D reconstruction. Micrographs can be corrected during movie pre-processing into images that have an isotropic pixel size by use of parameters previously calibrated with gold-shadowed diffraction grating, using programs like MotionCor2 (Grant and Grigorieff, 2015b). If no pre-calibrations were performed, magnification anisotropy can be estimated from the data and corrected at the particle level (Yu et al., 2016).

1.4.3.2. CTF estimation and correction

In case of negative-stain data, CTF correction is often not necessary, as the defoci used are usually small, and the first zero of the CTF occurs at frequencies higher than the resolutions achievable by this method. However, in cryo-EM accurate determination of the CTF is essential for a preliminary evaluation of image quality and, ultimately, to the reconstruction of a high-resolution map. Calculation of the CTF requires user-provided values for microscope-specific parameters (acceleration voltage and spherical aberration) as well as for the percentage of amplitude contrast and, in addition, the estimation of the defocus and astigmatism (largest difference of defocus along two perpendicular directions) for each image. The latter are obtained by fitting theoretical CTFs, calculated for different values of defocus and astigmatism, to the Thon rings in the power spectrum (Mindell and Grigorieff, 2003) (Figure 12). The accuracy of the estimated defocus and astigmatism depends on the size of the window used to compute the power spectra and, therefore, initial CTF determination is usually done for the entire micrograph. However, defocus can vary across an image due to the position of the particle in the layer of vitreous water and due to bent or tilted specimens. For this reason, several packages can refine defocus values at the particle level (Zhang, 2016; Zivanov et al., 2018).
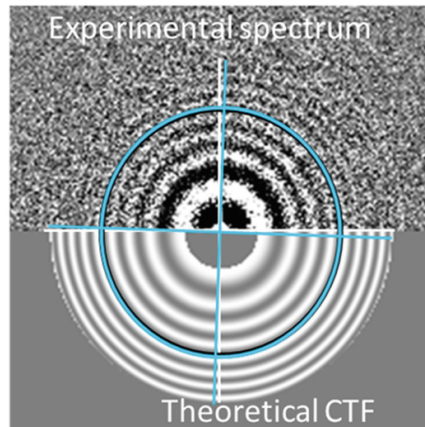
Figure 12. Comparison between the experimental power spectrum (upper half) and the calculated CTF (bottom half). A small amount of astigmatism is observed along the axis shown in blue. Adapted with permission from Costa et al. (2017). Copyright © Springer Science+Business Media LLC 2017.

CTF correction can be performed on the whole micrograph or on the windowed particles, in which case a large box must be used to assure that the high-frequency signal (delocalized in the distorted image) is included. Furthermore, the correction can be applied only to phases (phase flipping) or to both phases and amplitudes (full CTF correction). The first is a simple method, by which phases are flipped in the regions where the sine function has negative values. In the second case, the amplitude decay at increasing frequencies is also corrected, while applying a Wiener filter to avoid noise amplification (Cheng et al., 2015; Orlova and Saibil, 2011). CTF estimation can be performed from stacks or integrated movies, but it should not be done with "dose-filtered" micrographs. As mentioned before, since the information at the nodes of the CTF cannot be recovered for a given image, 3D reconstructions must be derived from images collected at different defoci, where the information of one image fills the zeros of another. Widely used software packages for CTF estimation include CTFFIND4 (Rohou and Grigorieff, 2015) and GCTF (Zhang, 2016).

To visualize high-resolution structural detail, it is also necessary to correct the final 3D map for the reciprocal space envelope decay that suppresses high-frequency signal (see 1.4.3.7. Resolution assessment and B-factor sharpening).

1.4.3.3. Particle picking

As the name suggests, single-particle analysis uses individual projections of the object and, therefore, requires particles to be selected from the original micrographs. Particle selection can be performed manually or (semi-) automatically. Manual particle picking is a tedious and time-consuming task, but valuable in early stages of a project, while the user becomes familiar with the shape and distribution of the protein (Henderson, 2013).

Automatic procedures accelerate picking drastically, but can generate large amounts of false positive or false negative picks and must be customized for each specimen. Programs developed in recent years have become more reliable. Automatic pickers can be feature-based, template-based or use machine-learning procedures. In the first case, features of the particle are expressed in a numerical manner and compared to local areas of the micrograph (e.g. DoG picker selects particles with a given diameter; (Voss et al., 2009)). On the other hand, template-based pickers measure the cross-correlation of a region of the micrograph with images provided that express what the protein should look like, selecting particles that fall above a specified threshold. Templates can be generated by 2D classification of a small dataset of particles or by reprojection of a 3D volume when available. The templates should be low-pass filtered to assure an unbiased picking and subsequent maps should be trusted only if refined to resolutions that surpass the initial threshold, as any reference can be recovered by averaging a sufficient number of noise images ("Einstein from noise" problem). Template-based picking programs include Gautomatch (by Kai Zhang, MRC-LMB Cambridge, UK) and Relion autopick (Scheres, 2015).

Finally, machine-learning algorithms select particles according to the user's preferences, based on training datasets provided. An example of such a program is the recently developed crYOLO picker within the Sphire package (Wagner et al., 2018). After selection, particles must be windowed with a carefully selected box size (see 1.4.3.2. CTF estimation and correction) and normalized to have zero-mean and unity-variance.

1.4.3.4. Initial model generation

Since the orientation assignment in single-particle is done most frequently by projection matching procedures (see 1.4.3.6. Structure reconstruction and refinement), a 3D model is required to generate reprojections to which the experimental images are equated. Such models can be an EM-map from single-particle analysis, subtomogram averaging or electron crystallography, a SAXS model or even a map calculated from an atomic model, of the protein of interest or a closely related homolog. However, if no 3D model is available, a low-resolution, but accurate model must be produced by other methods, as use of an incorrect starting model can impair or bias subsequent refinements.

A commonly used procedure for *ab initio* determination of a 3D model is the random conical tilt method (Radermacher et al., 1987). This approach requires the acquisition of tilt pairs, so that each particle is imaged from two different directions (first at a high tilt, of 45° to 60°, and then with the untilted specimen). After classification of the untilted images, the orientation of the tilted particles is determined by the in-plane rotation of the corresponding untilted view and a first 3D map can be calculated by back-projection (see 1.4.3.6. Structure reconstruction and refinement). The method is reliable and simple and assures a model with the correct handedness. The maps generated in this way are distorted along the z axis due to the missing cone, but if the particles adopt random orientations, an isotropic map can be obtained by averaging multiple maps. A map without a missing cone can also be produced by the related orthogonal tilt method, in which images are collected at tilts of –45° and +45° (Leschziner and Nogales, 2006). In this case, one tilted set of images is used for alignment and classification while the other is used for reconstruction. Accurate initial maps can also be obtained by tomography (and subtomogram averaging) (Frank, 2006). Nevertheless, the need for additional experiments and technical difficulties associated with imaging at high tilts might explain why the single-particle community has invested in the development of alternative, exclusively computational methods.

A preliminary 3D representation of the protein can be calculated using either experimental images or 2D class averages, through methods based on the common lines theorem (two 2D projections of an object have at least one line in common), in reciprocal space or in real space (angular reconstitution), or based on stochastic procedures (stochastic hill climbing projection matching and stochastic gradient descent). Common lines methods take advantage of the central slice theorem (see 1.4.3.5. Image alignment and classification), determining relative orientations by comparing three or more images (Van Heel, 1987). These methods are normally used with 2D class averages, due to the low SNR of individual images, but are still prone to errors. On the other hand, the stochastic hill climbing projection-matching programs use a 3D reconstruction derived from randomized orientations as a starting point, which is then refined iteratively in partially incorrect drifts that help to overcome local minima (Elmlund and Elmlund, 2012). Another projection-matching strategy for generation of initial models is well represented by the EMAN2 implementation, where several models are produced in parallel by a coarse refinement procedure of a small number of high quality 2D class averages, starting from different random blobs; the reliability of each model is evaluated by comparing its reprojections to the 2D class averages used as input, with wrong models being usually easily identified (Tang et al., 2007). Finally, the recently developed stochastic gradient descent method uses small subsets of particles, randomly selected at each iteration, to approximate the true reconstruction through noisy steps determined by the gradient of the approximated objective function (Punjani et al., 2017). This method uses the original particle images and can be successful even with heterogeneous samples that are particularly problematic in the calculation of a first map.

1.4.3.5. Image alignment and classification

The 3D structure of an object can be reconstructed by combining 2D projections along different directions. In this process, the relative position of the many projection images must be determined. Image alignment aims to bring the image

into register with a reference (2D or 3D) by applying appropriate shifts and rotations and is achieved by evaluating the normalized cross-correlation function, normally in Fourier space for faster calculations. This is an iterative process that starts with coarse searches followed by progressively finer inspections as the quality of the reference improves. Particle images must also be classified into homogenous groups. Statistical methods, such as multivariate statistical analysis and principal component analysis, are used to reduce the dimensionality of the problem to a smaller set of uncorrelated variables, also named principal components. Classification can then be achieved by hierarchical clustering or, most commonly, by the k-means clustering method. In the former, depending on the distance of a data point to the existing clusters a new class might be seeded or not, while in the latter the number of classes is predefined by the user. The procedure should minimize the distances or variance within a class and maximize them among classes. After adequate references are generated, the classification is refined through a multi-reference alignment (MRA), where every particle image is cross-correlated to every reference. MRA procedures are prone to lead to what is known as "group collapse", as high SNR classes tend to attract noisy or unrelated particles, leading to the underrepresentation of less populated groups (Cheng et al., 2015). Different programs implement specific strategies to minimize this effect. Particularly successful in this is the program ISAC within Sphire, which sets a limit for the maximum number of particles per class and uses statistical and reproducibility measurements to validate the class assignment (Yang et al., 2012).

Due to the low SNR, images, even containing pure noise, can be correlated to incorrect references. For this reason, and to avoid the "Einstein from noise" problem, any 2D analysis should start with a reference-free alignment, where the images are aligned to the rotationally averaged sum of all images or to a random set of images in the dataset. Additionally, to reduce the contribution of noise to the alignment and classification, real space and reciprocal space masks can be used that exclude background areas around the particle and low- and high-frequency components, respectively, according to the dimension of the particle and the current resolution of the 2D classes (or 3D reconstruction).

Classification in 3D can also be performed to remove lower quality particles, as is done in 2D, or more significantly to discern different 3D objects resultant from conformational or compositional heterogeneity. It consists simply of a multi-reference 3D refinement; maximum likelihood algorithms are ideal to classify unspecified variability and marginalize particles over both orientations and class assignments (see 1.4.3.6. Structure reconstruction and refinement).

1.4.3.6. Structure reconstruction and refinement

As stated in the previous section, a three-dimensional object can be recovered by combining 2D projections over a large angular range (De Rosier and Klug, 1968). In electron crystallography, electron tomography and micro-ED this is achieved by tilting the sample and acquiring multiple images of the object along different directions. On the other hand, in single-particle analysis and helical reconstruction individual macromolecules are randomly oriented and each particle provides a different view of the same object. In this case, the relative orientations of the particle images are not known and must be determined during structure refinement. The most popular method for *a posteriori* angular and translational assignment in 3D is the projection matching method (Penczek, 2010a). This approach requires an initial volume provided by the user, which will be reprojected along many directions. The orientation of the particles is then evaluated by calculating the differences (or similarities) between the experimental image and each reprojection, for all possible rotations and translations. The projection matching method can be applied also in Fourier space by virtue of the central slice theorem, which states that each 2D projection corresponds to a central 2D slice through the Fourier transform of the 3D object, perpendicular to the direction of the projection (Figure 13a). Programs may therefore operate in real space or Fourier space. A new map can be calculated from the experimental images by backprojection and in addition, if operating in Fourier space, by computation of an inverse fast Fourier transform (FFT) (Figure 13b). By application of an iterative refinement, with increasingly finer
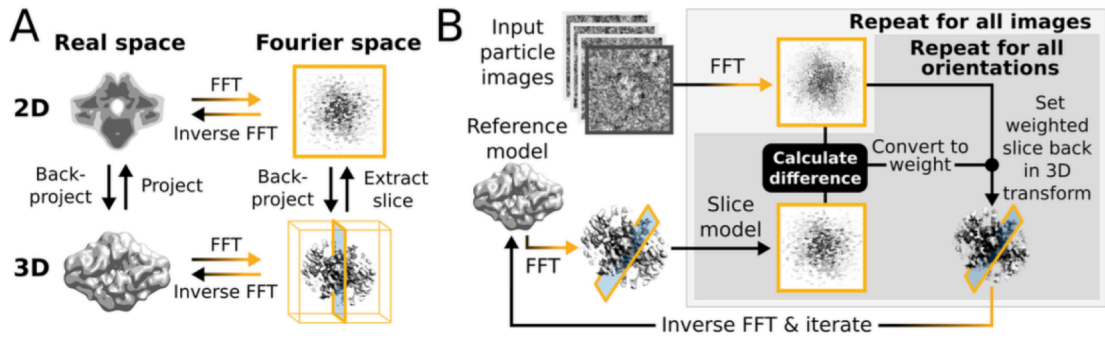
Figure 13. (a) Representation of the relations between 2D projections and 3D volumes in real and Fourier space. **(b)** Schematic representation of the procedure used for image alignment and map reconstruction in Relion. Reproduced with permission from Kimanius et al. (2016).

sampling, the reference volume is gradually improved and consequently a more accurate orientation assignment for each particle is achieved.

Structure refinement might be assisted by the use of 3D masks not only for minimization of the contribution of noise to the alignment (see 1.4.3.5. Image alignment and classification), but also to focus the refinement on specific regions when dealing with flexible structures. More sophisticated strategies may combine masking with signal subtraction at the experimental images (Bai et al., 2015) and multibody refinement (Nakane et al., 2018). The masked regions must nonetheless contain enough signal to drive the alignment; if these are too small, 3D classification without alignment, where particles are marginalized over classes only, can still be performed.

Software packages for image alignment, classification and structure refinement may use cross-correlation or maximum likelihood algorithms. In the first case, each image is assigned to one orientation, for which the cross-correlation is maximal. In the second approach, a probability distribution for the particle orientation is defined based on the cross-correlation values for all possible alignments and classes, and the 2D class averages or 3D maps are calculated by a weighted average. The latter gives more robust alignment parameters and has greatly improved cryo-EM reconstructions. Maximum-likelihood based programs include for example Relion (Scheres, 2012), cisTEM (Grant et al., 2018) and

cryoSPARC (Punjani et al., 2017). In the case of Relion, the most widely used program in the field, a regularization term is introduced in the likelihood function, i.e., image processing is further improved by implementation of an empirical Bayesian algorithm that imposes priors calculated from the data to model signal and noise, which result in the derivation of an appropriate 3D Wiener filter at every iteration (Scheres, 2012).

Refinements can be performed with applied symmetry in the case of symmetric particles. Nevertheless, one should be aware that no protein is truly symmetric and this only depends on the resolution taken into consideration. Therefore, the decision of using a symmetrized map must be carefully considered for each protein and resolution range. An alternative approach entails the classification and subsequent refinement of an artificially expanded dataset according to the symmetry point group (symmetry expansion) (Zhou et al., 2015).

1.4.3.7. Resolution assessment and B-factor sharpening

In order to prevent over-fitting through an iterative build-up of noise, current refinement procedures operate according to a "gold-standard" approach, in which the dataset is split in two halves that are refined independently and merged just at the end of the refinement. The resolution of the reconstruction, to which the map is filtered, is then determined by evaluating to which frequencies the two independent half maps correlate well, in a measurement that reflects the power of the SNR as a function of spatial frequency (Fourier shell correlation, FSC) (Penczek, 2010b). To avoid under-estimation of the map resolution, strategies to remove contributions of background noise to the FSC must be used, such as multiplication of the map by a real space soft mask (e.g. Relion (Scheres, 2012)) or mathematical corrections for solvent content given for example the molecular weight of the protein (e.g. cisTEM (Grant et al., 2018)). The frequency at which the FSC crosses the 0.143 threshold is considered the nominal resolution of the map and is based on the correlation between a map calculated from the full dataset and a perfect reference (Rosenthal and Henderson, 2003).

Most maps will locally deviate from the nominal resolution, due to inherent flexibility or simply due to the (in)accuracy of rotational alignment (small errors in the rotation angles will have a bigger detrimental effect at the periphery of the map). For this reason, several software packages have been developed to evaluate the local resolution of a map, including ResMap (Kucukelbir et al., 2014), LocalRes within Sphire (Moriya et al., 2017), and the local resolution implementations in Relion (Kimanius et al., 2016) and cryoSPARC (Punjani et al., 2017). Additionally, if Fourier space is not filled adequately, due to preferential orientation of the particles on the grid, the map will have an anisotropic directional resolution, which can be quantified by 3D FSC volumes (Tan et al., 2017).

As explained previously, during image formation, image detection and image processing high frequencies are dampened. This fall-off can be modeled by a Gaussian function with a B-factor similar to the temperature factor used in x-ray crystallography. Therefore, to produce a map with visible high-resolution features the reconstruction must be sharpened by application of a negative B-factor (B-factor sharpening), which can be estimated from the reconstruction (Rosenthal and Henderson, 2003) or specified by the user.

1.4.3.8. Map validation and interpretation

Even though the nominal resolution determined through the FSC informs on the interpretability of the map, this does not assure that the reconstructed volume is correct as it only reflects the consistency between the two half maps. This problem was particularly significant before the resolution revolution in single-particle cryo-EM, when it was common to obtain maps that did not resolve secondary structure features. Nonetheless, a critical analysis is still essential. The user should first of all verify if the raw images agree with both class averages and reprojections of the map and if the features of the map agree with the estimated nominal resolution (e.g. helix separation at 7 to 9 Å resolution, strand separation below 4.7 Å resolution and visible bulky side chains for resolutions below

~4.5 Å). The reliability of a map might also be judge based on previously determined structures for the whole protein or its components, if available.

One simple error that can pass undetected is the inversion of the handedness of the map. The correct hand can be easily identified for higher resolutions, when the helical pitch is clearly visible, but for lower resolution validation requires acquisition of tilt data (see 1.4.3.4. Initial model generation and tilt pairs method described below). Another possible pitfall is the refinement of a structure from particles in different states, in the absence of an adequate 3D classification. This can often be recognized by evaluation of local resolution.

Map validation can be performed through the acquisition of tilt pairs, with low tilt (10° to 30°), and subsequent verification of the particle orientations by projection matching using the final map (Henderson et al., 2011; Rosenthal and Henderson, 2003). This strategy has the advantage of also allowing the determination of the correct handedness.

Regarding the interpretation of the map, this depends of its resolution: at resolutions lower than 10 Å the map reveals only the shape of the protein and rigid body fitting of available structures might be performed, although it may be unreliable; at intermediate resolutions, from 10 to 4 Å, secondary structure elements are resolved and rigid and flexible body fitting can be used; at resolution better than 4 Å, when side chains become visible, models can be built *de novo*.

1.5. Bioenergetics, cellular respiration and electrochemical gradient

Production and depletion of energy are the principles at the basis of the metabolism of any living organism that allows them to grow and reproduce. Sources of energy range from the sunlight used by phototrophs, to organic and inorganic substrates that are oxidized in organotrophs and lithotrophs, respectively. The potential energy stored in organic compounds can be retrieved by fermentation and anaerobic or aerobic cellular respiration, the latter of which

is the most efficient process. During cellular respiration, molecules are oxidized and electrons are carried through an electron transfer chain to the final electron acceptor. While the most widely used final electron acceptor is molecular oxygen, in anaerobiosis this is replaced by either organic or inorganic compounds.

The energy released during this process is stored in the form of a transmembrane difference of electrochemical potential, by translocation of protons (or occasionally sodium ions) to the intermembrane space in mitochondria and periplasm in bacteria. Diffusion of protons across the membrane, in the direction of the electrochemical gradient generated by the respiratory protein complexes, through proton channels in the ATP synthase complex drives the mechanical rotation of its rotor ring and induces the conformational changes required for synthesis of ATP at the catalytic head (Sousa et al., 2018a). Likewise, the bacterial flagellar motor converts proton flow into torque and, therefore, proton motive force can be used for motility (Nirody et al., 2017). The transmembrane flux of protons can also be coupled to the co-transport of solutes by secondary active transporters (Shi, 2013).

During my doctoral work, I structurally characterized by single-particle cryo-EM two membrane protein complexes from aerobic respiratory chains and a bacterial transporter. Accordingly, this thesis is organized in three chapters dedicated to the following topics:

- respirasome, a supercomplex of complexes I, III and IV present in the mitochondrial respiratory chain (chapter I);
- alternative complex III, a quinol:cytochrome *c*/HiPIP oxidoreductase in many bacterial respiratory chains (chapter II);
- KimA, a high-affinity potassium transporter that takes advantage of the proton gradient maintained by cellular respiration (chapter III).

CHAPTER I

2. Introduction

2.1. Mitochondrial respiratory chain

Mitochondria are the main site for ATP production in eukaryotic cells, through a process known as oxidative phosphorylation (OXPHOS). These organelles are delimited by an outer membrane (OMM) and an inner membrane (IMM), which
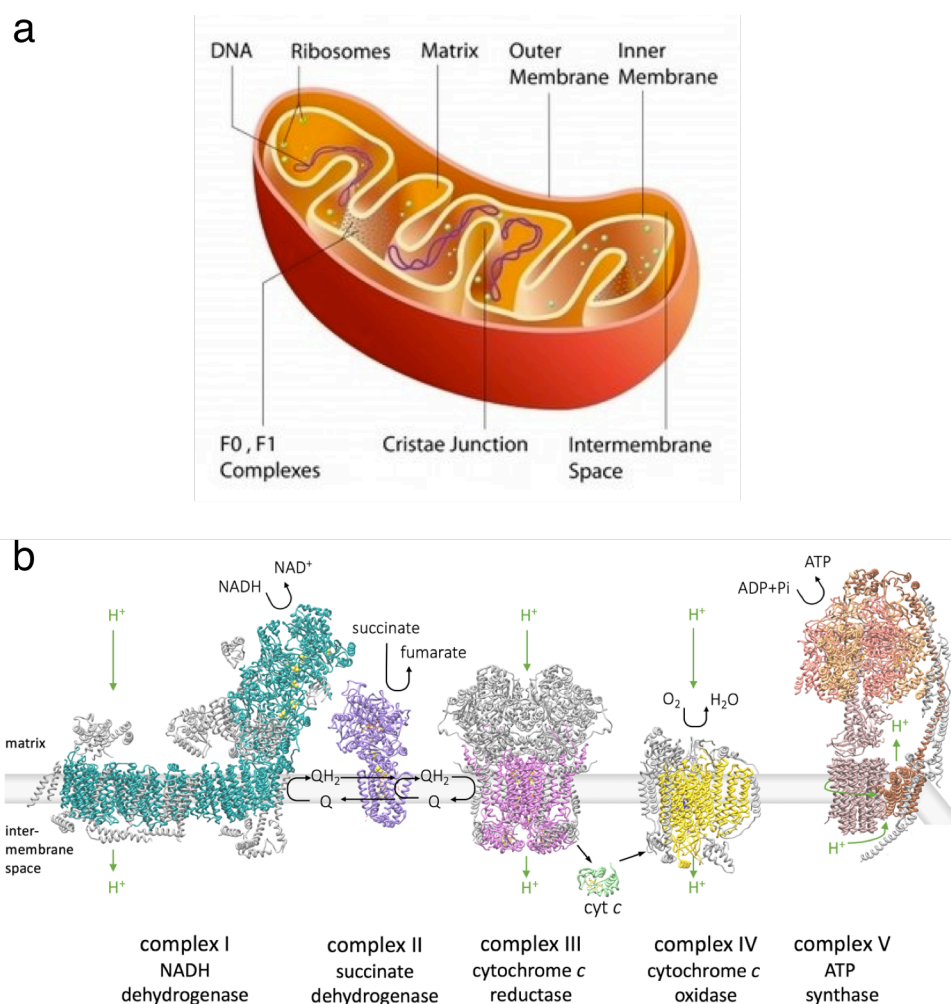
Figure 14. (a) Schematic representation of mitochondria architecture. Reproduced from http://images.tutorvista.com/cms/images/123/structure-of-mitochondria1.JPG. **(b)** Respiratory chain in the IMM. Core subunits of complexes I, II, III, IV and ATP synthase are shown in cyan, purple, pink, yellow and salmon/orange, while accessory subunits are shown in grey. Reproduced with permission from Sousa et al. (2018). Copyright © Springer Nature Singapore Pte Ltd. 2018.

define dedicated compartments (Figure 14a). In the mitochondrial matrix, oxidation of acetyl-CoA by the citric acid cycle generates NADH and succinate, the primary substrates of the mitochondrial respiratory chain. The large membrane protein complexes that compose the mitochondrial respiratory chain are located in the IMM; four complexes transfer electrons from NADH and succinate to molecular oxygen, of which three use the chemical energy released in the redox reactions to pump protons into the intermembrane space (IMS) (Figure 14b). The electrochemical gradient generated is used by the mitochondrial ATP synthase located at the tip of the mitochondrial cristae to produce ATP.

2.2. Complex I

The first protein complex in the electron transfer chain is NADH:ubiquinone oxidoreductase (complex I; Figure 15). The distinctive L-shape of the complex reflects the arrangement of the hydrophilic matrix arm and the membrane arm. In its dehydrogenase domain (N module), the former contains a flavin-mononucleotide (FMN) and a ~90 Å chain of seven iron-sulfur (FeS) clusters, which mediate the transfer of two electrons from the NADH at the distal end of the arm to a ubiquinone molecule in the hydrogenase domain (Q module), near the membrane surface (Sazanov and Hinchliffe, 2006). The membrane arm constitutes the proton pumping module, where four antiporter-like motifs, composed of two 5 transmembrane helices (TMH) structural-inverted repeats, are proposed to pump four protons across the IMM per catalytic cycle (Efremov and Sazanov, 2011; Leif et al., 1995). The coupling between the redox reaction and proton translocation remains to this date the main unanswered question in complex I catalysis. Complex I is composed of 14 core subunits that are largely conserved from prokaryotes to eukaryotes (Walker, 1992) and a variable number of supernumerary subunits, which in the mammalian enzyme bring the total number of polypeptide chains to 45 (Carroll et al., 2002; Vinothkumar et al., 2014). Complex I is a major source of reactive oxygen species (ROS) that play a crucial role in oxidative stress (Lenaz, 2012).

Figure 15. Structure of mitochondrial complex I, with 14 core subunits shown in color and 31 supernumerary subunits depicted in white. The structure of the cofactor chain and modeled ubiquinone is also shown in a separate panel. Reproduced with permission from Agip et al. (2018). Copyright © 2018 Nature America Inc.

2.3. Complex II

Succinate dehydrogenase, or complex II, is a member of both the respiratory chain and the citric acid cycle. The complex catalyses the oxidation of succinate to fumarate and the reduction of ubiquinone to ubiquinol. Although it does not translocate protons across the IMM, complex II feeds electrons into the respiratory chain by contributing to the ubiquinol pool used by complex III. Complex II is composed by a flavoprotein with a flavin adenine dinucleotide (FAD), an iron-sulfur protein with three FeS clusters and a membrane anchoring domain, which in mitochondria consists of two transmembrane proteins that coordinate one heme *b* (Hägerhäll, 1997).

2.4. Complex III

The ubiquinol pool maintained by complexes I and II is utilized by the cytochrome bc_1 complex, also known as complex III (Figure 16), to reduce the soluble electron carrier cytochrome *c*. Complex III is a symmetrical dimer, with each protomer consisting of three core subunits (Yang and Trumpower, 1986) and up to eight accessory subunits, as for the mammalian enzyme (Schägger et al., 1986). The three core subunits constitute the minimal active form of the complex and are highly conserved from bacteria to mammals. The largest amongst these is cytochrome *b* (cyt *b*), which harbors two *b*-type hemes (b_L and b_H) and two distinct quinone-binding sites at opposite sides of the membrane; the Q_o site is located on the positive side, near heme b_L and serves ubiquinol oxidation, while the Q_i site neighbors heme b_H at the matrix side and conducts ubiquinone (or semiquinone) reduction (Xia et al., 1997). The two other core subunits are cytochrome c_1 (cyt c_1) and the Rieske iron-sulfur protein (ISP); both subunits are anchored to cyt *b* by a single TMH and enclose in their soluble domain a *c*-type heme (c_1) and a [2Fe-2S] cluster, respectively (Yang and Trumpower, 1986). Each ISP subunit spans both complex III protomers, with its
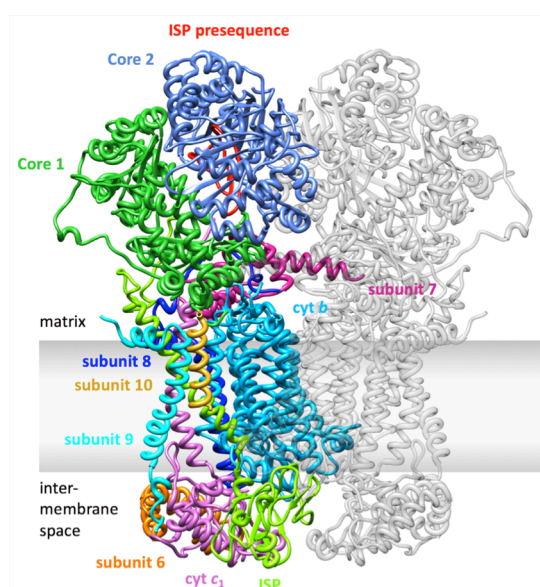
Figure 16. Structure of mitochondrial complex III with color-coded subunits in one monomer and the second monomer in grey. Reproduced with permission from Sousa et al. (2018). Copyright © Springer Nature Singapore Pte Ltd. 2018.

36
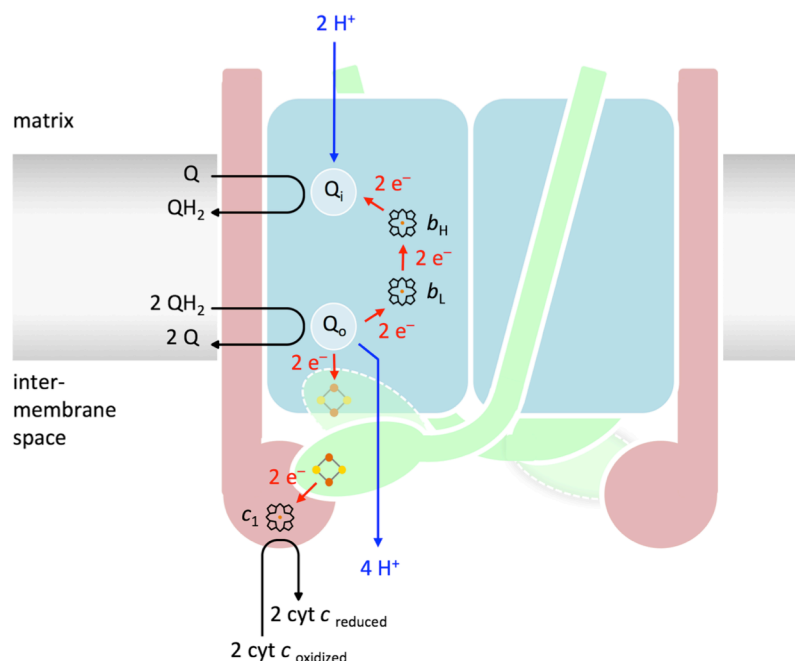
Figure 17. Schematic representation of the Q-cycle of the bc_1 complex. Cyt b, cyt c_1 and ISP are shown in blue, pink and green, respectively. Reproduced with permission from Sousa et al. (2018). Copyright © Springer Nature Singapore Pte Ltd. 2018.

TMH associated with one protomer while the soluble domain with the [2Fe-2S] cluster transfers electrons from ubiquinol to cyt c_1 in the opposite protomer.

The catalytic mechanism of complex III proceeds according to the modified Q-cycle, originally proposed by Peter Mitchell (Mitchell, 1974, 1976) (Figure 17). The reaction initiates with the binding of a ubiquinol molecule to the Q_o site and a ubiquinone at the Q_i site. Ubiquinol is first oxidized to semiquinone, by transferring one electron to the [2Fe-2S] cluster of the ISP. The ISP reduces heme c_1 that, subsequently, donates the electron to cytochrome c. The unstable semiquinone radical produced at the Q_o site sequentially reduces hemes b_L and b_H with its second electron. The ubiquinone bound at the Q_i site accepts the electron from the high-potential heme b_H giving place to a stabilized semiquinone. To complete the Q-cycle, a second ubiquinol is oxidized at the Q_o site, with reduction of a second cytochrome c and of the semiquinone at the Q_i site to ubiquinol. During the Q-cycle, two protons are picked up from the matrix for ubiquinone reduction at the Q_i site and four protons are released to the IMS

upon ubiquinol oxidation at the Q_o site. In this way, the topological separation of the two quinone-binding sites establishes the vectorial transport of protons across the IMM. Productive electron transfer from the Q_o site to the c_1 heme is dependent on significant conformational changes of the soluble domain of the ISP, which alternates between b position (close to the Q_o site) and c position (close to cyt c_1) to optimize the distances to either redox partner (Darrouzet et al., 2000; Iwata et al., 1998). It has been shown that under normal steady-state conditions only one Q_o site is active at a given moment (Castellani et al., 2010). Accordingly, the protomers were proposed to randomly alternate between active and inactive states (half-of-the-sites reactivity model). Rapid electron equilibration between the b_L hemes (Castellani et al., 2010; Lanciano et al., 2011) should allow ubiquinone reduction in either Q_i site.

2.5. Complex IV

The terminal oxidase in the mitochondrial respiratory chain is cytochrome c oxidase (complex IV; Figure 18). In its simplest form, complex IV is composed of subunits I, II and III. Subunit I contains heme a, heme a_3 and Cu_B, while subunit II,
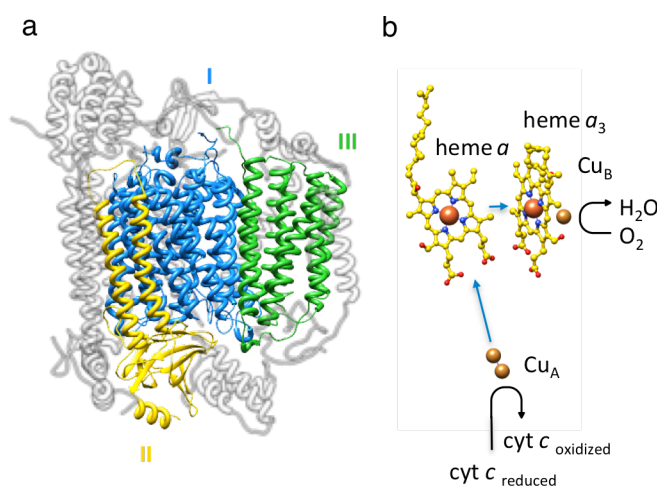
Figure 18. (a) Structure of mitochondrial complex IV with core subunits shown in blue, yellow and green and accessory subunits shown in grey. **(b)** Redox metal centers and electron transfer flow (blue arrows) in complex IV. Adapted with permission from Sousa et al. (2018). Copyright © Springer Nature Singapore Pte Ltd. 2018.

to which cytochrome c binds, encloses Cu_A. Subunit III stabilizes the first two subunits and acts as an initial proton acceptor (Alnajjar et al., 2014; Varanasi and Hosler, 2012). In mammalian mitochondria, complex IV has 11 accessory subunits that strongly depress its activity and are essential for regulation (Arnold and Kadenbach, 1997; Arnold et al., 1998; Sousa et al., 2018a; Yang et al., 1998). Several complex IV subunits have distinct isoforms that are tissue- or developmental stage-specific and that introduce an extra level of regulation (Bonne et al., 1993; Ewart et al., 1991; Hüttemann et al., 2003a, 2003b; Parsons et al., 1996; Schlerf et al., 1988).

Complex IV couples the reduction of molecular oxygen to water to the translocation of four protons into the IMS. During catalysis, Cu_A sequentially receives four electrons from four reduced cytochrome c molecules and transfers them to the Fe_{a3}/Cu_B binuclear center via Fe_a from heme a. The transfer of each electron to the active site is accompanied by the uptake of two protons from the matrix, for a total of eight protons at the end of the catalytic cycle. For reduction of the terminal acceptor, the four electrons at the active site are simultaneously transferred to O_2 and, together with half of the protons picked up from the mitochondrial matrix, used for water formation. The remaining four protons are transferred to the IMS (Wikstrom, 1977). The nonsequential four-electron reduction of molecular oxygen and the overall architecture of complex IV reduce the production of ROS by the complex to negligible values (Muramoto et al., 2010).

The transfer of protons within complex IV has been proposed to occur via a hydrogen bond network or by mobile water molecules in the hydronium state. In the mitochondrial enzyme, three proton pathways have been described (Wikström et al., 2015): the D-channel mediates the translocation of the four protons pumped into the IMS and, together with the K-channel, transports the chemical protons required for water formation (Brzezinski and Adelroth, 1998; Konstantinov et al., 1997), while the H-channel is believed to act as a dielectric channel for minimization of the thermodynamic cost of moving electrons into the nonpolar membrane domain (Rich and Maréchal, 2013).

2.6. Mitochondrial disorders

Defects of respiratory chain complexes are at the origin of serious genetic diseases with highly variable clinical presentation. These disorders often are multi-systemic and manifest in early childhood, but can also be restricted to a specific tissue and develop during adulthood (Keshavan and Rahman, 2018; Suomalainen and Battersby, 2018). About 30% of the mitochondrial disorders can be traced to mutations in complex I subunits, and include, among others, Leber's hereditary optic neuropathy, infantile-onset Leigh syndrome and fatal neonatal lactic acidosis (Fiedorczuk and Sazanov, 2018). Complex I disorders are most frequently associated with defects of its core subunits, but can also arise from mutations in supernumerary subunits (Rodenburg, 2016). Less common but equally severe are complex III related pathologies that most frequently result from mutations of the cyt *b* subunit or the assembly factor BCS1L (Meunier et al., 2013). Interestingly, human patients with progressive exercise intolerance and lactic acidosis due to point mutations (Bruno et al., 2003) or truncation (Lamantea et al., 2002) of cyt *b* were found to have diminished levels of not only complex III but also of complex I. The secondary loss of complex I upon depletion of complex III was reproduced in biochemical studies (Acín-Pérez et al., 2004; Schägger et al., 2004). Complex IV-linked pathologies are more often caused by mutations of specific assembly factors, but also by mutations of mitochondrial-encoded subunits (Rak et al., 2016), and can reduce levels of complex I as well (D'Aurelio et al., 2006; Diaz et al., 2006; Vempati et al., 2009). Inhibition of ROS production by reverse electron transport (RET) was used to reestablish complex I homeostasis in the absence of complexes III or IV (Guarás et al., 2016), while disruption of their activity is insufficient to produce complex I deficiency (Acín-Pérez et al., 2004; Guarás et al., 2016).

2.7. Supramolecular organization of the respiratory chain complexes

The distribution of respiratory chain complexes within the IMM was questioned early in the field's history. In 1955, Chance and Williams proposed in their solid-state model that OXPHOS complexes associate in higher-order structures

that enable efficient electron transfer (Chance and Williams, 1955). This model was quickly discarded, as successful purifications of isolated and active complexes suggested that they exist as single entities in the membrane. According to the fluid or random collision model, the complexes diffuse freely and electron transfer occurs during random collisions of the electron carriers (Hackenbrock et al., 1986). For several decades, the latter model was widely accepted and reports of stable supercomplexes of complexes III and IV in some prokaryotes were dismissed as a species-specific trait (Iwasaki et al., 1995). The presence of supercomplexes in eukaryotes was finally established at the beginning of the 21st century, after solubilization with mild detergents like digitonin and analysis by blue-native polyacrylamide gel electrophoresis (BN-PAGE) (Schägger and Pfeiffer, 2000). Initial structural studies by negative-stain EM showed that supercomplexes are well-ordered assemblies (Dudkina et al., 2005; Heinemeyer et al., 2007; Schäfer et al., 2006) and, more recently, analysis by subtomogram averaging corroborated that these structures exist in the mitochondrial membrane (Davies et al., 2018) (Figure 19). Numerous stoichiometric supercomplexes with various combinations of complexes I, III and IV have since been identified, while evidence that complex II also integrates such structures is limited. Studies with bovine heart mitochondria suggest that all
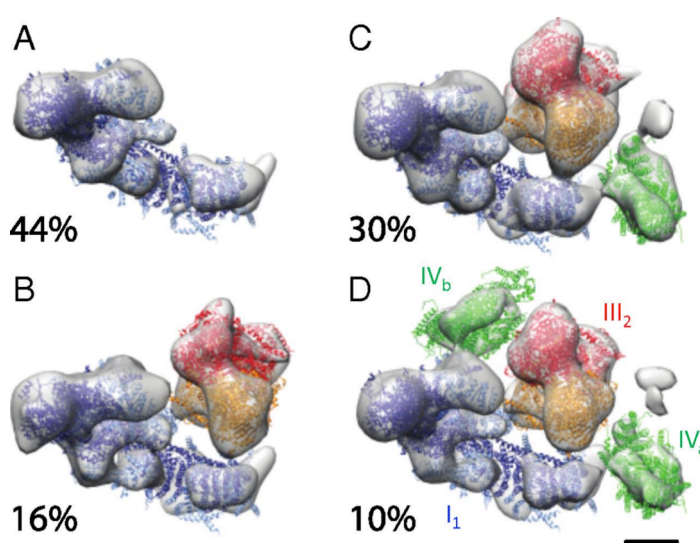
Figure 19. Maps of respiratory chain complex I and supercomplexes present in bovine heart mitochondria. Reproduced with permission from Davies et al. (2018).

complex I is found in supercomplexes, while approximately 30% of complex III and more than 85% of complex IV occur isolated in the membrane (Schägger and Pfeiffer, 2001). The plasticity model reconciles the two earlier models, postulating that respiratory complexes exist in an equilibrium between free enzymes and large supramolecular assemblies (Acín-Pérez et al., 2008). This ratio is highly regulated, varying across cell types and according to physiological stimuli. The plasticity of the system might be essential for metabolic regulation, by adaptation to substrate availability or modulation of ROS signaling.

The most studied supercomplex to date is the respirasome ($I_1III_2IV_1$) that contains the three complexes required for the electron transfer from NADH to molecular oxygen. It has been shown that respiratory supercomplexes are dependent on cardiolipin (Mileykovskaya and Dowhan, 2014) and one supercomplex assembly factor named SCAF1 was unquestionably identified (Cogliati et al., 2016; Lapuente-Brun et al., 2013). However, the assembly process for these structures is still unknown. Two models for respirasome biogenesis have been advanced after conflicting results were obtained in higher eukaryotes. The first model proposes that the respirasome is formed by association of the mature individual complexes (Guerrero-Castillo et al., 2017), while the second suggests that single subunits and intermediate assemblies are progressively integrated into the supercomplex (Moreno-Lastres et al., 2012).

The association of the OXPHOS complexes into supercomplexes is thought to introduce structural and functional advantages. From a structural perspective, supercomplexes were suggested to contribute to complex I assembly or stability. The hypothesis was supported by reports of combined deficiencies of complex III/IV and complex I (Bruno et al., 2003; D'Aurelio et al., 2006; Diaz et al., 2006; Lamantea et al., 2002; Vempati et al., 2009), which cannot be reproduced by inhibition of complex III or IV activity (Acín-Pérez et al., 2004; Guarás et al., 2016) and thereby implicate physical interactions with these respiratory complexes in the proper assembly of complex I. In agreement with this, the Moreno-Lastres assembly model mentioned previously postulates that subunits from the N-module of complex I are integrated only at the late stages of the process and solely after association of an imature subcomplex of the

NADH:ubiquinone oxidoreductase with complexes III and IV (Moreno-Lastres et al., 2012). Supercomplexes have also been connoted with diminished ROS production by both complexes I and III, as larger ratios of free to superassembled complex I (Maranzana et al., 2013) and destabilization of the III_2IV_1 supercomplexes of *Saccharomyces cerevisiae* (Chen et al., 2012; Vukotic et al., 2012) have been shown to increase ROS levels. Finally, substrate channeling within supercomplexes has been debated controversially. Substrate channeling is defined as a direct transfer of an intermediate between the active sites of two enzymes that catalyse consecutive reactions and should enhance catalysis and, in this case, the efficiency of the electron transfer. Channeling of quinone and cytochrome *c* were hypothesized for the respirasome. Several studies by flux-control analysis found that both complexes I and III are rate-limiting for NADH oxidation (Bianchi et al., 2004; Lapuente-Brun et al., 2013; Lenaz et al., 2018) as would be expected upon quinone channeling. Partition of the quinone pool in dedicated populations for succinate- and NADH-dependent respiration due to substrate channeling would explain why a decrease of complex III levels can impair succinate-dependent electron transfer while NADH oxidation is maintained by superassembled complex III (Lapuente-Brun et al., 2013). However, two reports have questioned the existence of distinct quinone pools (Blaza et al., 2014; Fedor and Hirst, 2018). Contradictory results hindered also a conclusion regarding cytochrome *c* channeling.

The respirasome is conserved in all higher eukaryotes and is the most abundant supercomplex in mitochondria from bovine heart (Schäfer et al., 2006; Schägger and Pfeiffer, 2000, 2001). Low resolution structures (20-30 Å) of this supercomplex have been determined by single-particle analysis and cryo-electron tomography (Althoff et al., 2011; Dudkina et al., 2011; Schäfer et al., 2007), however the resolution of the maps was insufficient to fully comprehend the structure of this assembly. I used single-particle cryo-EM to produce a subnanometer structure of the respirasome from *Bos taurus* that expanded our knowledge on the supercomplex's architecture and activity.

3. Methods

3.1. Isolation and purification of the respirasome

Bovine heart mitochondria were prepared by differential centrifugation as described (Krause et al., 2005). Mitochondria were solubilized with 1% (w/v) digitonin (Calbiochem) at a detergent-to-protein ratio of 28:1 (Schäfer et al., 2006) or with 0.11% (w/v) PCC-a-M (Glycon) at a detergent-to-protein ratio of 1:1, for 1h at 4 °C. The detergent was exchanged to amphipol A8-35 by incubation with γ-cyclodextrin (Sigma Aldrich) at 4 °C for 30 min. Precipitated material was removed by centrifugation at 45,500 g for 30 min at 4 °C in a tabletop centrifuge. Linear density gradients were prepared on a BioComp Gradient Master (Coombs and Watts, 1985) from 0.3 to 1.3 M trehalose in 20 mM KCl and 15 mM HEPES pH 7.7. Approximately 2 ml of solubilized mitochondria, corresponding to ~2 mg of mitochondrial protein, were added to the top of each density gradient and separated by ultracentrifugation at 217,000 g for 21 h at 4 °C in a SW40 rotor (Beckman). Gradients were fractionated from top to bottom and analyzed for protein content by BN-PAGE (Wittig et al., 2006). Trehalose was removed by dilution/concentration cycles in a Centricon with 100 kDa MWCO (Millipore).

3.2. BN-PAGE and in-gel activity assays

Proteins were separated on 3-12% polyacrylamide linear gradient gels by BN-PAGE and 2D BN/BN-PAGE (Wittig et al., 2006). Functionally active supercomplexes were detected by in-gel activity assays for NADH:dehydrogenase and cytochrome *c* oxidase (Grad and Lemire, 2006; Kuonen et al., 1986). Briefly, for complex I, gels were incubated in buffer containing 100 mM Tris, pH 7.4, 0.5 mM NBT (*p*-nitrotetraazolium blue) and 100 μM β–NADH for 1h. For complex IV, gels were incubated for 10-12h in 50 mM sodium phosphate buffer at pH 7.2, 0.5 mg/ml DAB (3,3'diamino-benzidine tetrahydrochloride), 1 mg/ml equine heart cytochrome *c* and 20 U/ml bovine liver catalase.

3.3. Negative-staining

Samples of respirasome in amphipol, initially solubilized with either digitonin or PCC-a-M, were applied to 3 mm, 400 mesh, carbon coated copper grids (SPI) previously glow-discharged at 0.38 mbar and 15 mA for 45 seconds, and blotted after 30 seconds with filter paper #4 (Whatman). Immediately afterwards, a drop of a 1% (w/v) solution of uranyl acetate, pH 4 was applied and blotted, followed by incubation with a second drop for 30 seconds. For respirasomes purified from digitonin-solubilized mitochondria, electron micrographs were acquired with a CCD camera (Ultrascan 2000) on a CM120 at 120 kV under low-lose conditions, at a magnification of 45,200x for a pixel size at the specimen of 3.1 Å. Approximately 4000 particle images were manually picked with EMAN boxer (Ludtke et al., 1999). For respirasomes purified from PCC-a-M solubilized mitochondria, images were acquired with a CCD camera (Ultrascan 4000) on a Tecnai Spirit at 120 kV under low-lose conditions, at a magnification of 34,000x for a pixel size at the specimen of 3.2 Å and ~42,000 particles were picked automatically with Relion 1.4 (Scheres, 2012) after generation of adequate templates from a small set of particles picked manually. Both datasets were first analysed by a reference-free 2D classification in Relion 1.4. Particles from the best 2D class averages were further classified in 3D, using as an initial reference an earlier low-resolution respirasome map (EMD-1876; (Althoff et al., 2011)) low-pass filtered to 60 Å.

3.4. Single-particle cryo-EM specimen preparation and data collection

Cryo-EM grids were prepared in a FEI Vitrobot plunge freezer at 10 °C and 90% humidity, using Quantifoil R2/2 holey carbon grids (Quantifoil Micro Tools). The grids were pre-treated in chloroform for 1 to 2 hours for removal of residual plastics and freshly glow-discharged at 0.38 mbar and 15 mA for 90 seconds. After 3 seconds from the application of the sample (2.4 µl of respirasome in amphipol A8-35 at ~170 µg/ml plus 0.6 µl of 1 M KCl added immediately before freezing to reduce aggregation) to the grid, this was blotted for 10 seconds, at blotting force –2, with filter paper #597 (Whatman) and, subsequently, quickly

plunged into liquid ethane. Cryo-EM images were collected manually on a FEI Tecnai Polara operating at 300 kV and aligned as previously described (Mills et al., 2013), with a Falcon III direct electron detector operating in integrating mode at a rate of 32 frames/s. A nominal magnification of 59,000x yielded a pixel size at the specimen of 1.77 Å. Videos were collected for 1.5 seconds with a total of 46 frames with a calibrated dose of about 3 e$^-$/ Å^2 per frame, at defocus values between –1.3 and –4.3 μm.

3.5. Image processing

A set of 3,592 micrographs was collected manually. Whole-image drift correction of each movie was performed using the algorithm developed by Li (Li et al., 2013). Particles were picked manually using EMAN Boxer (Ludtke et al., 1999), and the micrograph-based CTF was determined using CTFFIND3 (Mindell and Grigorieff, 2003) in the Relion 1.4 workflow (Scheres, 2012). An initial dataset containing 156,519 particle images (288 pixels x 288 pixels) was picked manually using EMAN boxer (Ludtke et al., 1999). Particles were subjected to two-dimensional reference-free classification in Relion 1.4 (Scheres, 2012). Visual selection of particle classes with interpretable features resulted in a dataset of 137,606 particle images for the first 3D consensus refinement. The earlier low-resolution respirasome map (Althoff et al., 2011) was low-pass filtered to 60 Å and used as an initial model for the 3D refinement in Relion 1.4. Individual frames were B-factor weighted and movements of individual particles were reversed by movie frame correction in Relion 1.4 (Scheres, 2014). The resulting dataset of polished particles was used for 3D classification and the best 3D classes were selected for further processing. Refinement of three different subsets of particles produced maps at 9.1 Å, 10.4 Å and 9.9 Å resolution. Local resolution was estimated using ResMap (Kucukelbir et al., 2014). UCSF Chimera (Pettersen et al., 2004) was used for visualization of cryo-EM maps, docking of atomic models and preparation of figures.

4. Results

4.1. Purification of the respirasome from bovine heart mitochondria

The purification procedure implemented in an earlier structural study of the respirasome (Althoff et al., 2011) used digitonin for mitochondria solubilization followed by a density gradient of amphipol-trapped supercomplexes. Replication of this procedure showed that the density gradient did not resolve supercomplexes $I_1III_2IV_1$ and I_1III_2 (Figure 20a), as was also the case in the original paper (Althoff et al., 2011). Analysis by negative-staining revealed that 3D classification procedures segregated two populations of particles consistent with the presence of both supercomplexes (Figure 20b). Even though an *in silico* "purification" strategy seemed possible, the presence of supercomplex I_1III_2 in the sample reduced the number of usable particles in the dataset, which was of
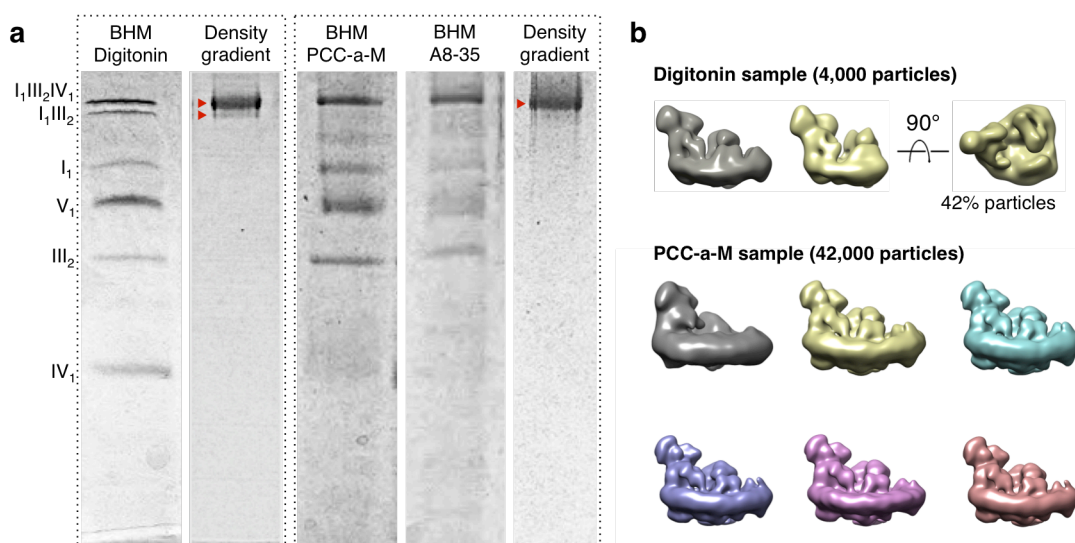
Figure 20. (a) Left panel: BN-PAGE of bovine heart mitochondria (BHM) solubilized with digitonin (lane 1) and of a subsequent density gradient fraction of respirasome in A8-35, contaminated with supercomplex I_1III_2 (lane 2). Right panel: BN-PAGE of BHM solubilized with PCC-a-M (lane 3) and after exchange to A8-35 (lane 4), and of density gradient fraction of supercomplex $I_1III_2IV_1$ in A8-35 after initial solubilization with PCC-a-M (lane 5). Bands observed in the density gradient fractions are indicated with red arrows. **(b)** Negative-stain 3D classes of supercomplex particles purified by density gradient after initial solubilization with digitonin (upper panel) and PCC-a-M (lower panel). In the first case, a mixture of supercomplexes $I_1III_2IV_1$ and I_1III_2 is observed, while in the second sample only respirasome classes are retrieved.

concern since data acquisition was a major limiting step in the project.

Since it seemed possible that at least a fraction of the population of supercomplex I_1III_2 originated from a partial disassembly of the respirasome, use of other detergents was considered for sample optimization. PCC-a-M (trans-4-(trans-4'-propylcyclohexyl)cyclo-hexyl-α-D-maltoside) is a non-ionic detergent, designed by Hovers and co-workers (Hovers et al., 2011) to be mild and, therefore, a good alternative to digitonin. The new detergent at a concentration of 0.11 % (w/v) could solubilize the mitochondrial membranes while preserving the association of respiratory complexes in larger assemblies (Figure 20a). Notably, the BN-PAGE profile of PCC-a-M-solubilized mitochondria shows clear differences to the one obtained when using digitonin; the second highest band runs at lower molecular weight than the band of supercomplex I_1III_2, whereas a band at the level of the respirasome is still observed. To confirm
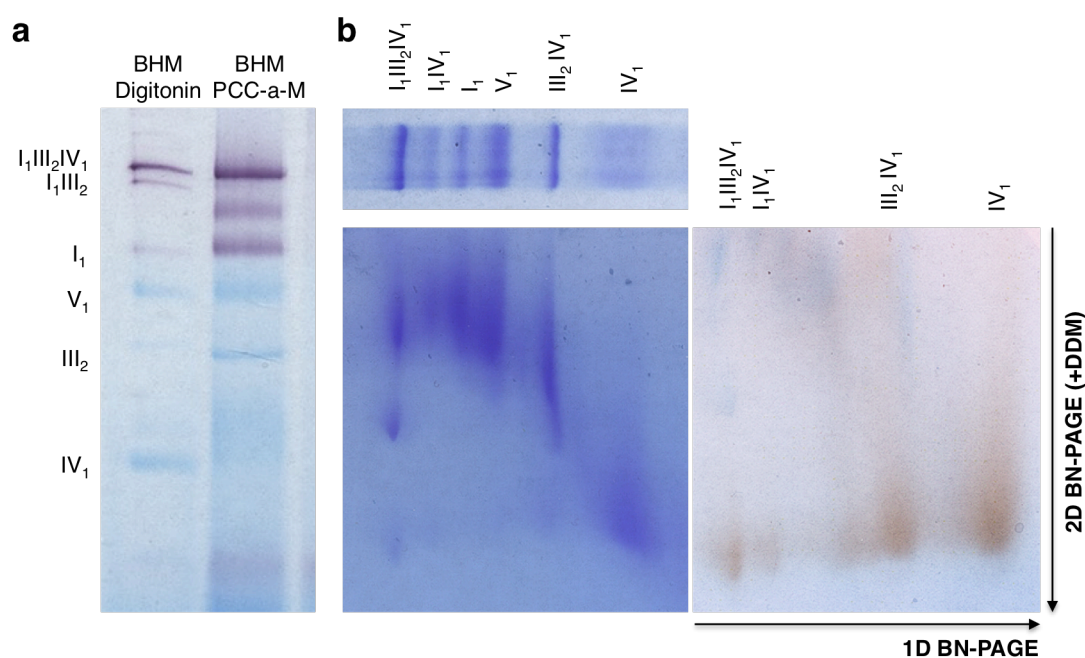
Figure 21. (a) In-gel activity assay for NADH:dehydrogenase in BN-PAGE gel. Purple bands are consistent with the presence of active complex I. **(b)** 2D BN/BN-PAGE gels of mitochondria solubilized with PCC-a-M, stained with Coomassie (left) or by cytochrome *c* oxidase activity (right). The largest assembly on PCC-a-M-solubilized mitochondria dissociates in three components, with the smaller one being active complex IV.

the nature of each of these bands, 2D BN/BN-PAGE and in-gel activity assays for complex I and complex IV were performed (Figure 21). The largest assembly is shown to be an active supercomplex that dissociates in complexes I, III and IV in presence of DDM, while the second highest band seems to be composed of complexes I and IV. Mitochondria solubilization with PCC-a-M produced, in this way, a sample enriched in the respirasome and for which contamination by smaller supercomplexes was minimized (Figure 20b), since the greater difference in molecular weight facilitates their separation from the respirasome.

It was previously shown (Althoff et al., 2011) that purification of the respirasome by density gradient centrifugation is improved in detergent-free systems. Therefore, after solubilization with PCC-a-M, the mitochondrial complexes were transferred to amphipol A8-35 by addition of γ-cyclodextrin. Evaluation of gradient fractions by BN-PAGE and negative-stain indicated high purity of the respirasome sample (Figure 20). This purification strategy was adopted for the following structural study.

4.2. Single-particle cryo-EM analysis of mitochondrial supercomplexes

A fresh sample of respirasome in amphipol A8-35 was used for preparation of cryo-EM grids. Electron micrographs were manually acquired and picked, for a total of 156,519 particles in the initial dataset (Figure 22a). Sequential rounds of 2D and 3D classification were used to isolate homogeneous sets of particles (Figure 22b,c). This characterization of the respirasome sample established three populations of supercomplexes that were refined to medium resolution maps: two distinct respirasome assemblies (class 1 at 9.1 Å – Figure 22d,e – and class 2 at 10.4 Å) and one supercomplex I_1III_2 (class 3 at 9.9 Å).

In addition to the integral supercomplex populations, classes of respirasome with no density for the NADH:dehydrogenase module of complex I, or even for the whole matrix arm (30% of the initial dataset), and a class of free complex I (15%) were also identified by the classification routines (Figure 22c). Such heterogeneity was not observed by negative-stain EM, suggesting that these
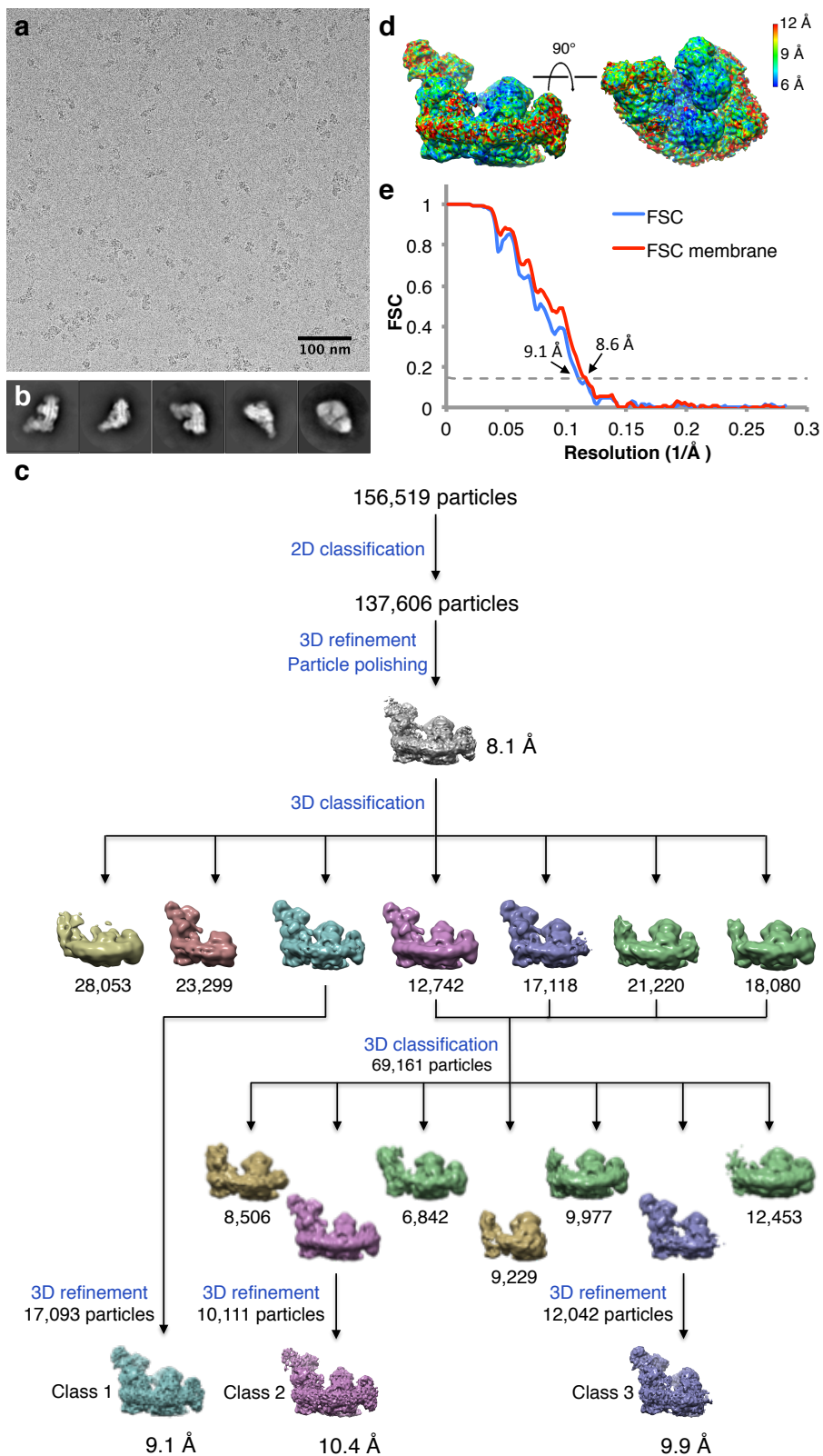
Figure 22. (a) Electron micrograph of bovine respirasome in vitrified buffer, recorded with a Falcon III camera in integrating mode on a FEI Tecnai Polara operating at 300 kV. **(b)** Representative 2D class averages produced by reference-free 2D classification with Relion. **(c)** Schematic representation of the image processing strategy used. (continue on next page)

assemblies result from partial denaturation or dissociation of the respirasome on the cryo-EM grid, prior to freezing. This is most likely the case for the supercomplex I_1III_2 as well.

4.3. Protein-protein contacts in the respirasome and supercomplex I_1III_2

Class 1 of the respirasome (EMD-4107, 5LUF; Figure 23) includes 11% of the particles and represents the most homogeneous population in the sample. Each of the component complexes is well resolved, allowing accurate docking of atomic models for complexes I (Vinothkumar et al., 2014), III (Iwata et al., 1998) and IV (Tsukihara et al., 1996). Complex III is located at the concave side of the membrane arm of complex I and the quinol-binding site of its inner protomer faces the quinone-binding site of complex I. Complex IV extends into the cleft formed by complex III and the end of the membrane arm of complex I. The transmembrane region of class 1, at an estimated local resolution of 8.6 Å (Figure 22e), shows clear densities for most of the 132 membrane spanning α–helices (Figure 23b).

The three component complexes are in close contact with each other. Interactions are established primarily by supernumerary subunits and near the membrane surfaces (Figure 23b). Complexes I and III show extensive interaction, established by both soluble and membrane subunits. In the matrix, subunit B22 of complex I and subunit 1 of complex III are found at a minimum distance of 4 Å. Within the membrane, the interaction is extended by contacts between subunit B14.7 of complex I and subunit 8 of complex III at both sides of the membrane

Figure 22 continued. In addition to the respirasome (dark cyan and pink), different populations of particles were identified by 3D classification, including free complex I (salmon), supercomplexes lacking subunits of complex I matrix arm (green and gold) and supercomplex I_1III_2 (violet and gold). Maps with similar architecture are depicted in the same color. **(d)** Class 1 map colored by local resolution estimated with RESMAP, as seen from the membrane (left) and from the matrix (right). **(e)** Gold-standard FSC plot of the respirasome class 1 map (blue) and its membrane domain (red). Resolution estimated at FSC=0.143.
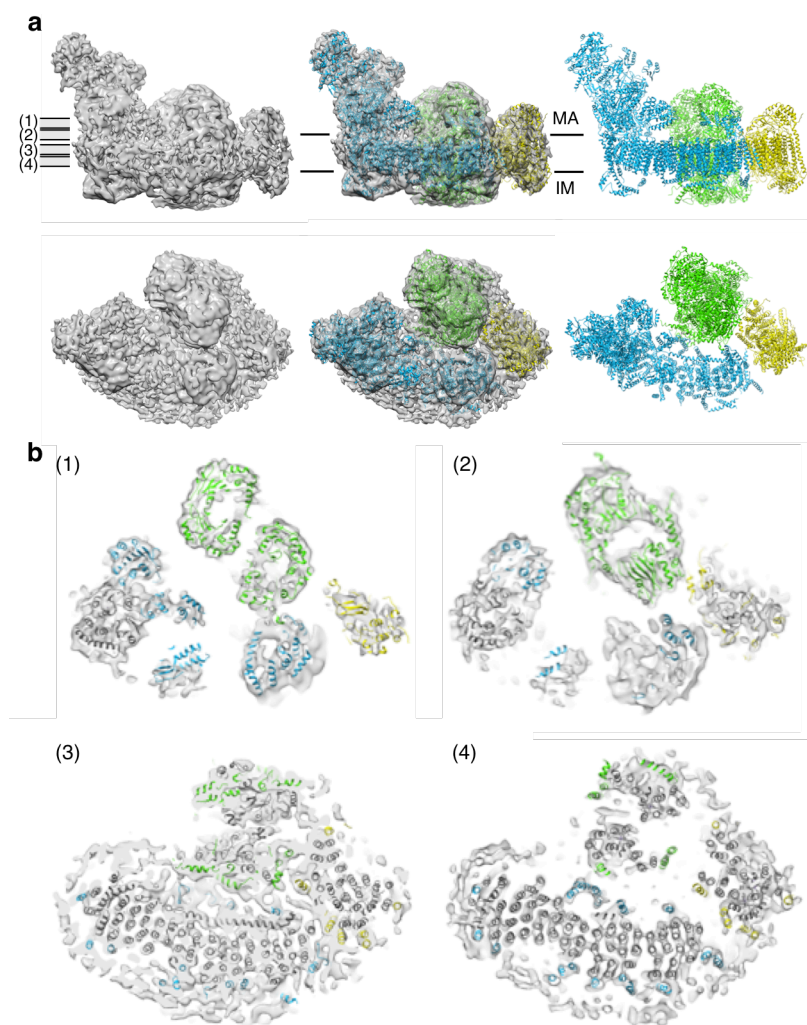
Figure 23. (a) Cryo-EM map of class 1 filtered to 8.6 Å (left) with docked atomic models (middle and right) of complexes I (blue), III (green) and IV (yellow), as seen from the membrane (upper row) and matrix (bottom row). **(b)** Class 1 sections at the positions indicated in (a), showing contact points between the component complexes. Supernumerary subunits are shown in the same color used for the respective complex in (a) and core subunits are depicted in grey.

(Figure 24). The association of complexes I and IV is defined by contacts between subunit ND5 of complex I and subunit COX7C of complex IV that align at an α–carbon distance of approximately 10 Å, at the matrix side of the membrane. ND5 appears to be the only core subunit within the respirasome to participate directly in the formation of this supramolecular assembly. Contacts between complex III and complex IV are mediated by subunit COX7A1 of the latter and subunits 1, 9 and 10 of the inner protomer of the dimeric bc_1 complex. This
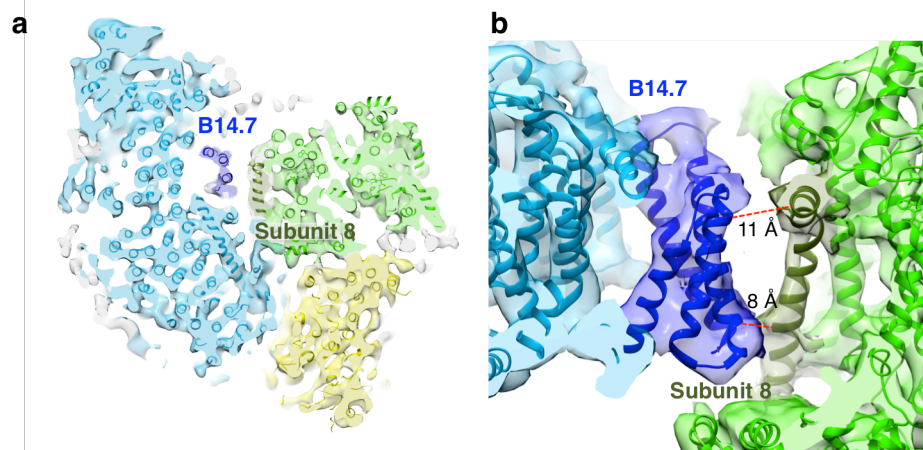
Figure 24. (a) Slice through class 1 map, through a plane parallel to the membrane, with docked models of complexes I (light blue), III (light green) and IV (yellow). **(b)** Zoomed-in view of the interface between subunit B14.7 of complex I (dark blue) and subunit 8 of complex III (dark green). The distances indicated were measured between α-carbons.

agrees with the previous report of an essential role for subunit 9 of complex III in the interaction with complex IV (Zara et al., 2007).

Approximately 6% of the particles clustered in a second class of supercomplex $I_1III_2IV_1$ (class 2, EMD-4108). This class, already observed in negative-stain datasets, differs from class 1 in the relative arrangement of complexes III and I, while the position of complex IV remains unchanged (Figure 25a); a rigid-body rotation of approximately 25° of the complex III dimer relative to complex I, around an axis roughly perpendicular to the membrane plane, disrupts the protein-protein contacts observed in class 1 between complex III and the other component complexes. Class 2 is most likely introduced during solubilization with PCC-a-M, as the detergent seems to be particularly harsh to complex III inter-complex contacts; with no significant new interactions being established, this represents a less stable state of the respirasome. In addition to the major displacement of complex III, in class 2 the matrix arm of complex I has moved away from the center of the supercomplex by a rotation of 3-4° around an axis parallel to the membrane (Figure 25b). An identical translation of the matrix arm observed in a single-particle cryo-EM study of bovine complex I was suggested to

reflect transitions between the active and deactive states of the complex (Zhu et al., 2016).

The map of supercomplex I_1III_2 (class 3, EMD-4109) arises from 8% of the particles in the initial dataset and shows clear density for both the component complexes. The mutual arrangement of complex I and complex III in this class is similar to the one in class 1 (Figure 25a), corroborating that this is a stable conformation, maintained solely by the specific interactions between the two complexes.
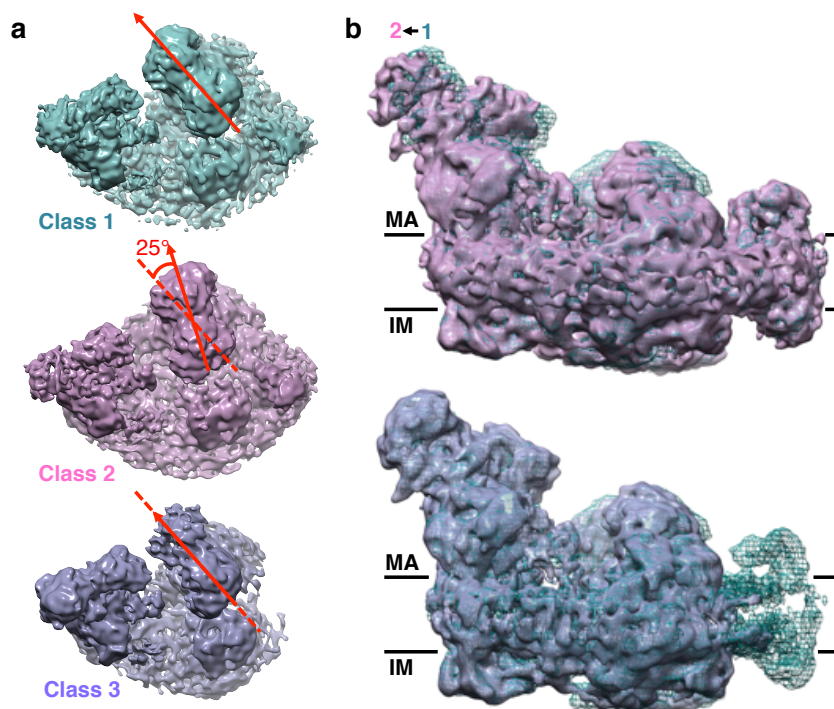
Figure 25. (a) View from the matrix of respirasome's classes 1 (dark cyan) and 2 (pink), and supercomplex I_1III_2 (violet). Classes 1 and 2, differ by a 25° rigid-body rotation in the membrane plane of complex III relative to complex I. **(b)** Superposition of class 2 (top) and class 3 (bottom) with class 1 (dark cyan mesh) reveals flexibility of complex I matrix arm.

4.4. Asymmetry of complex III in the respirasome

Inherent flexibility of a protein or protein complex is likely to limit the achievable resolution by single-particle cryo-EM analysis. Several strategies are

in place to deal with such challenging targets, pushing the resolution limits and, more importantly, giving us a more comprehensive view on the dynamics that underlie the activity of these proteins. Previous work on complex III established that large movements (10-15 Å) of the two membrane-extrinsic iron-sulfur domains occur in normal turnover conditions (Iwata et al., 1998). These iron-sulfur domains are the active part of the Rieske protein subunits that carry electrons from the Q_P site to heme c_1, where they are transferred to the small, soluble cytochrome c protein (Sousa et al., 2018a). The hinge movement of the iron-sulfur domains is critical for efficient electron transfer to cytochrome c_1 and, therefore, for complex III activity (Darrouzet et al., 2000). It is, for this reason, expected that these domains would be invisible in a 9 Å map. Surprisingly, this is not the case in the respirasome map, where one of the protomers of complex III shows clear density for its iron-sulfur domain (Figure 26). The asymmetric behavior of the two iron-sulfur domains in the respirasome suggests that one of the complex III protomers is inactive. The inactive protomer, in contact with the well-defined iron-sulfur domain, occupies a peripheral position in the supercomplex and is largely exposed to the lipid bilayer. The inner protomer, surrounded by complex I, complex IV and the
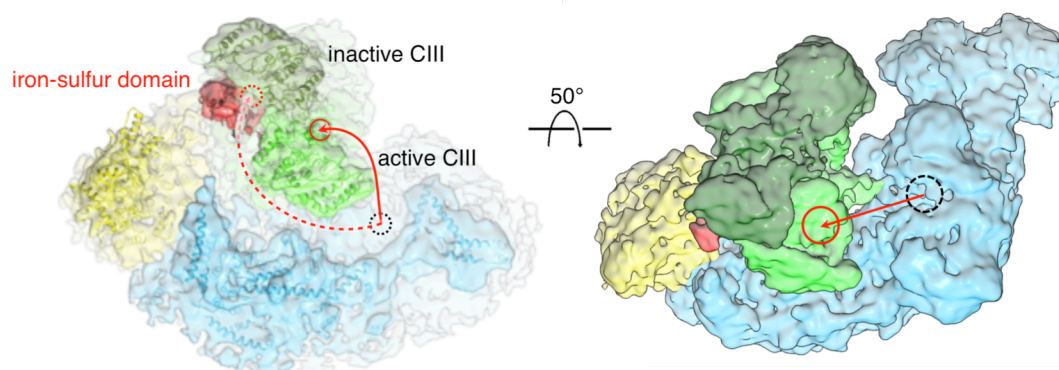
Figure 26. Respirasome map with fitted atomic models (complex I, blue; complex III, green; complex IV, yellow) seen from the cristae lumen (left) and at an angle (right). The resolved Rieske iron-sulfur domain of complex III is shown in red and the active and inactive protomers are depicted in light and dark green, respectively. The red circles indicate the approximate position of the quinol-binding sites in complex III, while the black circle indicates the position of the quinone-binding site in complex I.

inactive protomer of complex III, is located near the unresolved iron-sulfur domain and can be, therefore, assumed to be active.

5. Discussion

5.1. Isolation and characterization of respiratory supercomplexes

Most detergents routinely used for isolation of membrane proteins destabilize the interactions between respiratory complexes; the existence of supercomplexes in mitochondria was only reported in 2000 by Schägger and Pfeiffer, after solubilization with the particularly mild detergent digitonin (Schägger and Pfeiffer, 2000). Analysis by BN-PAGE of the digitonin-solubilized mitochondria revealed the presence of several supramolecular assemblies of defined stoichiometry, of which the respirasome (or supercomplex $I_1III_2IV_1$) deserves special note, as it contains all the complexes required to "respire". Another abundant assembly in this preparation was supercomplex I_1III_2. Originally this assembly was contemplated as a possible degradation product of the respirasome, resulting from dissociation of complex IV during solubilization. Later *in situ* analysis by subtomogram averaging showed that significant levels of supercomplex I_1III_2 are present in the mitochondrial membrane (Davies et al., 2018).

The molecular weight of supercomplex I_1III_2 makes it a likely contaminant in respirasome preparations. Solubilization of the mitochondrial membranes with PCC-a-M proved to minimize the presence of supercomplex I_1III_2 and give rise to an assembly of complex I and complex IV only (I_1IV_1; Figure 21). This supramolecular assembly is most likely a detergent-specific artifact, created by dissociation of complex III from part of the respirasome population. The specific destabilization of the contacts between complex III and the other component complexes by PCC-a-M explains also the absence of a supercomplex I_1III_2 (Figure 20) that most likely dissociates to individual complexes, and the presence of a respirasome class with complex III in a second conformation (Figure 25). Despite the harshness of PCC-a-M towards complex III interactions, biochemical and negative-stain analyses of the purified sample proved it to have lower contamination rates by smaller (super)complexes (Figure 20).

The homogeneity observed in the preliminary characterization of the sample did not translate in a uniform cryo-EM dataset; a large ensemble of structures with

different compositions and conformations reduced the respirasome population to a small fraction of usable particles (Figure 22c). Supercomplex I_1III_2 and complex I were present in the dataset, corroborating the fragile nature of the inter-complex interactions in the respirasome that appear to be destabilized by the conditions for cryo-grid preparation. Free forms of complexes III and IV, if present on the images, were excluded during particle picking, as they did not fit the target dimensions. Dissociation of the respirasome in its component complexes might have occurred on the grid upon an increase of the ionic strength due to evaporation. Degradation of the sample by interaction with the air-water interface is also a prominent problem in cryo-EM; it has been shown that the vast majority of the particles on a cryo-grid are located at the air-water interface and that denaturation can be induced at the contact surfaces (Noble et al., 2018). These forces might be responsible for the significant portion of respirasome particles with no density for part or all the matrix arm of complex I. However, we cannot rule out that these structures might represent a relevant state of respiratory supercomplexes (see 5.3. Respirasome and complex I).

In order to overcome the inherent flexibility and instability of the bovine (super)complexes and improve the resolution of the maps two main strategies could have been pursued: automation of data acquisition and use of coated grids (carbon, graphene, graphene oxide) or detergents to reduce issues related with the air-water interface.

5.2. Mammalian respiratory supercomplexes

Even though the bovine respiratory complexes have been the most studied among mammals, screening of other homologues proved crucial for the identification of better candidates for structural characterization. Since we first determined the structure of the bovine respirasome, other groups published similar cryo-EM maps for different mammalian supercomplexes (Guo et al., 2017; Letts et al., 2016; Wu et al., 2016). Substantial heterogeneity was observed across all these studies, with sub-populations of supercomplex I_1III_2 being a constant. A small subset of particles composed of two copies of complex I, a

complex III dimer and two copies of complex IV was also identified in a study of the human respirasome (Guo et al., 2017). The low-resolution map of this so-called megacomplex shows a two-fold symmetrical particle, where the complex III dimer is flanked by the other four component complexes. This supramolecular assembly has not been observed in mitochondrial membranes (Davies et al., 2018), being unclear at this point if it represents a physiologically relevant respiratory supercomplex.

As in the case of the bovine sample, Letts and co-workers identified two respirasome conformations in an ovine preparation (Letts et al., 2016). The two states, referred to by the authors as "tight" and "loose", diverge mostly by a relative movement of complex IV. In the tight state, defined contacts between complex IV and the other two component complexes are observed, while in the loose state complex IV interacts only with complex I (Letts et al., 2016). A small displacement of complex III away from complex I is visible in the loose conformation. The arrangement of the component complexes in the loose state differs considerably from our class 2. In both these minor classes, interactions between complexes are disrupted, and in the case of the ovine sample the ratio of loose to tight respirasome was found to increase over time (Letts et al., 2016). This suggests that the loose state of the ovine supercomplex, as class 2 of the bovine respirasome, results most likely from destabilization of the inter-complex interactions during and after purification. The tight state of the ovine supercomplex and class 1 of the bovine respirasome are essentially the same and so must represent the native and most stable association of the component complexes. *In situ* structural analysis of supercomplexes in mammalian mitochondria corroborated this arrangement of the respirasome, amongst other assemblies (Davies et al., 2018).

Notably, in the maps of the ovine, porcine and human respirasome both iron-sulfur domains in the complex III dimer are resolved, which implies that none of these structures shows a mobile, and therefore active, Rieske domain. This observation contrasts with the asymmetric behavior of complex III in our bovine respirasome map (see 5.4. Functional asymmetry and electron flow in the respirasome).

5.3. Respirasome and complex I

The relevance of supercomplexes in mitochondrial physiology has been debated at great length since their discovery. Our map of the bovine respirasome shows that the association of respiratory complexes into supercomplexes is driven by defined protein-protein contacts, mainly concerning the supernumerary subunits. This structure may now help us to understand several mitochondrial genetic disorders that have their origin in point mutations of subunits of the component complexes (Rodenburg, 2016; Meunier et al., 2013).

Stabilization of the individual complexes within supercomplexes has been one of the advantages proposed by the community for these structures. In particular, it has been proposed that association with complex III might be required for stability or assembly of complex I. Clinical cases and biochemical studies of co-deficiencies of complexes III and I, where a point mutation or truncation of complex III subunits promotes the secondary loss of complex I, support this hypothesis (Acín-Pérez et al., 2004; Bruno et al., 2003; Lamantea et al., 2002; Schägger et al., 2004). In agreement, the respirasome maps discussed here show that the contacts between complexes I and III are extensive. Interestingly, one of the subunits identified as necessary for the association of these complexes is the nuclear-encoded, supernumerary subunit B14.7 of complex I; a point mutation of this subunit has been described to cause complex I deficiency in patients with fatal infantile lactic acidemia (Berger et al., 2008), and disruption of the gene of the homologous protein in *Neurospora crassa* is associated with incomplete assembly of complex I (Nehls et al., 1992). Such extreme outcomes were difficult to understand, as supernumerary subunits are, by definition, non-essential for catalysis. However, in the light of the respirasome structure, the significance of complex I B14.7 (and other accessory subunits) becomes indisputable. In this case, the loss of complex I might be understood on the basis of its destabilization or incomplete assembly, due to deficient interaction with complex III.

The respirasome particles lacking density for the distal part of the matrix arm of complex I present in our dataset must also be discussed, since they cannot be excluded as possible intermediates in the normal turnover of supercomplexes. A

study by Moreno-Lastres and co-workers suggested that respirasome biogenesis requires an initial association of complexes III and IV with an immature form of complex I lacking N-module subunits; incorporation of these subunits would follow at the late stages of the assembly pathway (Moreno-Lastres et al., 2012). Concurrent with the *de novo* assembly of complex I, it has been shown that mature complex I can exchange several of the nuclear-encoded, N-module subunits by newly imported copies (Dieteren et al., 2012; Lazarou et al., 2007). A direct replacement of the N-module subunits provides an efficient way for repairing oxidative damage (Dieteren et al., 2012; Lazarou et al., 2007), to which these proteins are particularly susceptible. In this background, the experimental respirasome reconstructions with incomplete densities for the complex I matrix arm could represent intermediates of the supercomplex generated during its assembly, disassembly or complex I regeneration.

5.4. Functional asymmetry and electron flow in the respirasome

In the several crystal structures of complex III, the positions occupied by the iron-sulfur domains can reflect the occupancy of the Q_P site but may also result from regular contacts (Berry et al., 2013). Single-particle cryo-EM is not affected by such contacts and, therefore, can give us a potentially unbiased view of the conformational landscape of the protein. In our map of the respirasome, density for one of the iron-sulfur domains from the complex III dimer is absent, as a result of averaging particles where this occupies different positions, adopted during catalysis. The iron-sulfur domain from the other protomer is well resolved and so does not undergo the large conformational change required for the transfer of electrons from the Q_P site to heme c_1. It has been shown that, despite being an obligatory dimer, under normal turnover conditions the two protomers of complex III are not active simultaneously since the activity is not altered if one of them is permanently inactivated by mutagenesis (Castellani et al., 2010). Electron transfer within complex III was for this reason proposed to occur by random activation of either protomer (Covian and Trumpower, 2008), with two equivalent electron transfer branches that switch between active and

inactive states. Even if this model might hold true for free complex III, our respirasome structure shows that within a supercomplex the dimer behaves asymmetrically and the alternating activation model does not apply. The structural data presented implies that in the respirasome the inner protomer of complex III preferentially catalyzes quinol oxidation, since the movement of the iron-sulfur domain associated with the outer protomer is restricted. Concurrently, quinone reduction may take place at either protomer, as electrons can equilibrate quickly between the two b_L hemes (Castellani et al., 2010). It is possible though that the outer protomer acts exclusively as a scaffold, not participating in the catalysis.

In the respirasome, the quinol oxidation site of the inner, active protomer of complex III is aligned with the quinone entry channel of complex I, from where quinol is released after receiving the electrons donated by NADH. The shortest distance between the two sites is of approximately 11 nm (Figure 26). The quinol oxidation site on the outer, inactive protomer faces the membrane on the far side of the dimer and the shortest unrestricted path to the quinone-binding site of complex I is of at least 18 nm. Consequently, a quinol diffusing through the lipid bilayer from complex I to complex III would more likely encounter the active protomer first. Enhanced catalysis and efficiency of electron transfer has been proposed to occur within the respirasome by substrate channeling. The existence of substrate channeling and of distinct quinone pools has been challenged (Blaza et al., 2014; Fedor and Hirst, 2018), but it finds support in numerous studies of metabolic flux control (Bianchi et al., 2003; Lapuente-Brun et al., 2013) and in reviews discussing the results of Blaza et al. (Enríquez, 2016; Lenaz et al., 2016). While a confined pathway is not observed between the quinol sites in complex I and the inner protomer of complex III, the arrangement of these two component complexes in the respirasome seems to be particularly favourable for direct substrate transfer. Therefore, even if strict substrate channeling might not take place, our map suggests that a short diffusion of quinol from complex I to the nearest quinol oxidation site is favoured (Figure 27). Significantly, in the megacomplex structure, the quinol oxidation sites of both complex III protomers are well-placed to accept reduced quinol from the neighboring complex I. The

functional asymmetry observed for complex III in our respirasome map provides further support for a kinetic advantage of these structures.
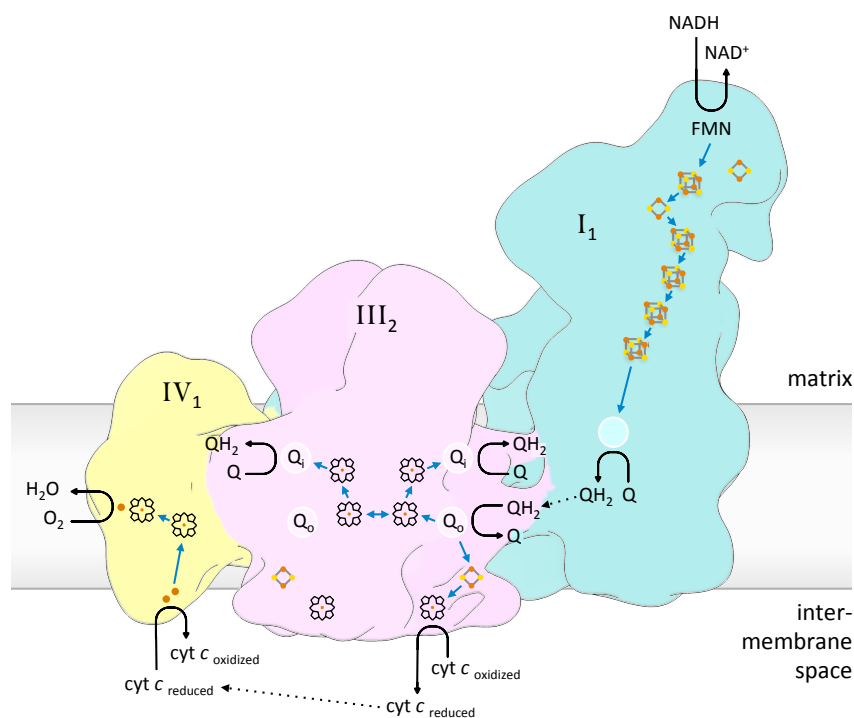
Figure 27. Schematic representation of electron and substrate transfer in the respirasome, showing that quinol oxidation occurs preferentially at the inner protomer of complex III. Complexes I, III and IV are depicted in blue, pink and yellow, respectively. Quinone and quinol binding sites are represented by circles. Blue arrows, dotted arrows and black arrows indicate transfer of electrons, diffusion of substrates and reactions, respectively.

6. Conclusions

The 9 Å structure of the mammalian respirasome confirms that specific interactions maintain the respiratory chain complexes I, III and IV associated in a well-defined architecture. The relative position of component complexes plays an essential role in the electron transfer and establishes the inner complex III protomer as the primary point for quinol oxidation.

Subsequent structural analysis of supercomplexes in mitochondria from mammals, yeast and plants by subtomogram averaging revealed a wide spectrum of assemblies within each species and across kingdoms (Davies et al., 2018). Interestingly, the variations observed exclusively concern complex IV. The conserved arrangement of complex I and complex III across such a vast selection of organisms argues in favor of directed quinol transfer, as we propose. Even though no megacomplexes were observed in mitochondrial membranes to date, such a structure would suggest that each protomer of complex III is dedicated to oxidation of quinol produced by the adjacent complex I.

The data acquired during this study provides in this way pioneering support for the optimization of electron flow in cellular respiration by association into ordered supramolecular assemblies. Further studies are required to comprehend all aspects of respiratory supercomplexes, including extensive *in situ* structural studies to describe the full range of these assemblies.

CHAPTER II

7. Introduction

7.1. Bacterial respiratory chains

The respiratory chain is classically viewed as a sequential arrangement of four electron transfer complexes, known as complex I to IV (see *2. Introduction, Chapter I*). However, in many prokaryotes the respiratory chain's composition and organization diverge greatly from the mitochondrial model. In bacteria, respiratory chains can be branched, modular and inducible; frequently the canonical complexes are complemented or replaced by alternative enzymes with identical catalytic activity. Alternative complexes may switch between, or concurrently use, different electron donors and acceptors. This feature underpins the flexible metabolism that allows bacteria to adapt to changing and contrasting environments and to survive and grow under conditions that sustain no other life forms.

Bacterial respiratory chains are formed by combination of five major modules: dehydrogenases, quinones, reductases, cytochromes and terminal oxidases (Figure 28). At the beginning of the redox chain, a dehydrogenase oxidizes a substrate, such as NADH, succinate, formate, lactate, glycerol-3-phosphate, pyruvate and hydrogen, by transferring hydrogens to an electron acceptor (Shepherd and Poole, 2013). In particular, quinone reductases catalyze the reduction of an isoprenoid quinone to its quinol (hydroquinone) form by delivering two electrons and two protons. The quinone pool is responsible for shuttling electrons and protons from the dehydrogenases to (electron carrier) reductases or ubiquinol oxidases. These quinones are highly diversified, varying in the length of their isoprenyl chain, composition of aromatic ring (Collins and Jones, 1981) and reduction potential (Marreiros et al., 2016).

Under anaerobiosis, reductases mediate the transfer of electrons from quinol to an inorganic or organic final electron acceptor, such as sulfate, carbon dioxide, nitrate, nitrite, TMAO (trimethylamine N-oxide) and DMSO (dimethyl sulfoxide).

65

In the presence of oxygen, two routes are possible. The first involves the reduction of a second, periplasmic electron carrier and its subsequent oxidation by an electron carrier oxidase. Another pathway leads to the oxidation of ubiquinol by ubiquinol oxidases. The terminal oxidases couple the oxidation of the electron carrier to the four-electron reduction of molecular oxygen to water (Poole and Cook, 2000). The different chain segments can consist of complexes that may, or may not contribute to the transmembrane electrochemical potential.
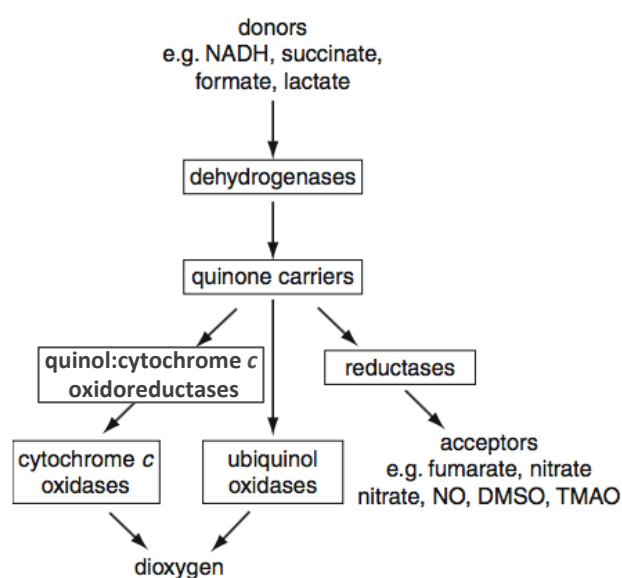
Figure 28. Generalized model of bacterial respiratory chains. Adapted with permission from Shepherd et al. (2013). Copyright © European Biophysical Societies' Association (EBSA) 2013.

7.2. Respiratory chain from Rhodothermus marinus

R. marinus was first isolated in Iceland in 1988 (Alfredsson et al., 1988) and later found in the island of S. Miguel in the Azores, Portugal (Nunes et al., 1992; Silva et al., 2000), in Stufe di Nerone, Italy (Moreira et al., 1996) and on the island of Monserrat in the Caribbean Sea (Silva et al., 2000). Despite the distance amongst these thermal sites, the *R. marinus* strains are closely related (Bjornsdottir et al., 2006).

R. marinus belongs to the *Bacteroidetes* phylum, class *Sphingobacteria* and family *Crenotrichacea* (Garrity et al., 2004). This bacterium is moderately halophilic, gram-negative, rod-shaped and, as the name suggests, it is thermophilic, with an optimum growth temperature of 65 °C. *R. marinus* is also an obligate aerobe and, therefore, its growth is restricted to a narrow area within shallow submarine hot springs where its temperature, salinity and oxygen requirements are met.

Even though the respiratory chain of *R. marinus* is not highly branched, it proved to be particularly interesting as early studies of the chain lead to the identification of an, until then, unknown respiratory complex. Since then, this respiratory chain has been extensively characterized and today we know that *R. marinus* has two dehydrogenases, a quinol:cytochrome *c*/HiPIP oxidoreductase and three cytochrome *c* oxidases (Figure 29).

R. marinus has a typical bacterial complex I (NDH-1 or NADH:quinone oxidoreductase) with 14 subunits and a total molecular mass of approximately 800 kDa. The activity of complex I is inhibited by rotenone and stimulated by dissipation of the transmembrane proton gradient, in agreement with its role in proton translocation (Fernandes et al., 2002). A second dehydrogenase uses
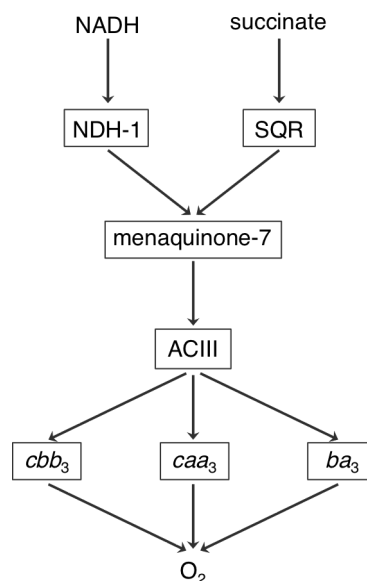
Figure 29. Respiratory chain of *R. marinus*.

succinate as its electron donor (succinate:quinone oxidoreductase or SQR). It is a canonical complex II, with three subunits that harbor three iron-sulfur clusters and two *b*-type hemes. This dehydrogenase does not contribute to the transmembrane difference of electrochemical potential and it has, in fact, been proposed to dissipate the proton gradient during catalysis (Fernandes et al., 2001). The main quinone in *R. marinus* membranes is menaquinone-7, with an unsaturated isoprenoid chain (Tindall, 1991). This is reduced to menaquinol by either dehydrogenase.

The existence of three cytochrome *c* oxidases in *R. marinus*, which are unable to receive electrons from quinol, imposes the need for a quinol:cytochrome *c* oxidoreductase that links the electron transfer from the dehydrogenases to the terminal oxidases (see Figure 28). However, no Rieske centers ([2Fe-2S] clusters) were detected in this bacterium (Pereira et al., 1994) and, consequently, cytochrome bc_1 (complex III; see 2.4. Complex III) must be absent. In *R. marinus*, oxidation of quinol is performed instead by alternative complex III (ACIII) (Pereira et al., 1999a). ACIII is expressed under different growth conditions and is highly abundant, as expected from its central role in this respiratory chain. The alternative complex is not inhibited by DBMIB, mixothyazol or antimycin A (Pereira et al., 1999a), typical inhibitors of the canonical complex III, and can reduce both cytochrome *c* and HiPIP (high potential iron-sulfur protein) (Pereira et al., 1999b).

The HiPIP from *R. marinus* is a small membrane-bound protein with a single [4Fe-4S] cluster. It has a reduction potential of +290 mV at pH 7.0, and it was shown to mediate electron transfer from ACIII to the terminal oxidases with a higher efficiency than cytochrome *c* (Pereira et al., 1994, 1999b). The cytochrome *c* from *R. marinus* is also bound to the membrane (Pereira et al., 1999b) and has been suggested to be part of a new class of cytochromes, specific of the *Bacteroidetes* phylum (Stelter et al., 2008).

All cytochrome *c* oxidases in *R. marinus* belong to the superfamily of heme-copper oxidases, which couple oxygen reduction to proton translocation. Members of this family share a central subunit with a low-spin heme and a

high-spin heme-copper binuclear center. The latter constitutes the catalytic site and varies between the established subfamilies. The major terminal oxidase in *R. marinus* is *cbb*$_3$, from the C-type subfamily. The *cbb*$_3$ oxygen reductase consists of five subunits, with two low-spin *c*-type hemes, a low-spin *b*-type heme and a *b*$_3$-Cu$_B$ center. HiPIP appears to be a poor electron donor to this oxidase, and the physiological substrate of the enzyme is still unknown (Pereira et al., 2000a). The second oxygen reductase, *caa*$_3$, belongs to the A2 subfamily of heme-copper oxidases. The *caa*$_3$ oxygen reductase from *R. marinus* is similar to the one expressed by *Thermus thermophilus*, where four subunits harbour one *c*-type heme, a binuclear Cu$_A$ center, an *a*$_3$-Cu$_B$ center and an *a*-type heme (Pereira et al., 1999c). This complex was shown to translocate protons from the cytoplasm to the periplasm according to a 1H$^+$/e$^-$ stoichiometry (Pereira et al., 2000b). The expression of the *caa*$_3$ oxygen reductase of *R. marinus* is increased in the presence of higher oxygen concentrations (Pereira et al., 2000a). This oxidase was also proposed to form a supercomplex with ACIII based on BN-PAGE analysis (Refojo et al., 2010a). The last terminal oxygen reductase in *R. marinus* is *ba*$_3$, of the B subfamily. This *ba*$_3$ oxidase is homologous to that from *Thermus thermophilus*. It is composed of two subunits, where the first one harbors an *a*$_3$-Cu$_B$ center and a low-spin *b*-type heme, while the second has a Cu$_A$ binuclear center (Veríssimo et al., 2007).

The respiratory chain of *R. marinus* illustrates well how the enzymes used by bacteria for energy production can deviate from the mitochondrial model and, more significantly, demonstrates that some bacteria have an alternative to the standard cytochrome *c* reductase, ACIII.

7.3. Alternative complex III

Cytochrome *bc*$_1$/*b*$_6$*f* complex, also known as complex III, is present in both organotrophs and lithotrophs and widespread in gram-negative, gram-positive, aerobic, anaerobic and photosynthetic bacteria (Trumpower, 1990). Maybe for this reason, complex III was for a long time believed to be the only quinol:cytochrome *c* oxidoreductase in biology. Since it was first recognized in

R. marinus membranes, ACIII has been shown to be widespread in Bacteria (Figure 30), participating in both respiratory and photosynthetic transport chains (Pereira et al., 1999a; Gao et al., 2010; Pereira et al., 1999b; Venceslau et al., 2010; Yanyushin, 2002; Yanyushin et al., 2005). Interestingly, *Chloroflexus aurantiacus* and *Oscillochloris trichoides* have two copies of ACIII, with one operon being expressed under aerobic growth and the other during photosynthetic growth (Majumder et al., 2013). ACIII typically replaces cytochrome bc_1, but in certain genomes both quinol:cytochrome *c* oxidoreductases are encoded (Figure 30), for example *Oscillochloris trichoides* (Refojo et al., 2010b; Majumder et al., 2013; Marreiros et al., 2016). It is possible that catalysis by either ACIII or complex III may be favored under specific metabolic demands.

The *act* cluster is composed of six to eight genes (Refojo et al., 2010b). In the case of *R. marinus*, this cluster encodes seven subunits: ActA, ActB, ActC, ActD, ActE, ActF and ActG (Pereira et al., 1999a, 2007; Refojo et al., 2010b; Refojo et al., 2012). None of the ACIII subunits is homologous with cytochrome bc_1 subunits, proving that ACIII and complex III are structurally unrelated complexes. The iron content of ACIII in *R. marinus* is estimated at 21 Fe per protein complex, of which six are part of *c*-type hemes and three form a [3Fe-4S] cluster; the remaining irons were proposed to belong to three [4Fe-4S] clusters (Pereira et al., 2007; Refojo et al., 2012). According to fluorescence quenching titration experiments with HQNO, an inhibitor that binds quinol oxidation sites, ACIII has one quinone-binding site (Refojo et al., 2010a), though existence of further quinone sites, and in particular quinone reduction sites, cannot be excluded.

ActA is a 27 kDa protein with five *c*-type heme-binding motifs (CXXCH); four additional strictly conserved histidines (H54, H57, H129 and H132) and a methionine (M160) are believed to serve as the second axial ligand. At its N-terminus, ActA has one predicted TMH, which is present in the mature protein according to N-terminal amino acid sequencing results (Pereira et al., 2007; Refojo et al., 2010b).
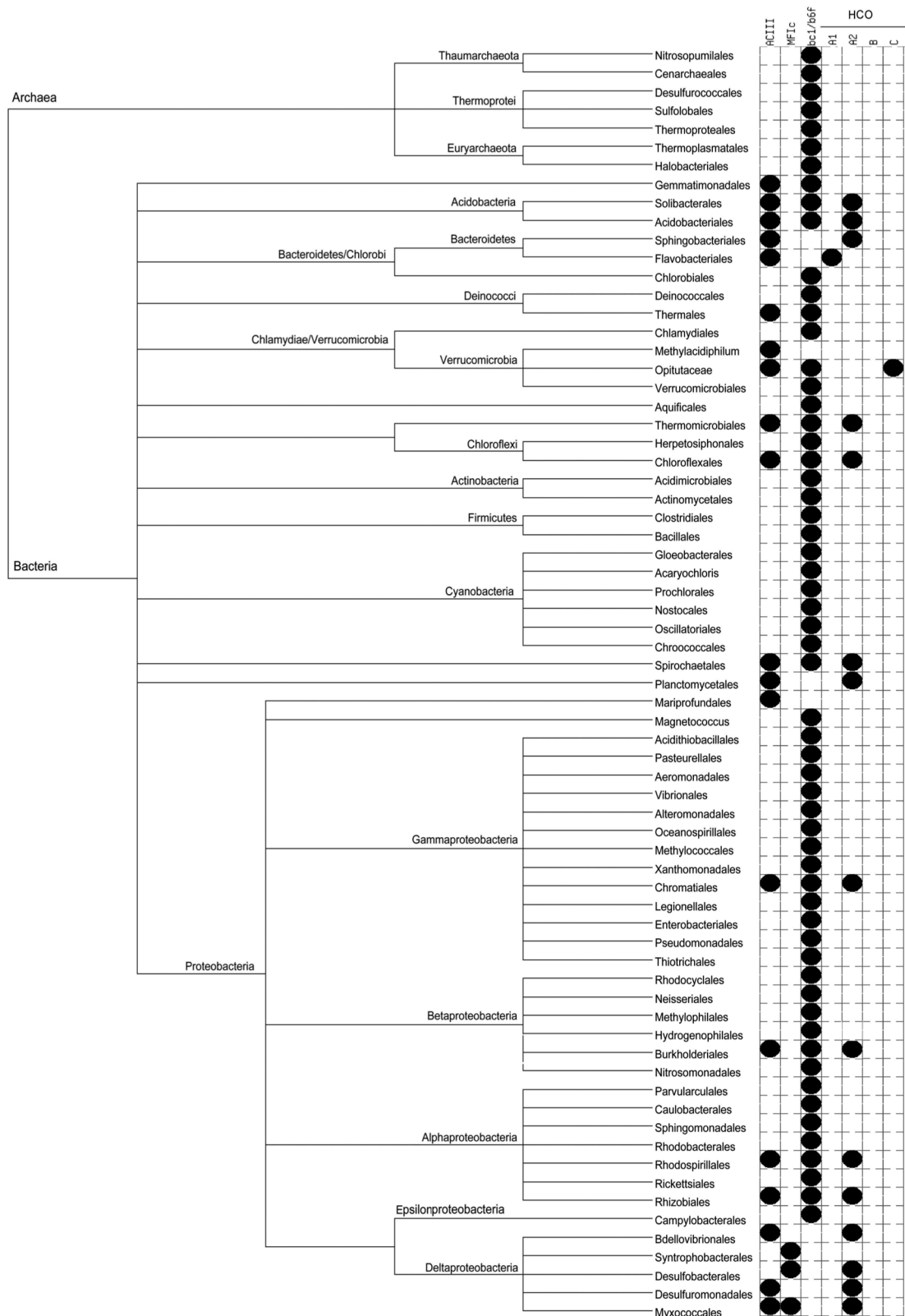
Figure 30. Phylogenetic profile for aerobic organisms of the presence of ACIII, MFIc complex and cytochrome bc_1/b_6f. The type of heme-copper reductases (HCO) encoded by the gene cluster that follows the one of ACIII is also indicated. Reproduced with permission from Refojo et al. (2010). Copyright © 2010 Elsevier B.V.

In some genomes, ActB is split between two genes that encode ActB1 and ActB2. In *R. marinus*, the two domains have fused into a single chain of 117 kDa. The N-terminal domain B1 and the C-terminal domain B2 are homologous to the molybdopterin-guanine dinucleotide-containing subunit and the iron-sulfur containing protein of the CISM (complex iron-sulfur molybdoenzyme) family, respectively. However, the molybdenum-cofactor binding residues are not conserved in ActB and ACIII does not contain molybdenum. The amino acid sequence of domain B2 shows three binding sites for [4Fe-4S] clusters and one binding site for a [3Fe-4S] cluster (Pereira et al., 2007; Refojo et al., 2010b, 2012). The orientation of ActB relative to the membrane has been debated; while a twin arginine translocase (Tat) signal peptide suggests it to be imported to the periplasm (Refojo et al., 2012; Yanyushin et al., 2005), cross-linking data from *Chloroflexus aurantiacus* places ActB in the cytoplasm (Gao et al., 2010).

ActC is a 55 kDa protein with ten predicted TMHs. It has homology with transmembrane subunits of members of the CISM family, such as PsrC, NrfD and DmsC. Existence of quinone-binding sites in ActC has been proposed (Pereira et al., 2007; Refojo et al., 2010b; Yanyushin et al., 2005).

The subunit encoded by *actD* is a 25 kDa membrane protein, with two predicted TMHs in *R. marinus*. ActD has no homologues in other respiratory enzymes, being specific to ACIII (Pereira et al., 2007; Refojo et al., 2010b) and is in some genomes fused with ActE (Majumder et al., 2013).

ActE is a monohemic cytochrome of 22 kDa and its *c*-type heme has the highest redox potential within ACIII. A strictly conserved methionine (M164) was suggested to be an axial ligand of the heme (Refojo et al., 2012). ActE has low homology with other monohemic *c*-type cytochromes and, in particular, bears no similarities with the *c*-type cytochromes of the bc_1/b_6f complexes (Pereira et al., 2007; Refojo et al., 2010b, 2012). ActE has a lipobox (residues 21 to 24 in *R. marinus*) that should allow a cysteine (C24 in *R. marinus*) to covalently bind a lipid upon post-translational modification (Refojo et al., 2017). The monohemic subunit was shown to be necessary for the oxidoreductase activity of ACIII from *Chloroflexus aurantiacus* (Gao et al., 2013) and to reduce the *caa₃* oxygen

reductase directly, being a more efficient electron donor than either cytochrome *c* or HiPIP (Refojo et al., 2017). Accordingly, and considering its high redox potential, ActE has been proposed to be the terminal member of the electron transfer wire in ACIII.

ActF is a 48 kDa membrane protein, homologous to ActC. Like ActC, ActF is predicted to have ten TMH and might harbor one or more quinone-binding sites (Pereira et al., 2007; Refojo et al., 2010b, 2012). While in most species ACIII has both ActC and ActF, in some cases the complex lacks the latter (Majumder et al., 2013).

ActG is a small 15 kDa subunit whose gene is present only in some *act* gene clusters. Topology predictions suggest that ActG has one N-terminal TMH and a periplasmic C-terminal domain (Refojo et al., 2010b, 2012).

ACIII has been intensively studied for the last two decades and genetic and biochemical data has accumulated to show that this is an original respiratory complex, relevant in many bacteria. No structural studies of ACIII had been performed before and several fundamental questions remained unanswered regarding the number and location of quinone-binding sites, intra-protein electron transfer, electrogenic nature of the complex and overall architecture. Using single-particle cryo-EM, I determined a 3.9 Å map of ACIII from *R. marinus* and modeled the first structure of ACIII, which provides essential insights into its catalytic mechanism.

8. Methods

8.1. Protein purification

ACIII was purified by Filipa Calisto, from the group of Dr. Manuela Pereira, at ITQB, Universidade Nova de Lisboa from *R. marinus* membranes as described previously (Pereira et al., 1999a, 2007). Aliquots of purified ACIII in 20 mM Tris-HCl pH 8, 150 mM NaCl and 0.05% DDM were stored at –20 °C. A detailed description can be found in Sousa et al. (2018).

8.2. Negative-staining and initial model generation

ACIII was negatively stained with 1% (w/v) uranyl acetate, pH 4 as described before (see 3.3. Negative-staining). Electron micrographs were recorded on a Tecnai Spirit operating at 120 kV with a CCD camera (Gatan Ultrascan 4000) at a magnification of 51,000x, corresponding to a pixel size at the specimen of 2.34 Å. Approximately 2000 particles were picked manually with EMAN boxer (Ludtke et al., 1999) and 25,848 automatically with Gautomatch, after generation of adequate templates by 2D classification with Relion 1.4 (Scheres, 2012). Reference-free 2D classification of the larger dataset in Relion 1.4 produced several 2D class averages with distinctive features. The best 2D classes were used for generation of a first initial model using EMAN2 (Tang et al., 2007).

8.3. Single-particle cryo-EM specimen preparation and data collection

Cryo-EM grids were prepared in an FEI Vitrobot plunge freezer at 10 °C and 90% humidity, using C-Flat multihole holey carbon grids (Electron Microscopy Sciences), glow-discharged at 0.38 mbar and 15 mA for 90 seconds. 3 μl of a freshly thawed ACIII sample at a concentration of 1 mg/ml were applied to the grid for 3 seconds, blotted with filter paper #597 (Whatman) for 9 seconds at a blotting force of –2 and then quickly plunged into liquid ethane. Images were collected manually on a FEI Titan Krios at 300 kV, aligned as previously reported

(Mills et al., 2013), with a Gatan K2 Summit electron detector operating in counting mode and with an energy filter. Movie stacks with 40 frames were recorded over 8 seconds, at a nominal magnification of 135,000x, corresponding to a pixel size of 1.035 Å at the specimen, with a calibrated dose of 1.8 e$^-$/ Å^2 per frame, at defocus values from –0.6 to –4.0 μm.

8.4. Image processing and model building

A set of 2,479 movie stacks was preprocessed with MotionCor2 using a 5x5 grid (25 tiles), for motion correction and dose weighting according to the implemented pre-calibrated filtering scheme (Zheng et al., 2016). The micrograph-based CTF was determined with CTFFIND4 (Rohou and Grigorieff, 2015) on drift-corrected, non-dose weighted micrographs. Particles were picked manually using EMAN boxer (Ludtke et al., 1999) or automatically using the template-matching algorithm within Gautomatch (by Kai Zhang, MRC-LMB), and extracted with a box of 288 x 288 pixels. False-positive picks and low quality particles in the automatically picked dataset were identified by reference-free 2D classification with ISAC within Sphire (Moriya et al., 2017). A total of 131,995 particles composed the initial clean dataset. The subsequent classifications and refinements were performed in Relion 1.4 and 2.1 (Scheres, 2012). A second round of 2D classification was performed with the entire dataset. The particles in the best 2D classes were selected, reducing the dataset to 103,756 particles images. For 3D classification, the ACIII negative-stain map, low-pass filtered to 60 Å, was used as an initial reference. From nine 3D classes, the best three contained 52,386 particle images. Refinement of this subset, after polishing in Relion 2.1, and with a soft mask, produced a map at 3.87 Å nominal resolution. Local resolution was estimated using ResMap (Kucukelbir et al., 2014).

A 3D class with a weak density at the membrane level was recurrent in independent runs of 3D classification. Accordingly, particles from this class were re-extracted with a 300 x 300 pixels box and subjected to several rounds of 3D classification, with updated references containing the extra density. A subset of

9,267 particle images was identified and refined to a map of ACIII bound to an additional protein, with nominal resolution of 20 Å.

Seven subunits of ACIII were modelled *de novo* with Coot (Emsley et al., 2010). The atomic model was refined in Phenix (Adams et al., 2012) using real-space refinement and validated with Molprobity (Williams et al., 2018) and EMRinger (Barad et al., 2015). UCSF Chimera (Pettersen et al., 2004) was used for visualization of cryo-EM maps, docking of atomic models into the 20 Å map (ACIII from this work and *Thermus thermophilus caa$_3$* oxygen reductase – PDB 2YEV (Lyons et al., 2012)) and preparation of figures.

8.5. Peptide mass fingerprinting

Proteins present in the ACIII sample were analysed by peptide mass fingerprinting, performed as described previously (Buschmann et al., 2010) by Dr. Julian D. Langer from the Department of Molecular Membrane Biology, Max Planck Institute of Biophysics. A detailed description can be found in Sousa et al. (2018).

8.6. Isothermal calorimetry

Isothermal titration calorimetry (ITC) experiments were performed by Filipa Calisto from the group of Dr. Manuela Pereira, at ITQB, Universidade Nova de Lisboa. Briefly, ACIII in a 20 mM KPi pH 8, 10% glycerol and 0.05% DDM buffer was titrated with 2,3-Dimethyl-1,4-naphthoquinone (DMN) at 65 °C. A detailed description can be found in Sousa et al. (2018).

8.7. Sequence alignments

Filipa Calisto and Dr. Patrícia N. Refojo from the group of Dr. Manuela Pereira, at ITQB, Universidade Nova de Lisboa, performed sequence alignments in

CLUSTALW for all the ACIII subunits. More information can be found in Sousa et al. (2018).

9. Results

9.1. Single-particle negative-staining and cryo-EM analysis of ACIII

Samples of ACIII from *R. marinus* were initially analyzed by negative-staining with uranyl acetate. Grids were covered by particles of uniform size and showed no significant aggregation (Figure 31a). Two-dimensional reference-free classification of a small set of negatively-stained particles corroborated the homogeneity of the sample (Figure 31b). Since no suitable structure was available for use as a 3D reference in subsequent image processing routines, a first initial model was generated with EMAN2 by refining some of the high
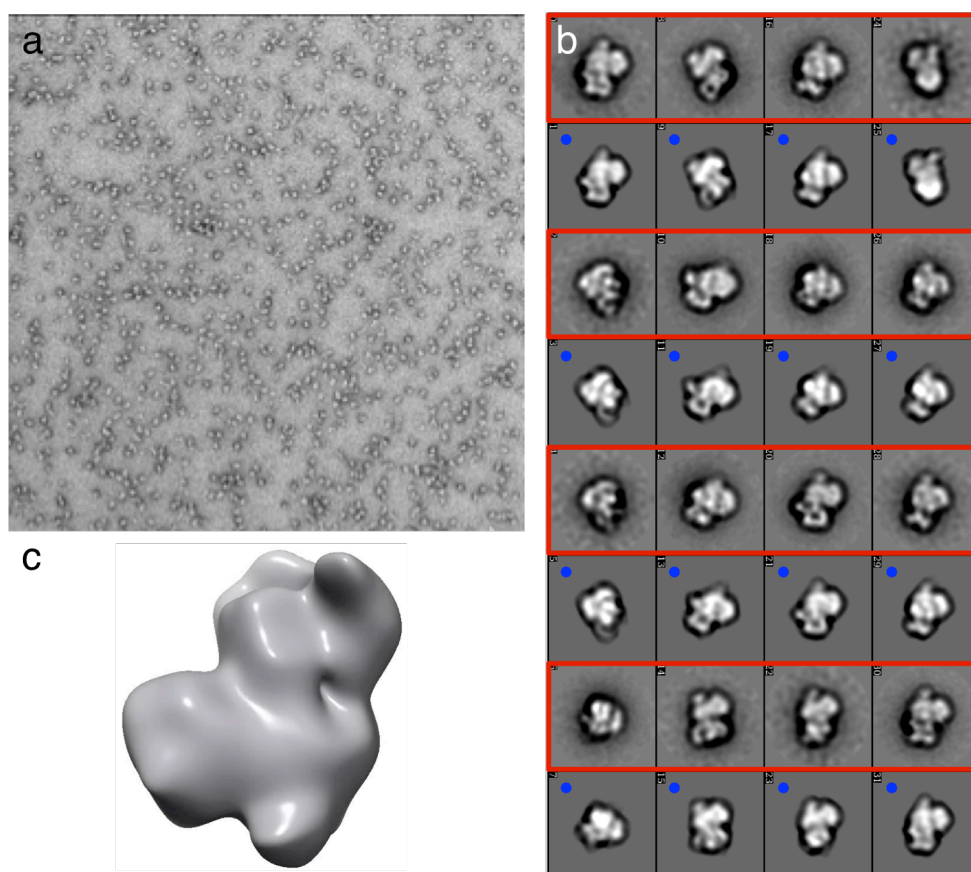
Figure 31. (a) Electron micrograph of ACIII stained with uranyl acetate, recorded with a Tecnai Spirit operating at 120 kV, at a magnification of 51,000x. **(b)** Negative-stain 2D class averages (highlighted in red) produced by reference-free 2D classification and used for generation of an initial model. Each 2D class is matched to a reprojection of the refined initial model (marked with a blue dot). **(c)** Initial model of ACIII generated with EMAN2.
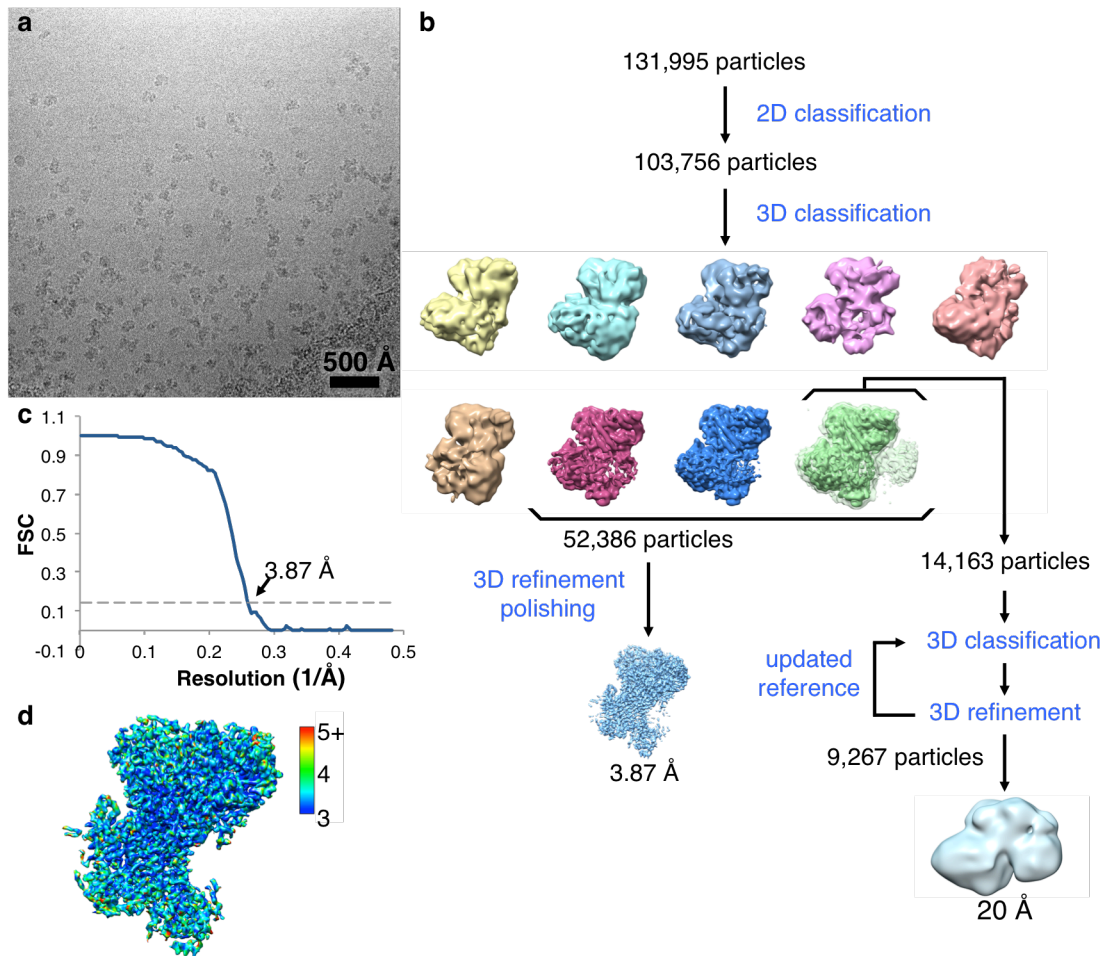
Figure 32. (a) Electron micrograph of ACIII recorded with a Gatan K2 Summit electron detector on a FEI Titan Krios with energy filter and operating at 300 kV. **(b)** Image processing workflow used for analysis of ACIII. Independent 3D classifications consistently produced a class with a weak density at the membrane level (green 3D class), visible at low contour level (light green). After re-extracting particles with a larger box size, a small population of particles with an additional density was identified by extensive 3D classification and refined to 20 Å resolution. Almost 40% of the total number of particles were refined into a 3.87 Å resolution map of ACIII. **(c)** Gold-standard FSC plot of the final ACIII map. Resolution estimated at FSC=0.143. **(d)** ACIII map colored by local resolution determined by ResMap.

quality 2D class averages against a random blob model (Figure 31b,c) (Ludtke et al., 1999; Tang et al., 2007).

Cryo-EM specimens prepared on C-flat multihole holey carbon grids exhibited a good distribution of ACIII in the ice in random orientations (Figure 32a). Nearly

2,500 movies were manually acquired on a FEI Titan Krios with a Gatan K2 Summit electron detector, for a total of ~132,000 particle images. Two distinct populations were identified by extensive 2D and 3D classification procedures, which were assigned to the ACIII complex and an ACIII-*caa*$_3$ supercomplex (Figure 32b), previously suggested to exist in *R. marinus* membranes (Refojo et al., 2010a). The ACIII set contained almost 40% of the initial number of particles and was refined to a 3.9 Å map, which was used to build an atomic model of the complex (Figure 32c,d, Figure 33). The second subset of particles, containing approximately 7% of the initial dataset, produced a map at 20 Å resolution with a large density associated to the transmembrane domain of ACIII. The extra density shape and size are consistent with the crystal structure of the *caa*$_3$ oxygen reductase from *Thermus thermophiles* (see 9.9. ACIII-*caa*$_3$ supercomplex).

9.2. Overall structure of ACIII

ACIII is an asymmetric complex whose transmembrane and soluble domains associate in an L-shape of ~110 Å by ~130 Å (Figure 33a). In total, eight polypeptide chains are present in the map, of which seven were modeled: subunits ActA, ActB, ActC, ActD, AtcE and ActF, encoded by the *act* gene cluster, and the newly identified ActH subunit. No density was observed for subunit ActG, even though this was detected by peptide mass fingerprinting (Figure 34). Notably, ActG should not be essential for catalysis since its gene is not present in all *act* gene clusters.

The orientation of the complex in the membrane can be inferred from the existence of *c*-type cytochromes in the large peripheral domain that must be, therefore, located in the periplasm. In addition to the six *c*-type hemes harbored by ActA and ActE, the periplasmic domain accommodates four iron-sulfur clusters within ActB (Figure 35). No prosthetic groups are present in the membrane or cytoplasmic domains.
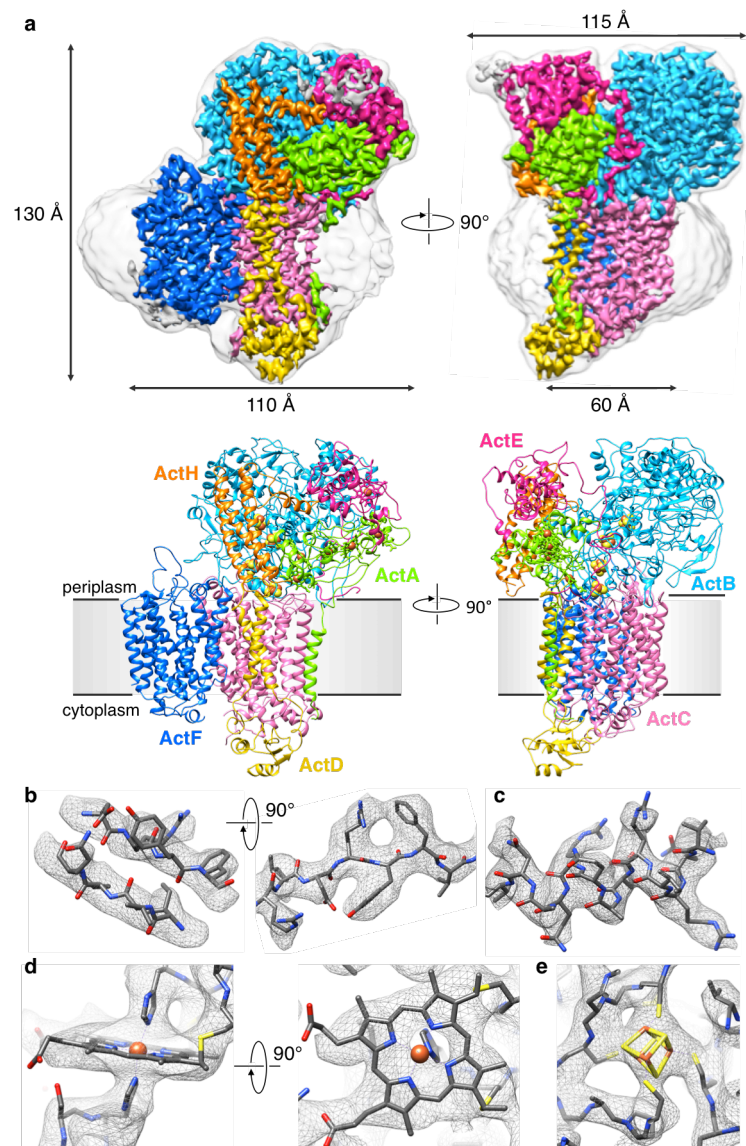
Figure 33. (a) ACIII cryo-EM density map (top) and model (bottom). The DDM micelle is visible in a map low-pass filtered to 10 Å (transparent light grey). Above ActE, the density of the eight subunit of the complex is visible in grey. ActA (green), ActB (cyan), ActC (pink), ActD (yellow), ActE (magenta), ActF (blue) and ActH (orange). Heme irons are shown as orange spheres and the porphyrin as green/magenta sticks. Iron-sulfur clusters are depicted as orange and yellow spheres. **(b)** Cryo-EM densisty of a β-sheet, with well resolved strands and good side chain densities. **(c)** Cryo-EM density of an α-helix, with clear helical pitch and good side chain densities. **(d)** Cryo-EM density of heme II and its axial histidines. **(e)** Cryo-EM density of cluster FeS2 and coordinating cysteines.
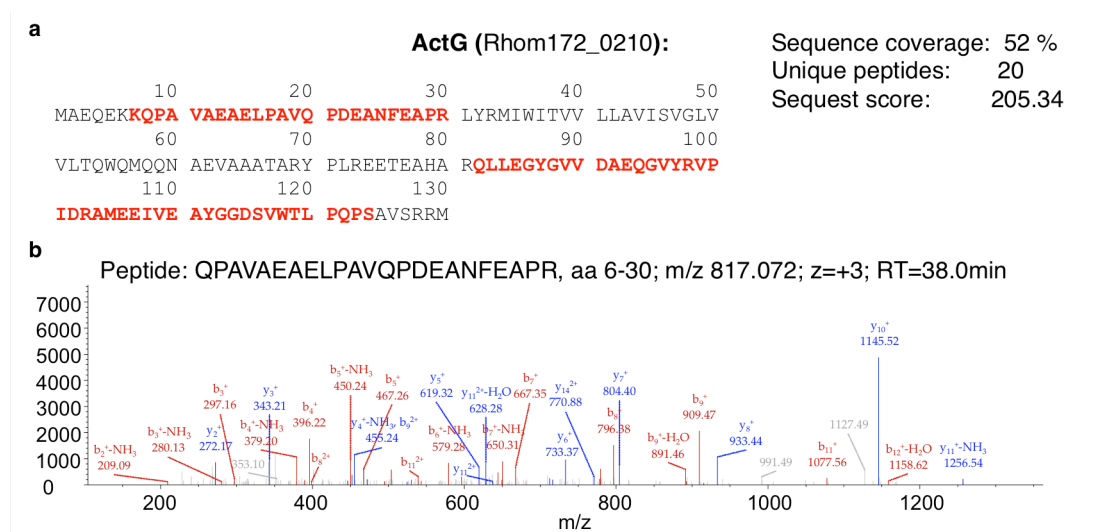
Figure 34. (a) ActG (Rhom172_0210, Uniprot identifier: G2SEG6) identification using LC-MS/MS (sequence coverage: 52%, matched peptides highlighted in red). **(b)** Annotated MS/MS spectrum for peptide QPAVAEAELPAVQPDEANFEAPR, corresponding to amino acid residues 6-30 of ActG. Peptide mass fingerprinting was performed by Dr. Julian D. Langer, Max Planck Institute of Biophysics.
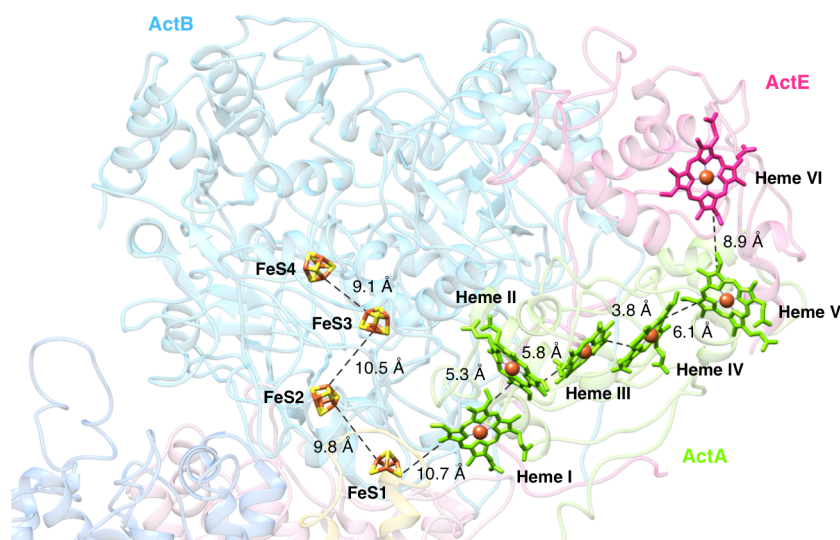
Figure 35. Prosthetic groups in ACIII form an ~35 Å chain of four iron-sulfur clusters and an ~60 Å heme wire with six *c*-type hemes, which diverge from FeS1. Dashed lines indicate edge-to-edge distances. ActA, ActB and ActE are shown in green, cyan and magenta, respectively. ActH was removed for clarity.

The complex has 23 TMH. The major membrane domain is composed of the two homologous subunits ActC and ActF, with 10 TMH each, and the smaller subunit ActD, with two TMH. The last TMH occupies a peripheral position and consists of the N-terminal residues of ActA. The N- and C-termini of ActC, ActD and ActF form the small cytoplasmic domain.

Two additional densities are visible in the periplasmic domain of ACIII that could not be assigned to any of the subunits encoded by the *act* gene cluster. The larger of the two was identified by peptide mass fingerprinting as the protein Rmar_1979, here renamed ActH. The second, smaller density is located above ActE, but could not be identified due to the lower resolution in this area of the map. The unidentified density is largely exposed to the solvent and is thus unlikely to be ActG, which is predicted to be an integral membrane subunit with one TMH.

9.3. ActA

ActA is a pentaheme cytochrome *c* with an N-terminal membrane anchor of a single TMH (Figure 36). The TMH density is weak when compared to the ones in the major membrane domain, most likely due to high flexibility. This assumption is supported by the fact that the TMH is isolated within the membrane, interacting only with loops of ActC and ActD at the membrane boundaries. The soluble domain is organized in two pseudo-symmetric subdomains, from residues 45 to 89 and residues 121 to 165, consistent with early gene duplication and fusion.

The five hemes of ActA form a linear wire of ~45 Å. Heme I is coordinated by a histidine and a methionine at the interface of ActA with ActB and is partially occluded by the N-terminus of ActE. The remaining hemes are located in the pseudo-two-fold symmetric subdomains and have two histidines for axial ligands. The porphyrin rings of hemes II-III and IV-V form two "di-heme elbow motifs" (Figure 36), with a ~6 Å edge-to-edge distance, while hemes III and IV relative position matches the structure of the split-Soret cytochrome from
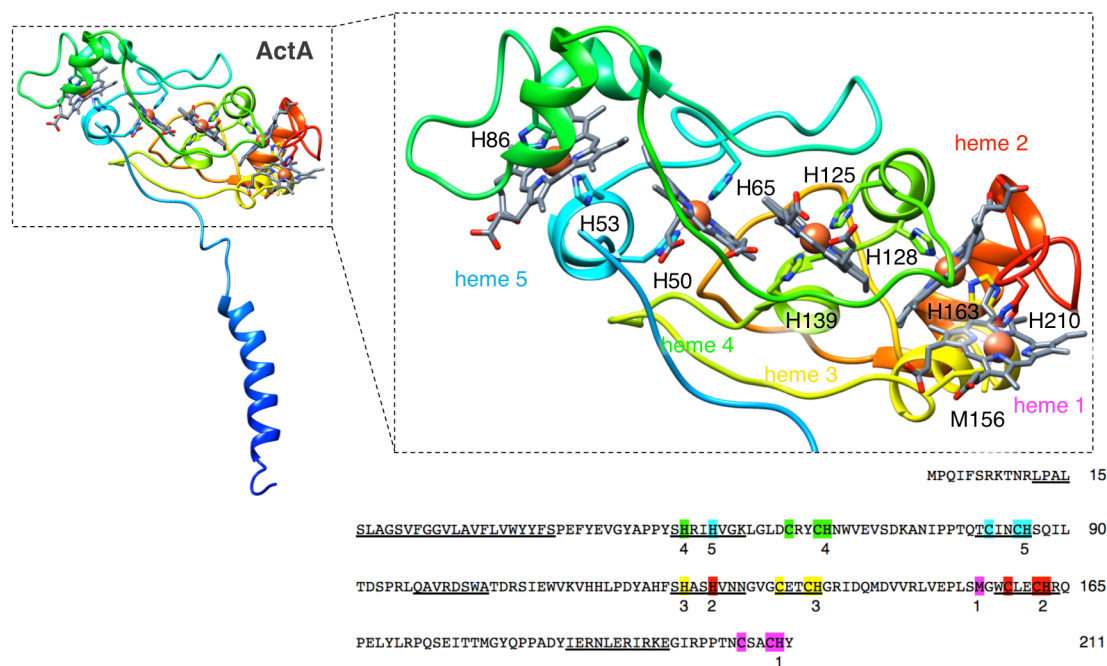
Figure 36. ActA structure with one TMH and five hemes, each coordinated by a CxxCH motif and a distal residue. The coordinating residues of each heme are highlighted in the sequence in the same color used in the model labels. The domains binding hemes 3-2 and 4-5 show a local two-fold pseudo-symmetry, most likely consequence of gene duplication. The model is colored in a rainbow, from blue to red.

Desulfovibrio desulfuricans ATC27774 (Matias et al., 1997). The parallel arrangement of the latter, with an edge-to-edge distance of less than 4 Å, is responsible for the split Soret effect in the UV-visible absorbance spectrum of ACIII (Pereira et al., 1999a).

9.4. ActE

ActE is a monoheme cytochrome *c*. Its heme (heme VI) adds to the heme wire of ActA, at ~9 Å from heme V (Figure 35). Similarly to heme I, heme VI is coordinated by a histidine and a methionine and is not part of any typical heme motif. The N-terminus of ActE extends from the membrane to the top of ActA and was traced starting at residue Ile28[E] at the membrane surface (Figure 37). Density for the first 27 amino acid residues is not visible. Nevertheless, the
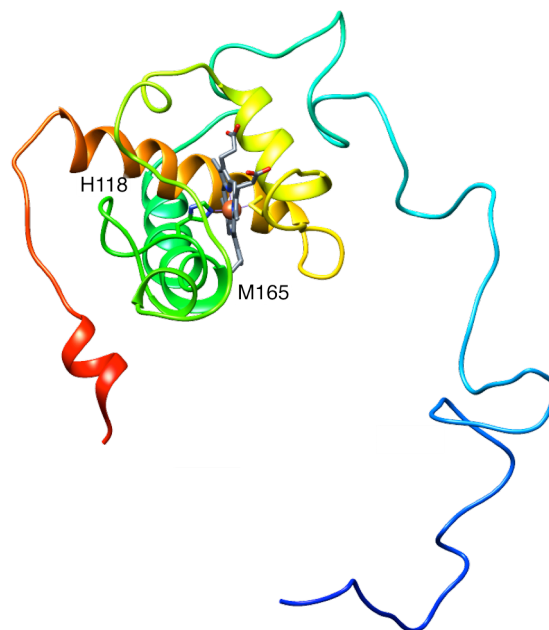
Figure 37. ActE structure rainbow-colored from blue (N-terminus) to red (C-terminus), with a long N-terminus loop and a *c*-type heme coordinated by His188 and Met165.

structure is in agreement with the prediction of ActE being a lipoprotein with a lipid-modified cysteine (Cys24^E) (Refojo et al., 2017).

9.5. ActB

ActB is the largest subunit in ACIII and interacts with all other subunits. Our structure shows that the first 74 amino acid residues, including the twin-arginine translocase (Tat) signal, are cleaved during translocation of the chain to the periplasm, as suggested by previous N-terminal sequencing results (Pereira et al., 2007).

Also in agreement with early studies (Pereira et al., 2007), the N-terminal domain B1, which includes residues 75 to 735, does not harbor any prosthetic groups, despite its homology to molybdopterin-containing proteins. Domain B2, from residues 736 to 1039, accommodates an iron-sulfur cluster electron transfer wire of ~35 Å (Figure 35) (Pereira et al., 2007; Refojo et al., 2010b).

The wire begins near the membrane surface with a [3Fe-4S] cluster (FeS1) and extends with three [4Fe-4S] clusters (FeS2-4) to 7 Å from the protein surface. FeS1 is ~11 Å away from heme I in ActA, and is the origin of two divergent electron transfer wires in ACIII.

9.6. ActC and ActF

The core membrane subunits ActC and ActF share the same fold and are related by a ~180° rotation through the normal to the membrane plane (Figure 38). Each of them has 10 TMH arranged in two four-helix bundles and one helix dimer. The four-helix bundles, containing TMHs 2 to 5 and 6 to 9, form parallel, face-to-face structural repeats identical to PsrC from *Thermus thermophilus*
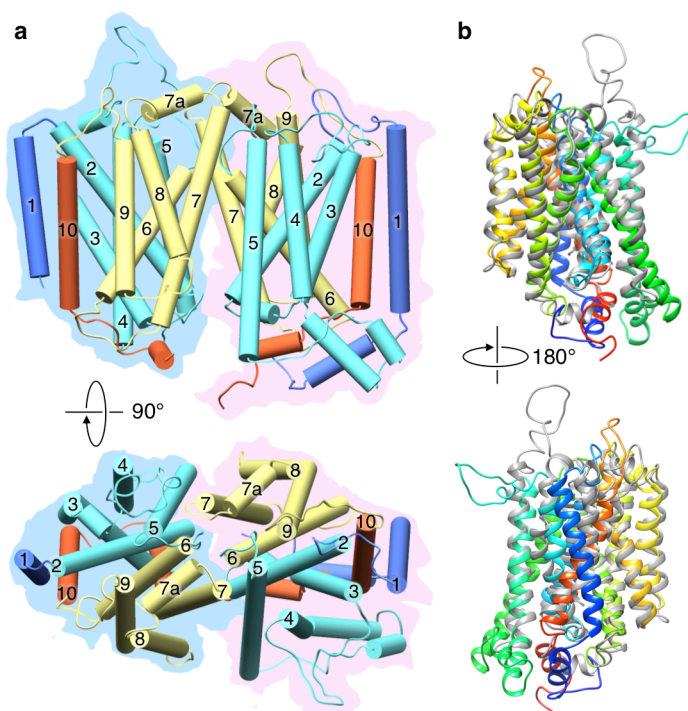
Figure 38. (a) ActC (pink silhouette) and ActF (blue silhouette) seen from the membrane (top) and from the periplasm (bottom). The two four-helix bundles are shown in cyan (TMHs 2-5) and yellow (TMHs 6-9) and the N- and C-terminal helices are colored in blue and red, respectively. **(b)** Superposition of ActC and ActF shows that the two subunits share the same fold. ActC is drawn with a rainbow palette from blue to red and ActF is shown in grey.
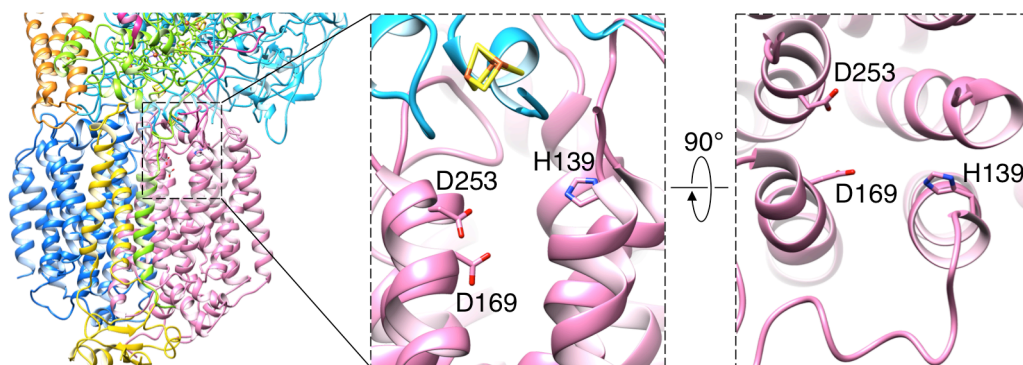
Figure 39. Putative quinol-binding site in ActC, with zoomed views of conserved residues proposed to be involved in quinol coordination, seen from the membrane (center) and from the periplasm (right). Subunits are colored as in Figure 33.

(Jormakka et al., 2008). The additional N- and C-terminal helices (TMHs 1 and 10) cross each other at the periphery of the ActC-ActF dimer, at an angle of ~45°. The dimerization interface is established by TMHs 2, 5, 6 and 7 and possibly by lipid-protein interactions, as several elongated densities are visible in the map between the two subunits.

Analysis of the structure suggests that, similarly to the homologous PsrC
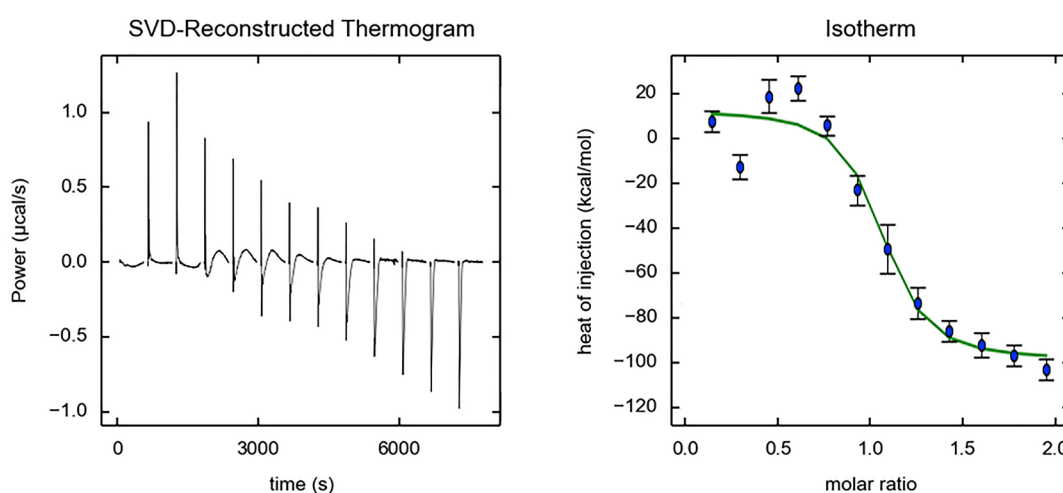
Figure 40. ITC thermogram obtained by titrating 190 μM DMN to 19 μM ACIII at 65 °C (left) and data after processing with NITPIC, fitted with a 1:1 binding model (right), with a binding constant (log K_a) of 6.5 ± 0.14. ITC experiments were performed by Filipa Calisto at ITQB.

(Jormakka et al., 2008), ActC harbors a quinol-binding site in its first four-helix bundle, near the membrane-periplasm boundary (Figure 39). The largely hydrophobic pocket is accessible from the membrane through a narrow channel delimited by TMHs 3 and 4 and the loop connecting them (L3-4) and contains three highly conserved charged or polar residues: His139[C], Asp169[C] and Asp253[C] (Appendix A). The presence of two conserved aspartates agrees with the need of acidic residues for deprotonation of the quinol (Abramson et al., 2000; Crofts et al., 1999; Iwata et al., 1998), while an essential histidine residue is known to participate in quinol coordination within many quinone-binding complexes (Fisher and Rich, 2000). The putative binding site is only 10-12 Å from cluster FeS1 in ActB and more than 20 Å away of heme I in ActA, which suggests the former to be the primary electron acceptor from the quinol. ActF lacks the residues defining the quinol-binding site as in ActC, as well as the binding pocket and entry channel since the structure of L3-4 deviates substantially from the conserved fold of ActC and PsrC. This is in agreement with the peripheral location of ActF in the structure, which positions it far from any cofactor in the complex. The presence of a single quinol-binding site in ACIII was corroborated by ITC experiments (Figure 40).

In both ActC and ActF, two putative half-channels lined by conserved residues (Appendix A and B) are observed: a cytoplasmic half-channel within the first four-helix bundle (TMHs 2 to 5) and a periplasmic half-channel in the second four-helix bundle (TMHs 6 to 9) (Figure 41). These pathways are similar to the ones proposed for PsrC and may contribute to electrogenic pumping of protons by ACIII.

9.7. ActD

ActD has two TMHs forming a helix dimer near the first four-helix bundle of ActC. Its N- and C-terminus form an antiparallel, four-stranded β-sheet that accounts for most of the small cytoplasmic domain of ACIII (Figure 42a). Within its second TMH, ActD has a highly conserved glutamate (Glu122[D]) (Appendix C), which is only ~8 Å from Asp169[C] at the quinol-binding site (Figure 42b). The position of
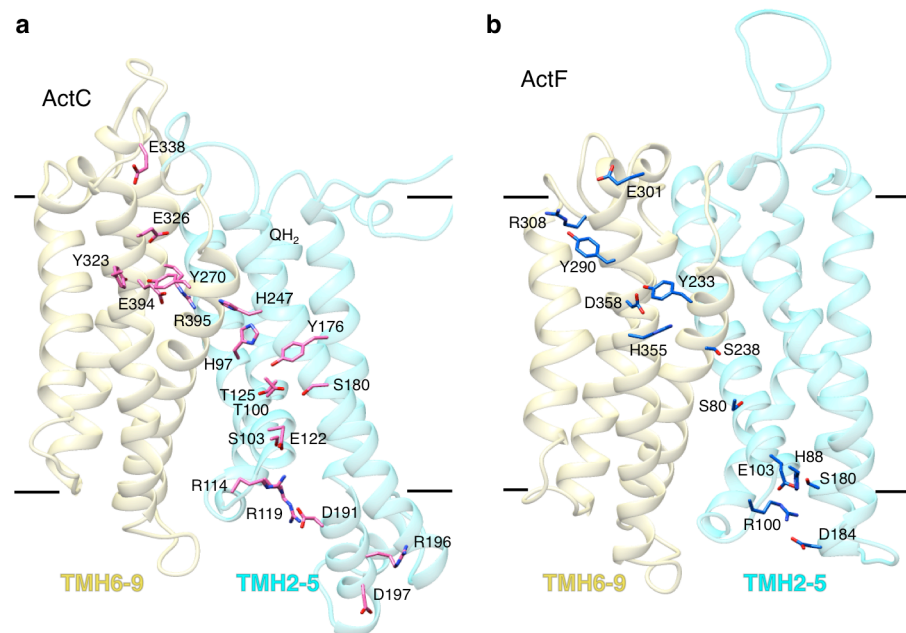
Figure 41. (a) ActC proton-conducting half-channels. The cytoplasmic half-channel (TMHs 2-5) is formed by residues Asp197, Arg196, Asp191, Arg119, Glu450, Arg114, Glu112, Ser103, Thr100, Thr125, Ser180, Tyr176, His97 and His247, while the periplasmic half-channel (TMHs 6-9) consists of residues Arg395, Glu394, Tyr270, Tyr323, Glu326 and Glu338. The approximate position of the quinol-binding site is indicated (QH$_2$). **(b)** ActF cytoplasmatic (TMHs 2-5) and periplasmatic (TMHs 6-9) proton-conducting half-channels include residues Asp184, Arg100, Ser180, Glu103, His88, Ser80, Ser238, His355, Asp358, Tyr233, Tyr290, Arg308 and Glu301. The four-helix bundles are shown in cyan (TMHs 2-5) and yellow (TMHs 6-9).

these residues may allow protonation or conformational changes of Asp169^C, linked to quinol oxidation, to be sensed by Glu122^D. At a short distance from Glu122^D we find also the conserved residues Ser245^C and Tyr284^F, which align with the central plane of the membrane where the putative half-channels in ActC and ActF meet.

9.8. ActH

After modeling subunits ActA to ActF, a bundle of three long helices at the periplasmic domain, with density inconsistent with the ActG amino acid sequence, remained unassigned. Combinatorial proteolytic digests, combined
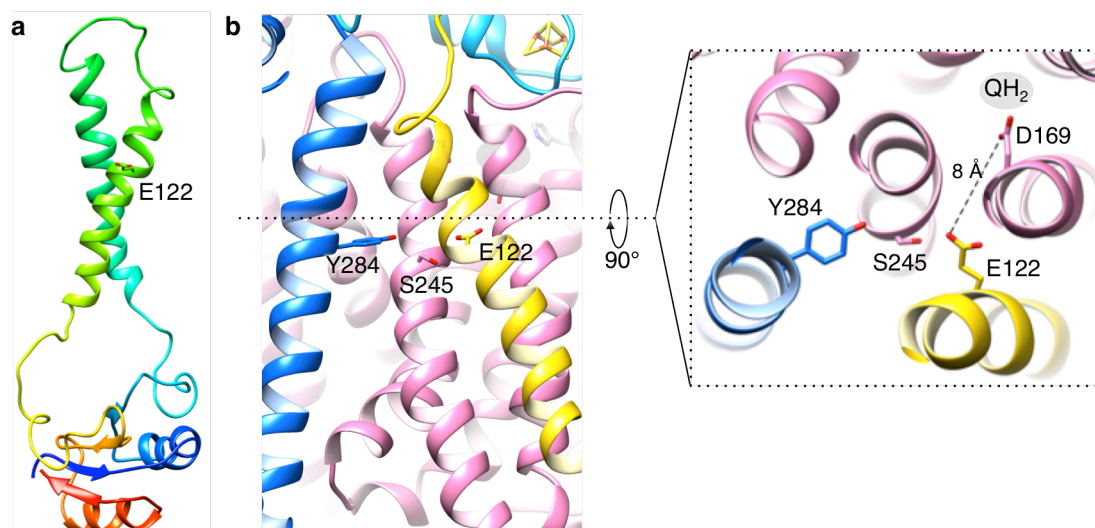
Figure 42. (a) ActD as seen from ActC. The conserved Glu122 in the middle of TMH 2 is shown. **(b)** Inter-subunit cross-talk at the interface between ActC, ActF and ActD, with the highly conserved Glu122^D, Ser245^C and Tyr284^F aligned at the central plane of the membrane and each 3-5 Å away from their closest neighbor. Glu122^D is ~8 Å from Asp169^C, part of the putative quinol-binding site. Subunits are colored as in Figure 33.

with liquid chromatography-coupled tandem mass spectrometry were used to identify the protein (Figure 43a,b). A total of 152 proteins from the *R. marinus* database were found in the ACIII sample, of which 62 yielded more than two high-scoring, unique peptides. Secondary structure predictions were further used to screen for proteins with predicted three long helices (Figure 43c). This analysis pinpointed hypothetical protein Rmar_1979, with 26 unique peptides and 47 % sequence coverage, with a sequence that agreed well with the side chain densities in the map (Figure 43d,e). Rmar_1979, or "ActH", is specific to *R. marinus* and its close relatives and might enhance ACIII stability by extending the contact surfaces of ActA, ActB and ActE.

9.9. ACIII-*caa₃* supercomplex

The 20 Å map with a shape suggestive of an ACIII-*caa₃* supercomplex accommodates well our ACIII model together with the structure of the *caa₃*
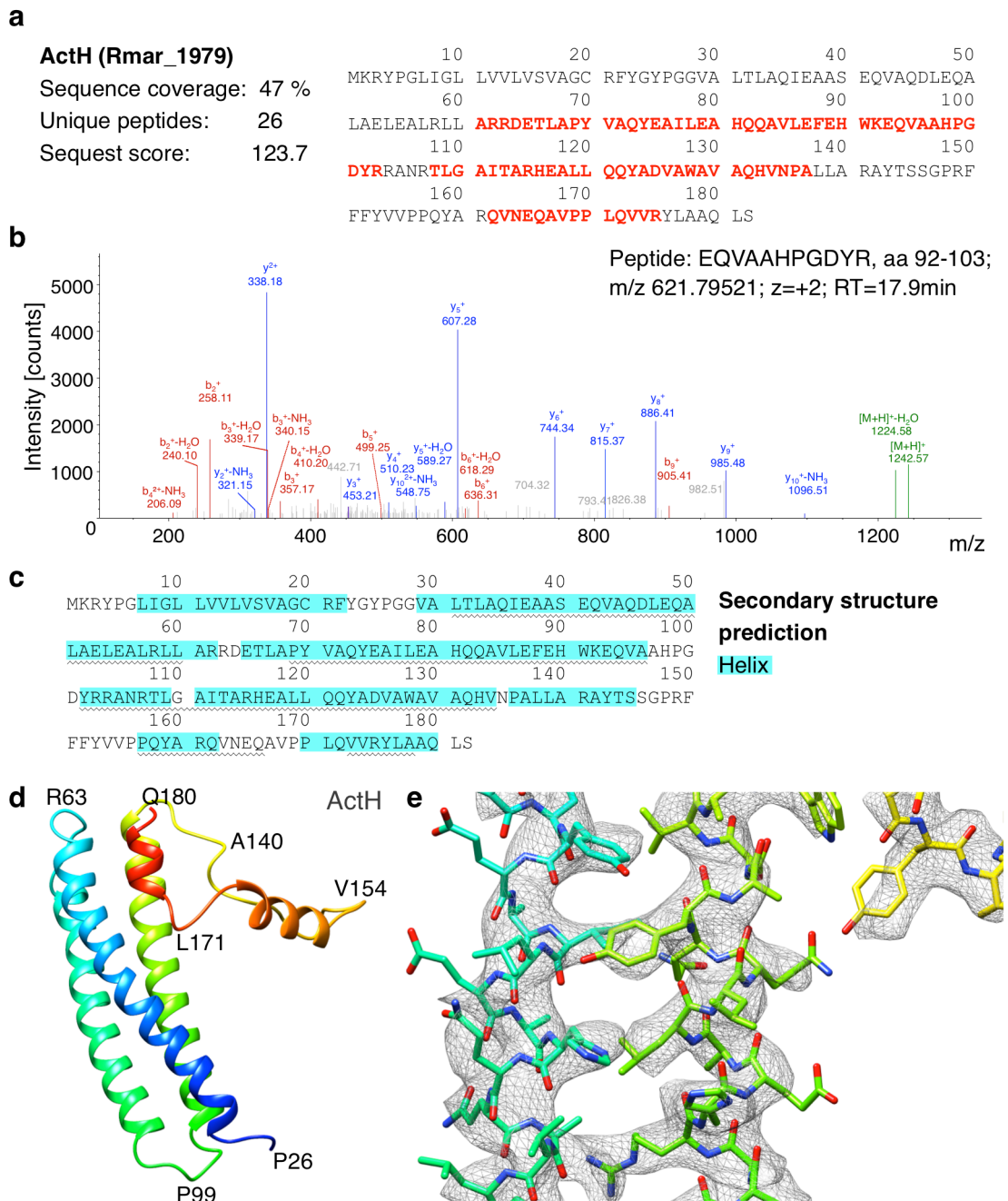
Figure 43. Identification of ActH as an ACIII subunit. **(a)** ActH (Rmar_1979, Uniprot identifier: D0MKF0) identification using LC-MS/MS (sequence coverage: 47%, matched peptides highlighted in red). **(b)** Annotated MS/MS spectrum for peptide EQVAAHPGDYR, corresponding to amino acid residues 92-103 of ActH. **(c)** Secondary structure predicted by PredictProtein with helices indicated in cyan. Helices modeled into the map are indicated by a wavy underline. **(d)** ActH model in rainbow colors from blue (N-terminus) to red (C-terminus). **(e)** Cryo-EM density map of ActH with model. Peptide mass fingerprinting was performed by Dr. Julian D. Langer, Max Planck Institute of Biophysics. Identification and modeling of ActH was performed by Dr. Janet Vonck, Max Planck Institute of Biophysics.

oxygen reductase from *Thermus thermophilus* (PDB 2YEV (Lyons et al., 2012)) (Figure 44). The docking of these models in the cryo-EM map places the membrane subunit I/III from the *caa*$_3$ oxygen reductase next to ActC and under ActA, and the soluble domain of subunit IIc opposite to ActA and ActE.
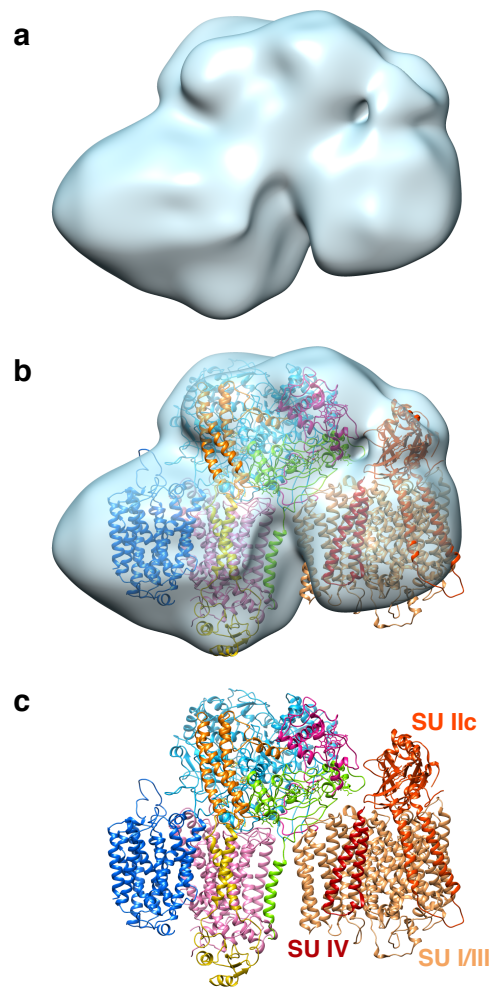
Figure 44. (a) Cryo-EM map of ACIII-*caa*$_3$ supercomplex at 20 Å resolution. **(b)** Fit of ACIII model (this work) and *Thermus thermophilus caa*$_3$ oxygen reductase to the cryo-EM map. **(c)** Fitted models of ACIII and *caa*$_3$ oxygen reductase.

...

10. Discussion

10.1. ACIII and the canonical complex III

ACIII is a quinol:cytochrome *c*/HiPIP oxidoreductase that replaces (or complements) the activity of the cytochrome bc_1 complex (complex III) in many bacteria. The structure of ACIII reported here (Figure 33) shows how these two complexes differ greatly in architecture and, consequently, in their catalytic mechanism. First, ACIII appears to exist in a monomeric state, while complex III is an obligatory dimer. More relevant differences concern the number of quinol-binding sites (Figure 39 and Figure 40) and the distribution of cofactors within the structure (Figure 35) that make the operation of a Q-cycle by ACIII impossible (see more on Q-cycle in 2.4. Complex III). Specifically, ACIII has a single quinol-binding site, instead of two complementing redox sites as the complex III protomers (Q_o and Q_i), and does not harbor cofactors in its membrane domain, in opposition to complex III that has two hemes within the cytochrome *b* subunit in the membrane.

Interestingly, the structure of ACIII approximates more the canonical complex I (Figure 15). The two complexes share an L-shape architecture, where the soluble arm conceals an electron transfer wire and the membrane arm comprises homologous subunits with putative proton pathways. These structural similarities may precede a functional parallelism between ACIII and complex I (see 10.3. Quinol oxidation and energy transduction).

10.2. Electron transfer wires

The prosthetic groups in ACIII form two distinct electron transfer wires: an iron-sulfur cluster wire and a heme wire (Figure 35). The two chains bifurcate at FeS1. The reduction potential of this [3Fe-4S] cluster was previously shown to be +140 mV by EPR monitored redox tritation (Pereira et al., 1999a) and its location in the structure is ideal to receive electrons from the quinol bound in ActC.

It is unclear if and how clusters FeS2, FeS3 and FeS4 might contribute to electron flow within ACIII, since in EPR spectroscopy experiments no signals were detected for [4Fe-4S] centers (Pereira et al., 1999a). Nevertheless, the structure shows that FeS4, at the end of the wire, is near the protein surface and so this might donate or receive electrons from an external electron carrier. The cysteines that coordinate the iron-sulfur clusters are strictly conserved. The preservation of this second wire throughout evolution implies that this is necessary to the enzyme and further studies should be performed to understand its role.

The second wire with hemes from both ActA and ActE is approximately 60 Å long. These hemes have reduction potentials that range from –45 mV to +230 mV at neutral pH (Crofts et al., 1999; Pereira et al., 1999a) and are known to be reduced upon quinol oxidation (Refojo et al., 2010b).

Together, the biochemical and structural data suggest that FeS1 is the primary electron acceptor in ACIII, oxidizing quinol to quinone. Subsequently, FeS1 donates the electrons to the heme wire for direct reduction of the electron carriers, cytochrome c and HiPIP, or the caa_3 oxygen reductase (see 10.5. Electron transfer in the ACIII-caa_3 supercomplex).

10.3. Quinol oxidation and energy transduction

In the oxidoreduction reaction catalyzed by ACIII, two electrons are transferred from menaquinol, with a reduction potential of –70 mV, to an electron acceptor with a reduction potential of +250 mV (Pereira et al., 1999a; Srinivasan et al., 2005; Stelter et al., 2008). The energy released is sufficient to transfer up to four protons into the periplasm. Accordingly, the presence of two putative proton pathways in ACIII (Figure 41) suggests that the complex contributes to the transmembrane electrochemical potential as a redox-driven proton pump, similarly to complex I. The residues in the channels should allow proton translocation through a hydrogen bond network, according to a Grotthuss mechanism (Cukierman, 2006; de Grotthuss, 2006).

The coupling of the redox reaction to the transport of protons across the membrane requires the propagation of conformational changes from the quinol pocket in ActC to the proton channels in the same subunit and in ActF. We propose that ActD mediates this communication through one key residue. Glu122^D is located in the inner TMH of ActD, near Asp169^C from the quinol-binding site and the conserved residues Ser245^C and Tyr284^F positioned at the plane in the middle of the membrane at which the cytoplasmic and periplasmic half-channels meet (Figure 42). The short distance from Glu122^D to the binding pocket suggests that it may act as a sensor for conformational or protonation changes that occur upon quinol oxidation. The cross talk between residues Glu122^D, Ser245^C and Tyr284^F may then induce conformational changes at the channel gate in both ActC and ActF, triggering its opening and proton translocation (Figure 45).
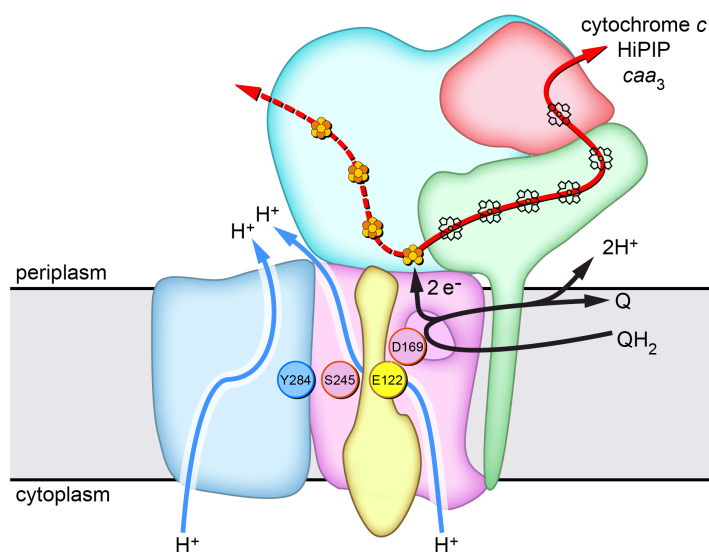
Figure 45. Proposed mechanism for ACIII operation as a redox-driven proton pump. Upon quinol oxidation (black arrows), electrons are transferred to FeS1 and than through the electron wires (red arrows); electrons conducted through the heme wire reduce cytochrome *c*, HiPIP or the *caa*$_3$ oxygen reductase. Simultaneously, a protonation or conformational change of Asp169^C at the quinol-binding site is propagated through the conserved neighboring residues Glu122^D, Ser245^C and Tyr284^F (colored circles). The conformational changes of these residues, located in the plane at the end of the putative proton half-channels, allow further conformational changes in ActC and ActF for proton translocation across the membrane (blue arrows). ActH is omitted for clarity.

10.4. ACIII from Flavobacterium johnsoniae

In a study contemporaneous to ours, the structure of ACIII from *Flavobacterium johnsoniae*, in a supercomplex with the aa_3 oxygen reductase, was solved by single-particle analysis at 3.4 Å resolution (PDB 6BTM) (Sun et al., 2018). Overall, the ACIII structures from *F. johnsoniae* and *R. marinus* are closely related, differing mainly in the supernumerary subunits that associate to the core complex and in the N-terminus of ActA.

The map of ACIII from *F. johnsoniae* shows density for subunits ActA to ActF and two unidentified transmembrane peptides associated to ActC, named by the authors ActX and ActY. No density corresponding to the *R. marinus* ActH subunit or the soluble subunit on top of ActE is present. In addition, the supernumerary subunit ActG is not encoded in the *act* gene cluster from *F. johnsoniae* and, accordingly, it is not found in the complex.

The structure shows that ActE has a triacylated cysteine at its N-terminus, as previously suggested for the ActE subunit in *R. marinus* (Refojo et al., 2017). Also ActB has a N-terminal lipid anchor. Moreover, as in *R. marinus*, several lipid molecules are observed at the interface between ActC and ActF.

The sequence of the ActA subunit of *F. johnsoniae* suggests the presence of an additional TMH and of a monoheme domain at its N-terminus, not present in *R. marinus*. However, no density is observed for this domain in the cryo-EM map, possibly due to a high degree of flexibility (see 10.5. Electron transfer in the ACIII-caa_3 supercomplex).

Only two iron-sulfur clusters are present in the structure of ACIII of *F. johnsoniae* solved by Sun and co-workers (Sun et al., 2018), namely FeS1 and FeS2. Nonetheless, the cysteine ligands for FeS3 and FeS4 are still found in the ActB subunit. Therefore, the two additional iron-sulfur clusters, present in the ACIII from *R. marinus*, were most likely lost during purification of the complex from *F. johnsoniae* due to oxidation.

10.5. Electron transfer in the ACIII-caa$_3$ supercomplex

ACIII was previously proposed to form a stable supercomplex with the *caa$_3$* oxygen reductase, in *R. marinus*, which is partially preserved after solubilization with DDM (Refojo et al., 2010a). The structural data obtained during this work (Figure 44) corroborates the existence of such an assembly and provides important insights into the electron flow. Within the supercomplex, the heme wire of ACIII converges to the cytochrome *c* domain of subunit IIc, the electron entering point of the terminal oxidase. Interestingly, it has been shown that ActE, with the last heme in the wire, is a direct electron donor to the *caa$_3$* oxygen reductase (Refojo et al., 2017). Our structure shows that the orientation of ActE and subunit IIc is favorable for the direct reduction of the *caa$_3$* oxygen reductase by ACIII (Figure 44c), without intervention of electron carriers.

Similar supercomplexes of ACIII and an oxygen reductase were believed to exist in other bacteria, since frequently a gene cluster encoding the latter is located downstream of the *act* gene cluster (Refojo et al., 2010b, 2010a; Yanyushin et al., 2005). Accordingly, a cryo-EM study of ACIII from *F. johnsoniae* (Sun et al., 2018) shows that the complex co-purifies with the *aa$_3$* oxygen reductase in the form of a supercomplex. The *aa$_3$* oxygen reductase differs from the *caa$_3$* oxygen reductase by lacking the cytochrome *c* domain in subunit IIc. The authors also report that this supercomplex in the presence of menaquinol catalyzes reduction of oxygen to water, without addition of exogenous cytochrome *c*. This agrees with our proposal that the assembly of ACIII into supercomplexes serves a functional role, where the efficiency of electron transfer is improved by bypassing electron carriers.

While the overall design of the ACIII complex is conserved between *F. johnsoniae* and *R. marinus*, species-specific variations seem to relate with the architecture of the supercomplex. In *F. johnsoniae*, the *aa$_3$* oxygen reductase faces subunits ActC, ActD and ActF, contrasting with the relative positions of ACIII and the *caa$_3$* oxygen reductase in *R. marinus* (Figure 44). In this alternative arrangement, ActE is not close enough to the oxygen reductase for direct electron transfer. Instead, an additional monoheme domain present at the ActA N-terminus is proposed to

mediate the electron transfer by moving between ActE and the aa_3 oxygen reductase (Sun et al., 2018). Interestingly, the N-terminal monoheme domain of ActA in *F. johnsoniae* has significant sequence homology with the heme *c* domain of subunit IIc from the caa_3 oxygen reductase from *Thermus thermophilus*, absent in the aa_3 oxygen reductase. The comparison between these two ACIII supercomplexes illustrates how different strategies may be employed for direct electron from ACIII to different terminal oxidases.

11. Conclusions

The work presented here provided a structural understanding of ACIII and offers pioneering insights into the catalytic mechanism of this quinol:cytochrome *c*/HiPIP oxidoreductase. The postulated mechanism introduces potential key elements for quinol oxidation, proton translocation and energetic coupling, contributing with testable hypothesis for upcoming studies.

Our results further stress the imperative role of supercomplexes within respiratory chains. While the purpose of these large macromolecular assemblies is still highly debated (see Chapter I), the ACIII-oxygen reductase supercomplex appears to serve a clear functional role by circumventing the need for electron carriers.

In the future, biochemical studies should be performed to verify the ability of ACIII to pump protons across the membrane and the relevance of the residues identified here. A higher resolution map of the ACIII-*caa*$_3$ supercomplex should also be pursued, for a precise evaluation of the assembly interfaces and of the distance between the hemes of ActE and subunit IIc. The isolation of the ACIII-*caa*$_3$ supercomplex will most likely benefit from the use of milder detergents or SMA (styrene-maleic acid) co-polymers, rather than DDM used in this study.

CHAPTER III

12. Introduction

12.1. Transport across biological membranes

The lipid bilayer that delimits the cell and its organelles constitutes a barrier to the free diffusion of solutes. This segregation is essential to life, as is well illustrated by its role in the maintenance of the electrochemical potential generated by the respiratory electron transfer chain. In addition, the controlled and regulated flux of ions, nutrients and other molecules across these membranes is required for a proper performance of the cell. Accordingly, many membrane proteins are responsible for mediating the import or export of different substrates in diverse biological processes.

Transport can be performed down the electrochemical gradient (passive transport or facilitated diffusion) or against it with expense of energy (active transport). The membrane proteins that catalyze such transport belong to two main groups: channels and transporters (Figure 46). Typically, channels have a higher conductance than transporters, but several exceptions to this rule are known and the distinction between them can be difficult. The first, also known as "pores", allow access to both sides of the membrane simultaneously, may have a
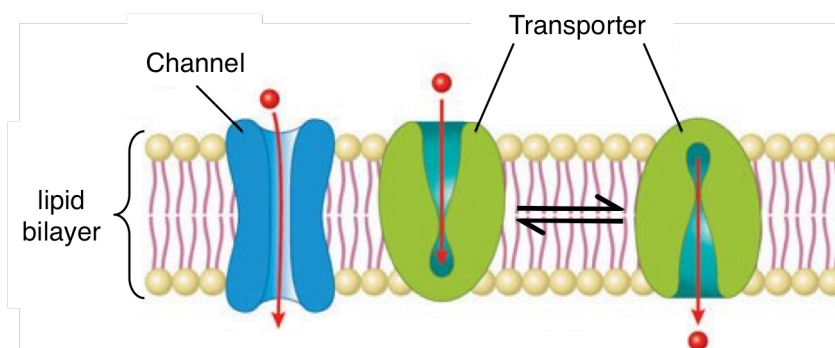
Figure 46. Schematic representation of a channel (blue) and a transporter (green). Adapted with permission from https://www.profacgen.com/preclinical/transporter-screening-service.htm. Copyright © 2010-2019 Profacgen.

regulatory gate or be constitutively opened, and mediate passive diffusion of the substrate down its electrochemical gradient. The latter have two gates that during the transport cycle regulate the access to either side of the membrane, through pronounced conformational changes linked to substrate binding and release. Transporters can actively transport substrates, by coupling with a chemical energy source such as ATP (primary active transporters) or with dissipation of pre-existing ion gradients (secondary active transporters), or may simply facilitate the diffusion of a specific molecule down its concentration gradient (facilitators).

12.2. Secondary active transporters

Secondary active transporters drive the translocation of their substrate by coupling it to the diffusion (down their concentration gradient) of one or more co-substrates. The most common co-substrates are ions, such as Na^+ and H^+. Substrate and co-substrate can be translocated in the same or opposite directions, by transporters named symporters and antiporters (or exchangers), respectively. These transporters are fully reversible, with the direction of flux being determined by the combined electrochemical potential of substrate and co-substrate(s).

From the structural analysis performed to date, three common folds have been identified for this type of membrane proteins: the MFS (major facilitator superfamily) fold, the LeuT fold and the NhaA fold (Figure 47). Some features are recurrent in these folds, namely the pseudo-symmetry exhibited by the transmembrane core, resultant from the presence of two inverted structural repeats (Shi, 2013), and the existence of discontinuous helices, crucial for transport as the unwound region frequently plays a role in ion and substrate coordination (Screpanti and Hunte, 2007).

The general mechanism of secondary-active transport is described by the alternating-access model, which postulates that the transporter must switch between at least three different conformational states: a inward-facing and a
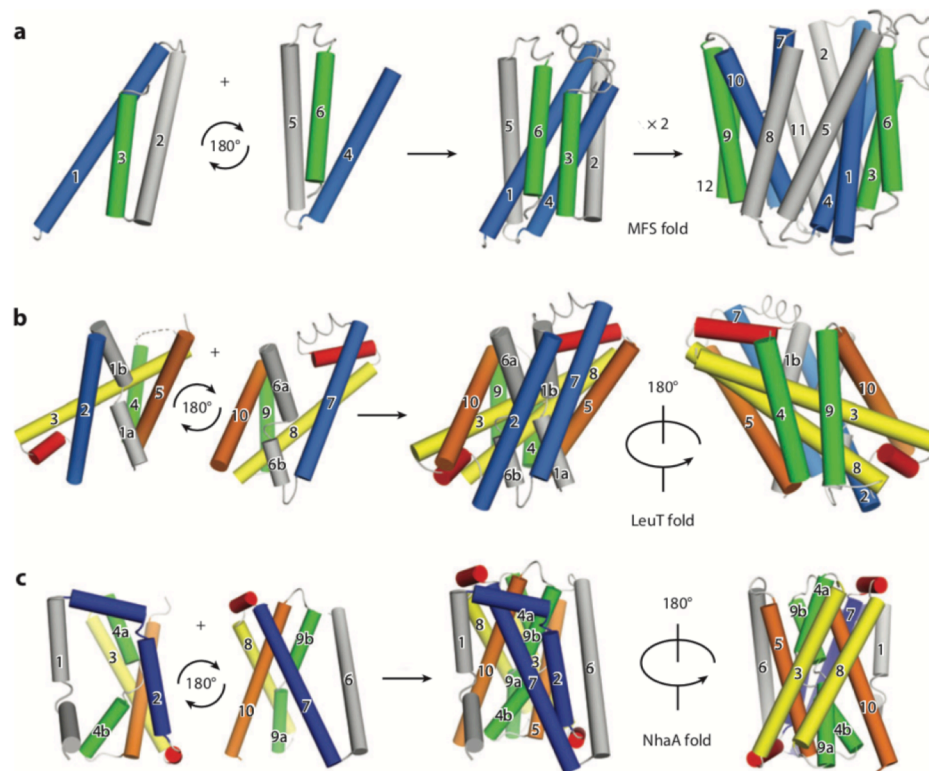
Figure 47. Common folds in secondary active transporters. **(a)** MFS fold with 12 TMH organized in two pseudo-symmetric domains (N- and C-domain), each composed of two inverted repeats of 3 TMH. **(b)** LeuT fold with 10 TMH arranged in two inverted structural repeats of 5 TMH each. TMH 1 and 6 display an unwound segment in the middle of the membrane (broken helices). **(c)** The NhaA fold comprises 10 TMH organized in two 5-TMH inverted structural repeats. TMH 4 and 9 are broken helices that cross each other at the discontinuous region. Reproduced with permission from Shi (2013). Copyright © 2013 Annual Reviews.

outward-facing states, where the substrate-binding site is made accessible to either side of the membrane for cargo upload and release, and a substrate-bound occluded state. This can be achieved by three different strategies: the rocker-switch, the rocking bundle and the elevator. In the first case, the substrate-binding site is located at the interface between two structurally symmetric domains, approximately halfway across the membrane, and coordinated opening/closing of the internal and external gates is accomplished by movement of the two domains relative to each other. The rocking-bundle mechanism is similar to the rocker-switch mechanism, but the two domains are structurally distinct and transport is performed predominantly by the movement

of one domain. Finally, in the elevator mechanism, the substrate binds exclusively (or almost exclusively) to one of two distinct transport domains that undergoes a large rigid-body movement during the transport cycle, while the second domain participates in oligomerization and remains immobile in the membrane (scaffold domain).

In secondary active transporters, aromatic residues are frequently involved in substrate binding and formation of the occluded state. Equally common is the coordination of cations by backbone carbonyl groups of the unwound regions of broken TMH and by negatively charged side chains. Binding of the co-substrate usually increases the binding affinity for the substrate and in proton symporters neutralization of negative charges might be required to overcome the energy barrier for substrate binding or for conformational changes. The two largest superfamilies of secondary active transporters are the major facilitator superfamily (MFS) and the amino acid-polyamine-organocation (APC) superfamily.

12.3. Potassium uptake systems

Potassium is the most abundant intracellular cation in living cells. It is an essential ion, with roles in signaling (Epstein, 2003), activity of several enzymes, in particular of the ribosome (Conn et al., 2002; Suelter, 1970), maintenance of intracellular pH (Booth, 1985), control of gene expression (Prince and Villarejo, 1990) and adaptation to osmotic stress (Gralla and Vargas, 2006). Still, potassium is toxic if accumulated to high concentrations (Cui, 1996; McLaggan et al., 2002). Therefore, the ability of the cell to regulate with precision the abundance of potassium through specialized influx and efflux systems is essential for survival. In animal cells, intracellular potassium concentrations are 10 times greater than in the extracellular medium, and in bacteria, fungi and plant cells this ion can be accumulated by as much as 10^3- to 10^5-fold (Diskowski et al., 2015).

In non-animal cells, potassium uptake transport proteins can be grouped in four classes: K^+ channels, Trk/Ktr/HKT (acronyms for transport of potassium in fungi and bacteria, potassium transporter in bacteria and high-affinity potassium transporter in plants), Kdp (potassium-dependent ATPase) and Kup/HAK/KT (acronyms for potassium uptake in bacteria, high-affinity potassium uptake in fungi and plants, and potassium transporter in plants). The first three systems belong to the superfamily of potassium transporters (SKT) and most likely evolved from the simpler potassium channel KcsA, by gene duplication and fusion (Doyle et al., 1998; Schrempf et al., 1995). Accordingly, the building block of these proteins consists of the MPM motif composed of two transmembrane helices linked by a reentrant P-loop that forms the selectivity filter. The highly conserved selectivity filter of K^+ channels is characterized by the GYG motif and allows a very rapid flux of potassium, while discriminating against similar ions (Thompson and Nimigean, 2013); the gating of these channels is controlled by specialized domains that may respond to membrane voltage, ligands or even membrane tension. The members of the Trk/Ktr/HKT and Kdp families most frequently have a single glycine residue at their selectivity filter (Horie et al., 2001; Mäser et al., 2002; Tholema et al., 2005). Transporters belonging to the Kup/HAK/KT family have been poorly characterized so far, particularly from a structural point of view. These transporters are unrelated to the SKT family, and instead belong to the APC superfamily (Vastermark et al., 2014).

In bacteria, the most frequent potassium transporter is the Trk system, which is in most cases expressed constitutively (Epstein, 2003). Trk has a low affinity for potassium and requires both proton motive force (PMF) and ATP to drive transport (Rhoads and Epstein, 1977). Also Ktr is often a constitutive potassium transporter in bacteria, dependent in this case on the presence of Na^+ (Matsuda et al., 2004; Tholema et al., 1999, 2005; Zulkifli et al., 2010) and ATP (Kröning et al., 2007). While the dependence on specific gradients implied that these transport systems, Trk and Ktr, are secondary active transporters, recent work suggests that they are simply cation channels with low selectivity, in agreement with their simplified selectivity filter (Cao et al., 2013b; Levin and Zhou, 2014). In some bacteria, we can find the multimeric Kdp complex (KdpFABC). Kdp is an

ATP-driven pump with high affinity and high selectivity towards potassium (Fendler et al., 1996, 1999). It is an inducible transporter expressed when potassium is limiting for cell growth (Epstein, 2016). Bacteria may also express Kup, a constitutive low-affinity potassium transporter. Kup has been proposed to be a K^+/H^+ symporter (Haro et al., 1999; Zakharyan and Trchounian, 2001). The topology of Kup from *E. coli* has been determined by reporter fusion and cysteine labeling assays; this transporter is composed of an N-terminal domain with 12 TMH and a cytosolic C-terminus approximately 180 amino acids long (Sato et al., 2014) (Figure 48). The latter has been suggested not to be essential for transport, but it seems to influence its maximum rate (Santa-María et al., 2018). Moreover, it has been shown that transport of potassium by Kup is dependent on four highly conserved acidic residues (D23, E116, E229 and D408) present in its transmembrane domain (Sato et al., 2014).

Recently it was reported that the Gram-positive bacterium *Bacillus subtilis* can grow in the presence of low concentrations of potassium even upon deletion of the genes coding for its high- and low-affinity potassium transporters, KtrAB and KtrCD, respectively. This observation led to the identification of KimA, until then
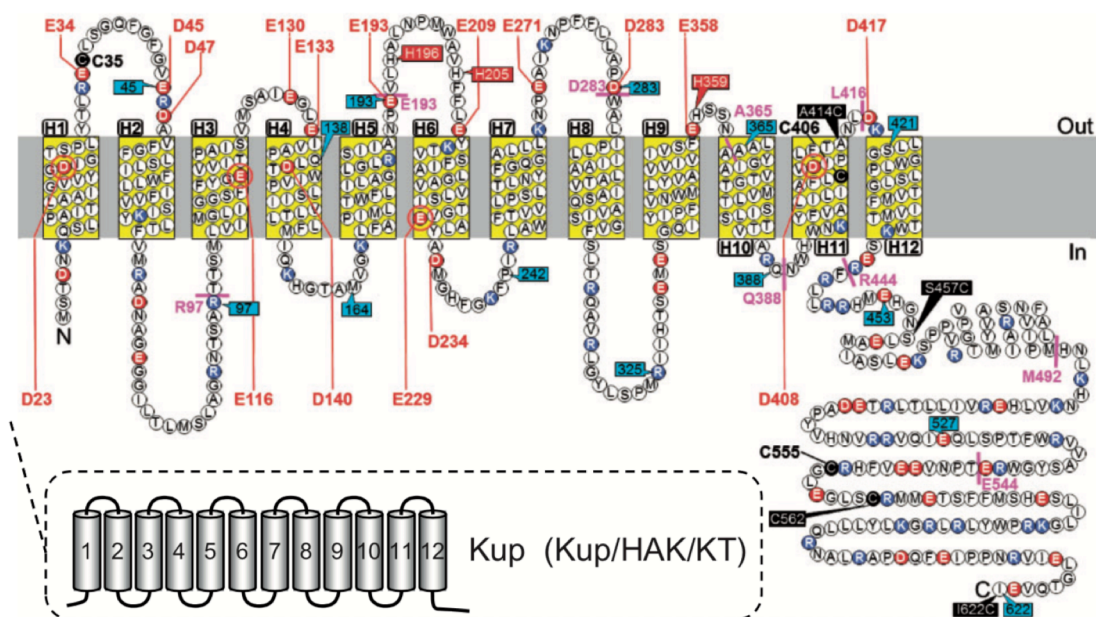
Figure 48. Topology of Kup. Reproduced with permission from Sato et al. (2014).

an unknown high-affinity potassium transporter of 69kDa, that is expressed only at low concentrations of potassium in the external medium (Gundlach et al., 2017). KimA is widespread among bacteria, with homologues in firmicutes, actinobacteria, cyanobacteria and proteobacteria (Gundlach et al., 2017). Our structural and biochemical characterization of KimA shows that it is a K^+/H^+ symporter and a member of the Kup/HAK/KT family. The 3.7 Å map of KimA from *B. subtilis,* determined by single-particle cryo-EM, provides the first structural insights into the transport mechanism used by this family of potassium secondary active transporters.

13. Methods

13.1. Protein expression and purification

KimA was expressed and purified by Dr. Igor Tascón in the group of Dr. Inga Hänelt at the Institute of Biochemistry, Biocenter, Goethe University Frankfurt. Briefly, KimA was expressed in *E. coli* cells. Membranes were solubilised with 2% SMA co-polymer Xiran SLA30010 P20 (2:1 molar ratio of styrene:maleic acid; Polyscope Polymers B. V.) or 1% DDM, in 50 mM Tris pH 8, 100 mM KCl, 400 mM NaCl, overnight at 4 °C. The solubilised material was incubated with Ni-NTA resin overnight, which was then washed with solubilisation buffer supplemented with 50 mM imidazole. The protein was eluted with 500 mM imidazole and further purified by size exclusion chromatography using a Superose 6 10/300 GL column (GE Healthcare) previously equilibrated with 50 mM Tris pH 8, 100 mM KCl (and 0.04% DDM, in the case of the detergent solubilised sample). Fractions containing KimA were pooled, concentrated to ~1 mg/ml and used fresh for preparation of EM specimens.

13.2. Negative-staining

Samples of KimA solubilized with DDM or SMALPs were negatively stained for up to 3 minutes with 1% (w/v) uranyl acetate pH 4, similarly to what was described before (see 3.3. Negative-staining). Electron micrographs were acquired with a CCD camera (Ultrascan 4000) on a Tecnai Spirit at 120 kV under low-lose conditions, at a magnification of 52,000x for a pixel size at the specimen of 2.11 Å. Particles were picked first manually with EMAN boxer (Ludtke et al., 1999) and automatically using Gautomatch (by Kai Zhang, MRC-LMB), after generation of appropriate templates by 2D classification in Relion 2.1 (Scheres, 2012). A total of 3,110 and 67,292 good particles of KimA in SMALP and DMM, respectively, were picked. Two-dimensional class averages were obtained by 2D classification with Relion 2.1.

13.3. Single-particle cryo-EM specimen preparation and data collection

Cryo-EM grids were prepared in a FEI Vitrobot plunge freezer at 10 °C and 90% humidity, using Quantifoil R2/2 holey carbon grids (Quantifoil Micro Tools), pre-treated in chloroform for 1 to 2 hours and freshly glow-discharged at 0.38 mbar and 15 mA for 90 seconds. The grid was blotted 3 seconds after sample application (3 µl of KimA in SMALP at 1.1 mg/ml with 50 µm cyclic di-AMP) for 9 seconds, at blotting force –2, with filter paper #597 (Whatman) and, subsequently, quickly plunged into liquid ethane. Images were collected automatically using EPU (Thermo Scientific), on a FEI Titan Krios operating at 300 kV and aligned as previously described (Mills et al., 2013), with a Gatan K2 camera in counting mode and with an energy filter. The nominal magnification of 130,000x yielded a pixel size at the specimen of 1.077 Å. Each micrograph was recorded as a movie stack with 40 frames over 8 seconds, with a calibrated dose of ~1.77 e$^-$/ Å^2 per frame and defocus values between –0.5 and –3.2 µm.

13.4. Image processing and model building

A set of 5,418 micrographs was collected automatically, of which 4,951 were of sufficient quality for processing. Drift correction and dose weighting of each movie stack were performed with MotionCor2, using a 5x5 grid (total 25 tiles) and its pre-calibrated dose-weighting scheme (Zheng et al., 2016). Whole-micrograph CTF was determined with CTFFIND4 (Rohou and Grigorieff, 2015) on drift-corrected, non-dose weighted movies. After manual picking of a small particle set using EMAN boxer (Ludtke et al., 1999), templates were generated (first by 2D classification and later by reprojection of a low-resolution 3D map) for automatic picking by template matching using Gautomatch (by Kai Zhang, MRC-LMB). The initial dataset contained 2,043,209 particles, windowed with a 208 pixels squared box. A low-resolution initial model was generated from ~19,000 particles using the stochastic gradient descent method implemented in Relion 2.1 and low-pass filtered to 60 Å (Zivanov et al., 2018).

A reference-free 2D classification with ISAC, within Sphire (Moriya et al., 2017), was used to discard clear false positives and bad particles, outputting a subset with 1,614,900 particle images. A more homogeneous set of 314,399 particles was identified through two consecutive rounds of 3D classification, with 5 classes and no symmetry applied, in Relion 3.0 (Zivanov et al., 2018). After Bayesian polishing, CTF refinement and beam tilt estimation with Relion 3.0, refinement of this subset with a soft mask and applied C2 symmetry produced a map at 3.8 Å. However, the resolution degraded towards the periphery of the dimer, especially at the cytoplasmic domain, due to small variations in the relative position of the KimA monomers. Since the signal from a single monomer was insufficient for proper alignment, we attempted to identify a particle subset where these deviations were minimized through a 3D classification of the symmetry-expanded dataset (629,798 particles) with 3 classes, only local searches (healpix order 4) and a reference map low-pass filtered to 4.5 Å; after every five iterations, the map of each class was aligned to a partial map, composed of one transmembrane domain and one cytoplasmic domain, within Chimera (Pettersen et al., 2004), in order to keep the position of one half of the dimer constant, while the position of the other half drove the classification (a similar approach was implemented in Zhang et al. (2018)). The best 3D class contained 198,366 particles. Symmetry expansion was reversed by removal of duplicates, for a total of 149,724 unique particle images. A homogeneous refinement of these particles with CryoSPARC v2 (Punjani et al., 2017) produced a map with a nominal resolution of 3.7 Å and improved densities at the periphery. Local resolution was estimated with CryoSPARC v2 (Punjani et al., 2017).

A homology model was obtained for the transmembrane domain of KimA using Phyre2 (Kelley et al., 2015), which was used as a starting point for modelling with Coot (Emsley et al., 2010). The cytoplasmic domain was built *de novo*. The atomic model was refined in Phenix (Adams et al., 2012) using real space refinement and validated with Molprobity (Williams et al., 2018). UCSF Chimera (Pettersen et al., 2004) was used for visualization of cryo-EM maps and the preparation of figures.

14. Results

14.1. Single-particle negative-staining and cryo-EM analysis of KimA

After some optimization of the purification procedure, guided by negative-stain single-particle analysis, monodisperse samples of KimA from *B. subtilis* in both SMALP and DDM were attained (Figure 49a,b). Reference-free 2D classification of negatively-stained KimA purified with either solubilization strategies produced identical 2D class averages (Figure 49c).
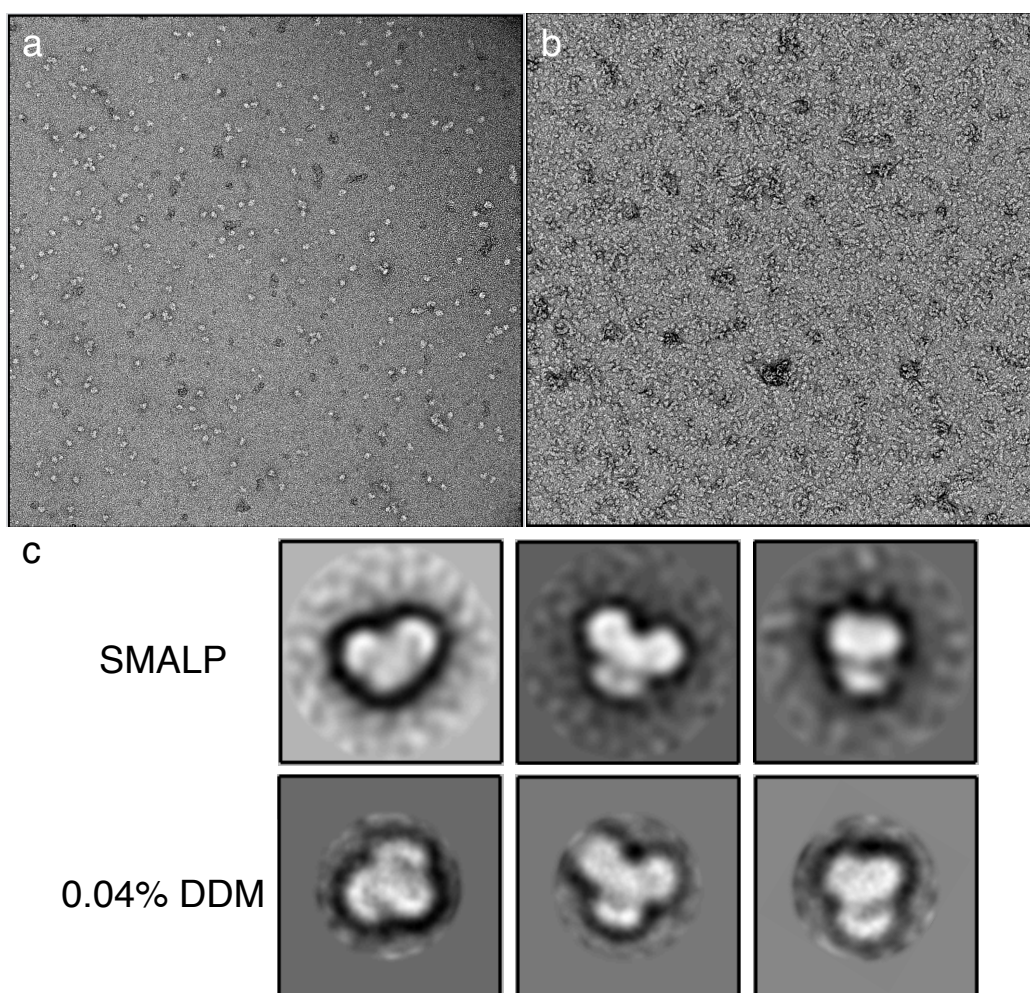
Figure 49. (a,b) Electron micrographs of KimA in SMALP (a) and DDM (b) stained with uranyl acetate, recorded with a Tecnai Spirit operating at 120 kV, at a magnification of 52,000x. **(c)** Negative-stain 2D class averages of KimA in SMALP (upper row) and DDM (lower row) produced by reference-free 2D classification in Relion.

Cryo-EM specimens were prepared with fresh samples of KimA in SMALP and Quantifoil R2/2 holey carbon grids. The small protein showed good contrast at typically used defocus values (80% of the micrographs with defocus below −2.0 μm) and was well distributed in the holes, adopting random orientations (Figure 50a). Over 5,400 micrographs were collected automatically on a FEI Titan Krios with a Gatan K2 Summit camera, of which almost 5,000 were picked using a template-based algorithm. After a conservative analysis of the 2D class averages, approximately 1,600,000 particle images were considered adequate for further processing.

Since an initial 3D reference was not available, one was generated by use of the stochastic descent method within Relion (Zivanov et al., 2018)(Figure 50b). This low-resolution map approximated a structure with C2 symmetry, even though no symmetry was applied, which together with its dimensions was suggestive of a KimA dimer. During analysis of independent runs of 3D classification it became apparent that the relative position of the two monomers fluctuates by a minor degree around the center of mass of the dimer. These deviations were particularly detrimental for the most peripheral areas of the map, but too small to properly drive classification. Attempts to refine a single monomer failed due to the limited signal provided by the 69 kDa protein. Therefore, in order to identify a subset of particles with a more homogeneous placement of the two monomers a modified 3D classification procedure was used where the position of half of the map was kept constant by aligning the map of each class with Chimera to a partial reference every few iterations (Figure 50b). This strategy allowed the classification to focus on the movement of the unrestrained half of the map, facilitating the distinction between different arrangements of the dimer. A set of approximately 150,000 particle images was refined to a 3.7 Å map (Figure 50c,d), with improved densities at the periphery and especially in the soluble domain, which allowed determining the structure of the KimA dimer.
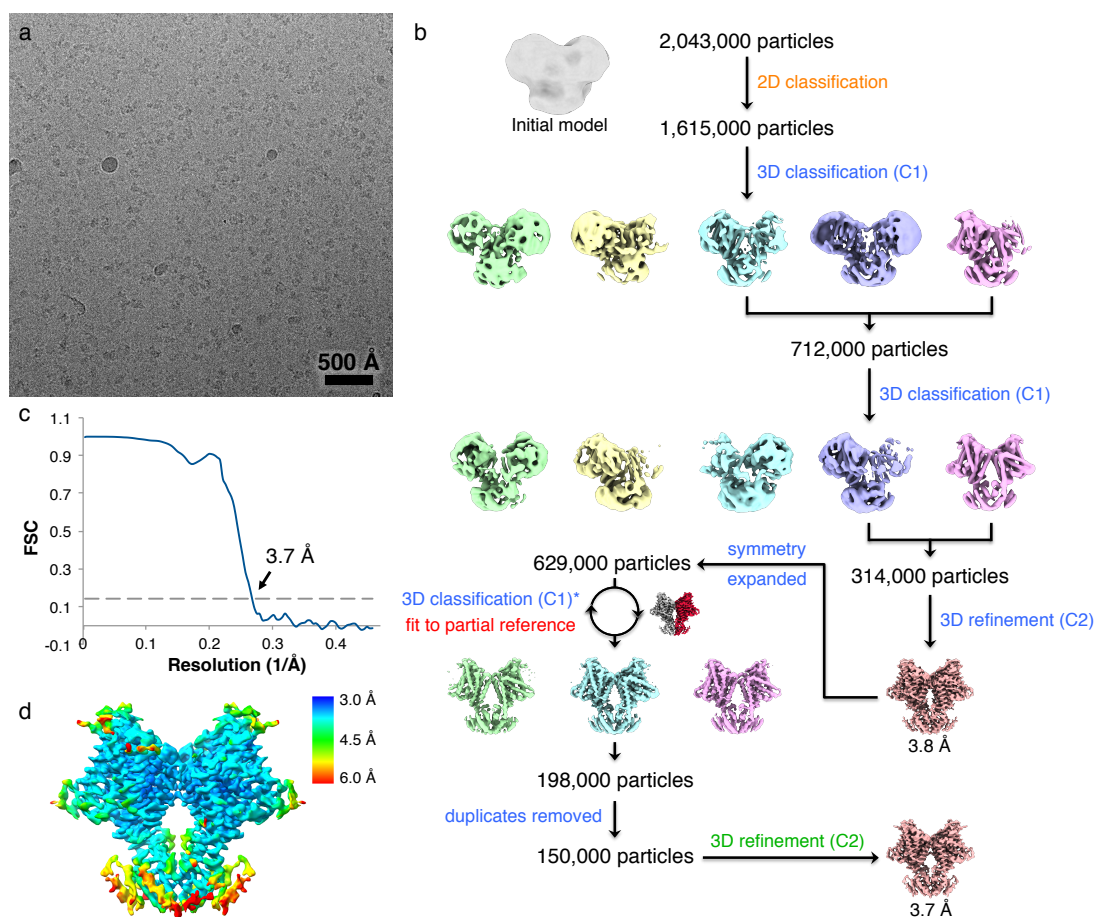
Figure 50. (a) Electron micrograph of KimA in SMALP, recorded with a Gatan K2 Summit electron detector on a FEI Titan Krios with energy filter and operating at 300 kV. **(b)** Image processing workflow used for refinement of a KimA map at 3.7 Å resolution. Processes performed in Relion, Sphire, Cryo-SPARC and Chimera are indicated in blue, orange, green and red, respectively. **(c)** Gold-standard FSC plot of the final KimA map. Resolution estimated at FSC=0.143. **(d)** KimA map colored by local resolution determined by Cryo-SPARC.

14.2. KimA structure

KimA is a homodimer of ~140 kDa with a transmembrane N-terminal domain and a cytoplasmic C-terminal domain. The membrane domains of the two monomers are positioned at an angle of approximately 130° and come into contact only at the boundary between the membrane and the extracellular space (Figure 51). Each soluble domain is placed under the transmembrane domain of the other monomer, with which it establishes some contacts. Moreover, the two
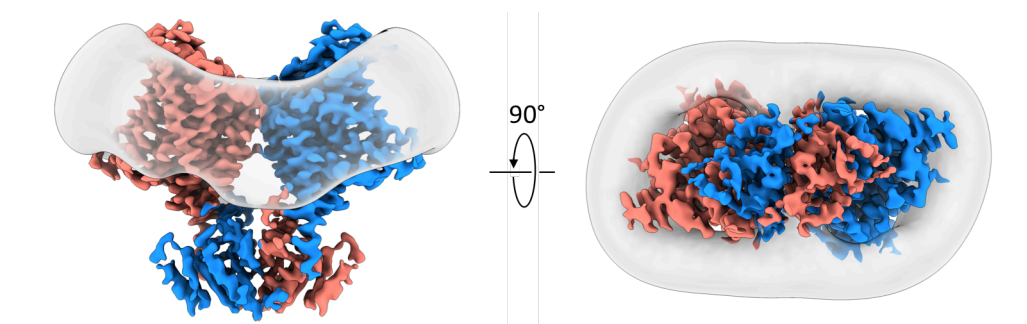
Figure 51. Cryo-EM density map of KimA dimer at 3.7 Å, with the monomers colored in salmon and blue, seen from the membrane (left) and the cytoplasm (right). SMALP density low-pass filtered to 30 Å is shown in grey.

cytoplasmic domains interact extensively with each other and therefore stabilize the dimer.

Each monomer is composed of 12 TMH plus 5 β-strands intercalated with 4 α-helices (Figure 52a,b). The first 10 TMH adopt a typical LeuT fold, with two inverted structural repeats composed of five helices each and discontinuities at the middle of TMH 1 (residues 39 to 45) and TMH 6 (residues 226 to 231) (Figure 52d,e and Figure 53). TMH 4 and 9 face their counterparts in the other monomer, with which they interact at the extracellular side of the membrane and then diverge moving towards the cytoplasmic side, where they are more than 2 nm apart (Cα-Cα distances). In the region between the membrane domains of the two monomers elongated densities are observed, consistent with the presence of lipid molecules that might be involved in stabilizing the dimer (Figure 54). TMH 11 and 12 add to the core transmembrane helices, with the latter extending into the cytoplasm for ~17 Å. A long loop positions then the soluble domain on the opposite side of the dimer.

A parallel β-sheet with 5 strands is found in the cytoplasmic domain of each monomer, that forms within the dimer a continuous 10-stranded mixed β-sheet (Figure 52c). Strands number 5 occupy the central positions in the β-sheet and contribute significantly to the dimerization interface. Some interactions between
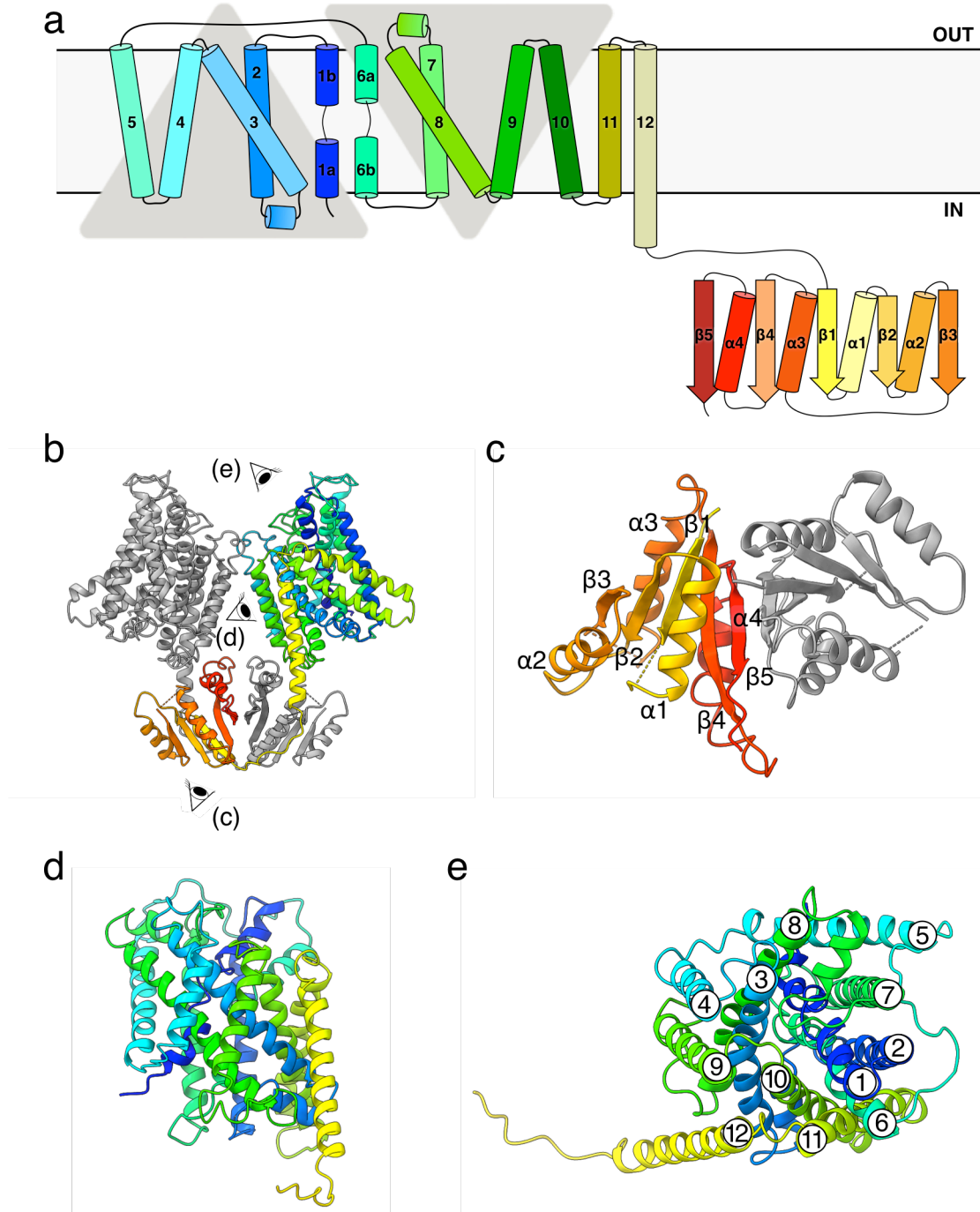
Figure 52. (a) Schematic representation of KimA topology in rainbow colors from blue (N-terminus) to red (C-terminus). **(b)** KimA structure with one monomer depicted in grey and the other in rainbow colors as in (a). **(c)** Soluble domain of KimA dimer. **(d)** Side view and **(e)** view from the periplasm of the membrane domain of a KimA monomer.
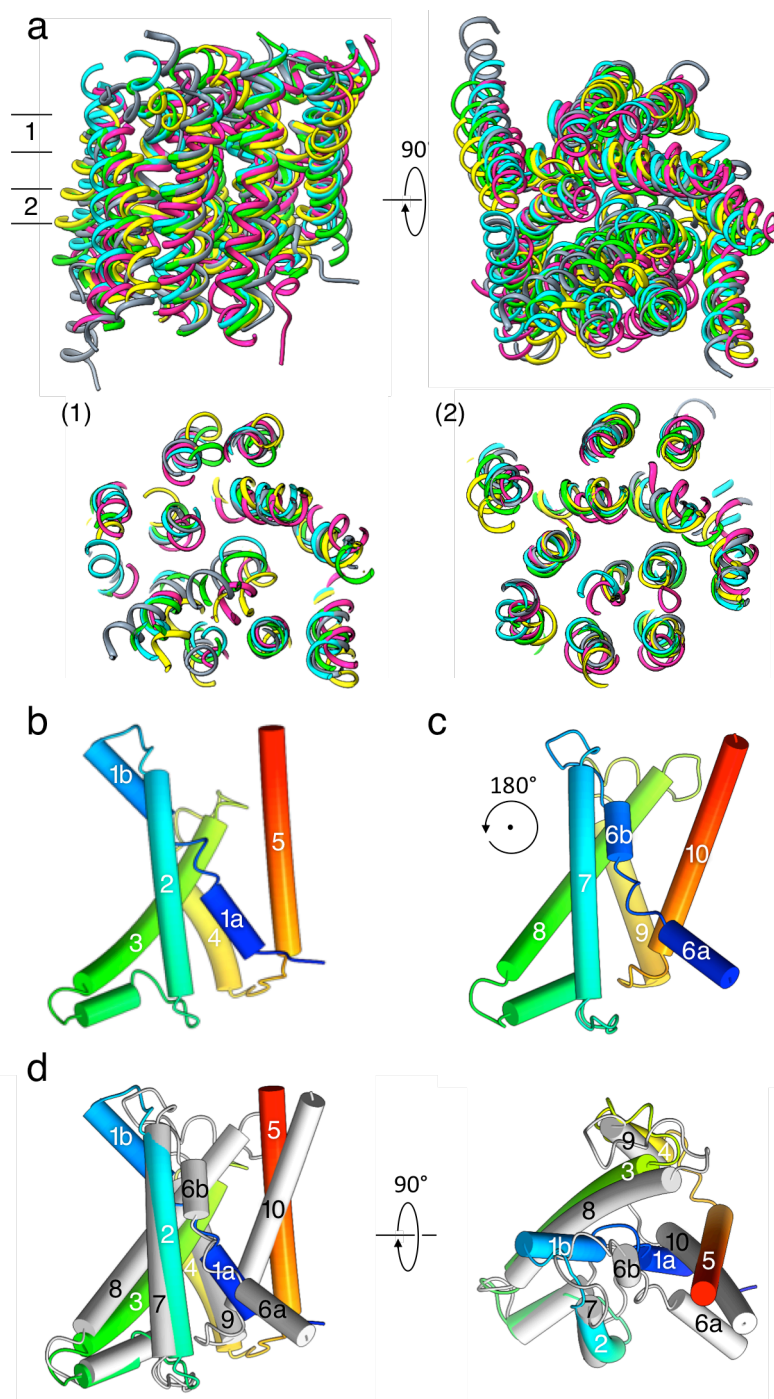
Figure 53. (a) Superimposition of KimA with amino acid transporters with the LeuT fold and 12 TMH. KimA, grey. GkApcT (PDB 5OQT), green. ApcT (PDB 3GIA), cyan. GadC (PDB 4DJI), pink. AdiC (PDB 3LRC), yellow. **(b,c)** KimA structural repeats from TMH 1 to 5 (b) and 6 to 10 (c) with discontinuities in TMH 1 and 6. TMH are colored from blue to red. The second repeat was rotated 180° around the symmetry axis. **(d)** Side view (left) and top view (right) of repeat 1 (rainbow) superimposed with repeat 2 (grey).
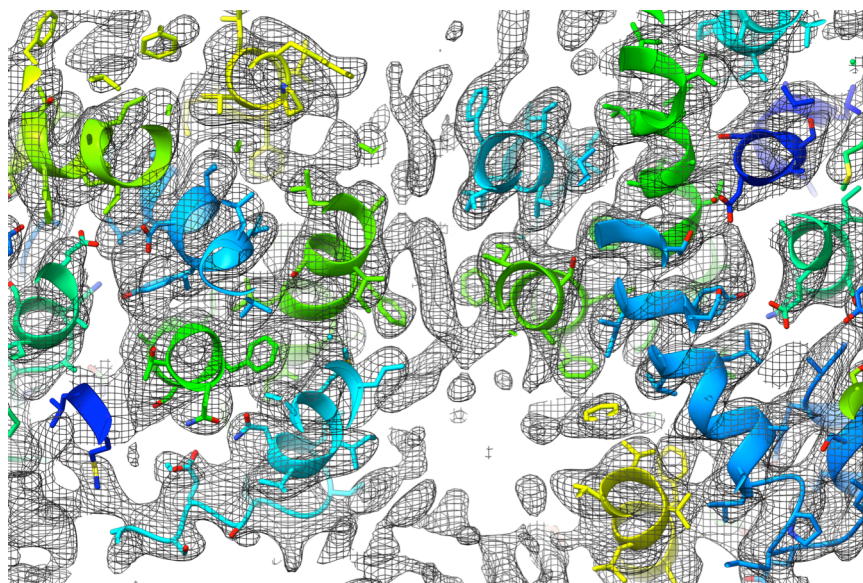
Figure 54. Cryo-EM density map of KimA, with atomic model colored in a rainbow palette, seen from the extracellular side. In the center, a putative lipid density is shown between the two monomers.

the monomers are also established by α-helices 1 and 4. The β-sheet is enclosed by the 8 α-helices from the two monomers.

14.3. Potassium-binding site

In the structure reported here, KimA adopts an inward-facing occluded state (Figure 55), with solvent-filled cavities that extend towards the putative binding site within TMH 1, 3, 6, 8 and 10 (Figure 56). A thick extracellular gate is established by interactions between TMH 1b, 3, 6a and 10, where the main steric occlusion is provided by Y43 (TMH 1b), I48 (TMH 1b) and I374 (TMH 10). On the intracellular side, a long and wide cytoplasmic tunnel leads to the potassium-binding site, which is sealed by a thin gate constructed primarily by D36 (TMH 1a), T121 (TMH 3), T230 (TMH 6b) and Y377 (TMH 10).
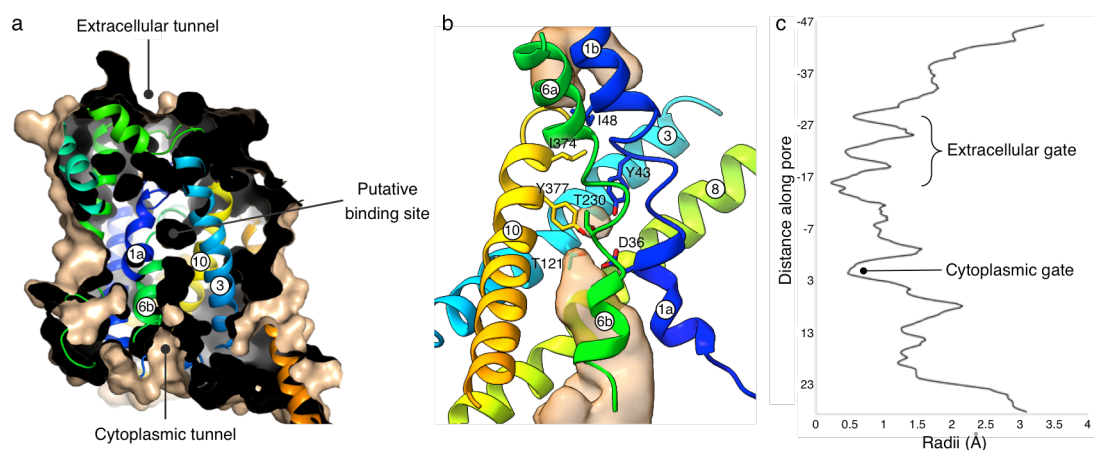
Figure 55. (a) Molecular surface representation of KimA, showing the binding site cavity and the solvent-filled extracellular and cytoplasmic tunnels. **(b)** Density of the KimA pore calculated with HOLLOW (Ho and Gruswitz, 2008), depicted in sandy brown, with the KimA structure showing the main occluding residues. **(c)** Pore radii along the KimA pore determined by HOLE (Smart et al., 1996). Pore calculations were performed by Dr. Igor Tascón, Institute of Biochemistry Goethe University.
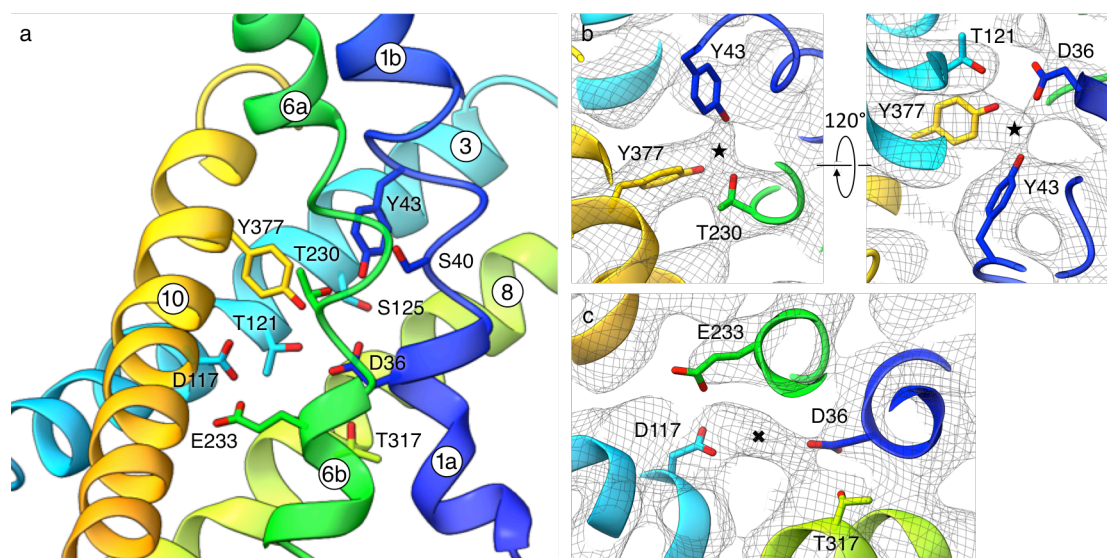
Figure 56. (a) Structure of the potassium-binding site, lined by residues capable of establishing polar interactions with the ligands. **(b)** Zoomed in view into the putative potassium-binding site, showing cryo-EM density. The location of a presumed potassium ion is indicated with a black star (★). **(c)** Zoomed in view showing an unknown density, indicated with a black cross (✖) that bridges residues D36 and D117.

Within the putative binding site a strong density is observed, consistent with the presence of a potassium ion (Figure 56b). Amino acid residues D36 in TMH 1a, S40 and Y43 on the discontinuous region from TMH 1, T121 and S125 in TMH 3, T230 on the discontinuous region of TMH 6 and Y377 in TMH 10 provide an adequate coordination for the ion. Additionally, an elongated density is found bridging the side chains of D36 (TMH 1a) and D117 (TMH 3), immediately below the putative potassium-binding site and near E233 in TMH 6b (Figure 56c).

15. Discussion

15.1. The KimA dimer

KimA forms a stable dimer with a pronounced angle within its transmembrane region, resultant from the assembly of two monomers tilted towards each other (Figure 51). The same angle is observed with SMALP and DDM, which supports the idea that this arrangement is intrinsic to the protein and not due to forces exerted by the SMA polymer. Interestingly, the angle of ~130° between the KimA monomers opposes to the natural curvature of the membrane. A comparable V-like shape is characteristic of ATP synthase dimers and has been shown to be responsible for deformation of the membrane and necessary for formation of mitochondrial cristae (Blum et al., 2019; Strauss et al., 2008). In our cryo-EM map, the SMALP belt around KimA shows a bent shape, with an angle similar to the one observed between the two membrane domains. It is therefore possible to speculate that KimA might have a role on bending or shaping the lipid bilayer.

KimA presents a peculiar dimerization strategy, largely dependent on its soluble domain. This differs substantially from other dimers (and multimers) within the APC superfamily, which establish extensive interactions between transmembrane segments from the several monomers. The limited dimerization interface observed for KimA within the membrane explains, at least partially, the fluctuations observed in the relative position of the monomers. Some elongated densities are observed in the map suggestive of the presence of lipid molecules in the structure, particularly between the two membrane domains. These represent the native lipid environment of KimA, thanks to the use of SMA for membrane solubilization, and might aid the stabilization of the dimer. However, at 3.7 Å resolution these densities are not resolved well enough for a proper assignment and modeling.

The observation of swapped cytoplasmic domains suggests that KimA might be an obligatory dimer. Further investigations are required to elucidate the relevance of KimA dimerization for its function and on the possibility of transport being coordinated between the two monomers.

15.2. Transport by KimA

The interaction of KimA with cyclic di-AMP, a secondary messenger known to regulate several potassium uptake systems, shed light on its role as a potassium transporter (Gundlach et al., 2017). A preliminary analysis shows that, in addition to downregulating expression of KimA by binding to the *kimA* riboswitch (Gundlach et al., 2017), cyclic di-AMP binds to KimA and inhibits potassium uptake (Igor Tascón, personal communication). Notably, deletion of the cytoplasmic domain of KimA abolishes the inhibitory effect of cyclic di-AMP (Jörg Stülke, personal communication), which suggests that this domain is involved in regulation of the transporter. The soluble domain of KimA shows marked differences to the RCK domains to which cyclic di-AMP binds in KtrAB, also in this case for inactivation of the transporter (Kim et al., 2015).

The KimA membrane domain has a LeuT fold typical of the secondary-active transporters that compose the APC superfamily. The structure captured in our map corresponds to a ligand-bound inward-facing occluded state. As previously reported for sodium-coupled transporters (Krishnamurthy et al., 2009), KimA also has a "thick gate" formed by packed TMH and a "thin gate" composed of only a few amino acid side chains, located at the extracellular and intracellular sides, respectively. In the intracellular gate, an aromatic residue (Y377) constitutes the main blockage of the binding site to the solvent. The rearrangement of this bulky side chain into an open configuration is expected to trigger the release of the substrate into the intracellular side. At the extracellular side, considerable conformational changes of several TMH will be necessary for opening the thick gate and Y43 may play a role in regulating the access of the substrate to the binding site. Taking into consideration the LeuT fold of KimA, this transporter is expected to mediate the translocation of potassium according to a rocking-bundle mechanism. A detailed description of the transport cycle will require the determination of structures of KimA in other states.

Within the binding site, KimA has several residues capable of establishing polar interactions with the ligands and a density consistent with a potassium ion is observed, coordinated by D36, Y43, T121, T230 and Y377. Preliminary

complementation assays with KimA single mutants at residues T121, T230 and Y377 (T121A, T230A, Y377F, Y377A) show a reduction in the affinity of the transporter for potassium, while a D36A mutant completely abolished transport (Igor Tascón, personal communication). The location of this putative potassium-binding site also agrees with the substrate binding site observed in other proteins with LeuT fold.

A second density is observed near D36, D117 and E233, which we may speculate to be either a second potassium ion or water molecules. Interestingly, these residues are conserved in Kup (D23, E116 and E229) and have been reported to be required for complementation of growth of an *E. coli* strain depleted of potassium uptake systems (Sato et al., 2014). Preliminary complementation assays show that these acidic residues are also important for transport by KimA. Transport assays with KimA reconstituted into liposomes show that this protein couples potassium transport to the translocation of protons (Figure 57; Igor Tascón, personal communication), similarly to what has been proposed for Kup (Haro et al., 1999; Zakharyan and Trchounian, 2001). A comparative analysis of
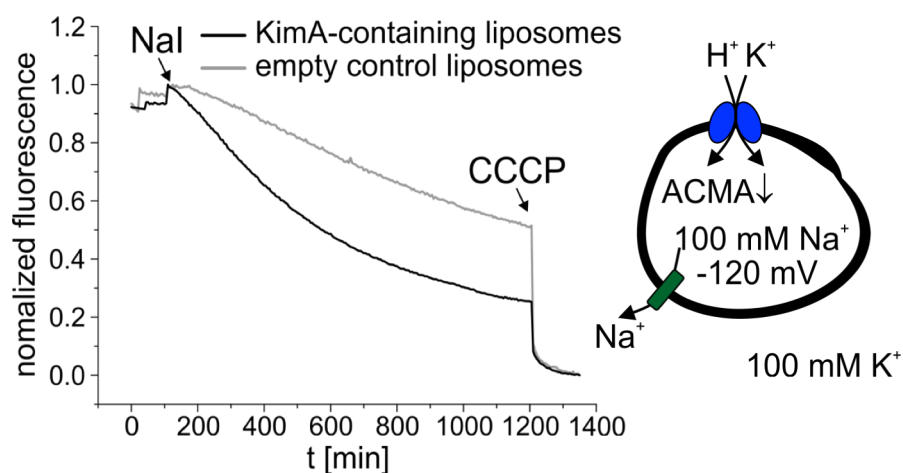
Figure 57. Fluorescence-based transport assay. Liposomes reconstituted with KimA and loaded with 100 mM NaPi pH 7 were diluted in 100 mM KPi pH 7. The addition of a sodium ionophore generated a negative membrane potential of –120 mV, which initiates the co-transport of protons and potassium ions. The fluorescent dye ACMA is quenched as the proton gradient is established. Transport assays were performed by Dr. Igor Tascón, Institute of Biochemistry Goethe University.

the KimA structure with GkApct, an amino acid/proton symporter from the APC family, reveals that D117 and E233 in KimA occupy the same position as the conserved residues E115 and D237 from GkApcT, which were shown to coordinate a water-mediated interaction between TMHs 3 and 6a and, in this way, contribute to the cytoplasmic gate (Jungnickel et al., 2018). Notably, the latter, D237, was proposed to be involved in proton coupling (Jungnickel et al., 2018). The conservation of these residues in KimA suggests that the acidic residues D117 and E233 might have a similar role in the potassium/proton symporter.

16. Conclusions

The structure reported here provided the first structural insights into the mechanism of potassium uptake by members of the Kup/HAK/KT family, with the identification of several residues relevant for transport that are currently being targeted in biochemical assays. In this study, we have also shown that SMALPs can be used for determination of near atomic structures by single-particle cryo-EM, with the advantage of enhanced contrast offered by the use of a detergent-free system. Isolation of membrane proteins in their native environment by use of SMA should be attempted routinely, as this will greatly advance our understanding on the contribution of lipids to protein structure and function.

Further structural analysis of KimA should be pursued in the future, in particular to investigate the mechanism of regulation of this transporter by cyclic di-AMP and to disclose other states in the transport cycle. While the workflow and processing strategy used during this project allowed the identification of a subset of particle images with low conformational heterogeneity, the quality of the map was limited by the inherent flexibility of the dimer. Future structural studies of KimA will most likely benefit from the use of fiducial markers such as nanobodies or antigen-binding fragments (Fab). Additionally, the relevance of the assembly of KimA into dimers and of its characteristic cytoplasmic domain for activity should be investigated. Imaging of proteoliposomes reconstituted with KimA by electron cryo-tomography would also inform on the capabilities of this V-shaped dimer to deform the membrane.

17. PERSPECTIVE

In recent years, the perceived limits of single-particle cryo-EM have been continuously pushed back. The doctoral work presented in this dissertation illustrates how this technique became a major resource in structural biology and, in particular, in the study of membrane proteins. Currently, sub-4 Å structures are routinely determined for various specimens, and the highest resolutions reported are close to 1.5 Å (Zivanov et al., 2018). Small macromolecules, with molecular weight even below 100 kDa, are now being imaged and reconstructed at high-resolution. These achievements have been made possible by the use of direct electron detectors and by important developments in image processing software. Nonetheless, there is still a wide margin for improvement and further progress is expected in the near future.

The pursuit of better cameras will gradually lead to the development of direct electron detectors that converge to an ideal DQE. Moreover, faster camera readouts combined with larger imaging areas and improved schemes for automatic data acquisition will speed up data collection even further but also increase the demands in data storage and computing power. The operation of more reliable phase plates, with constant, stable phase shifts, may allow them to be used routinely in the imaging of small macromolecules. The laser-based phase plate, currently being developed (Campbell et al., 2018), is expected to be a major breakthrough in this respect. Moreover, while deterioration of the image quality by beam-induced movement has been mitigated through the acquisition of movie stacks and use of more stable substrates (gold grids), the first frames, where the sample has suffered the least radiation damage, are still the ones with the highest specimen movement, and effects such as out-of-plane rocking have still to be addressed in drift correction algorithms. Implementation of experimental and computational strategies to retrieve high-resolution information within the initial frames and to fully correct for particle motion will most likely prove to be valuable for the reconstruction of better maps, from smaller datasets. Regarding software, important advances will include better algorithms for the analysis of flexible and heterogeneous particles, fine correction of microscope aberrations and for map and model validation.

Moreover, software for model building and refinement has been developed for use in x-ray crystallography and needs to be better adapted for cryo-EM maps.

Undoubtedly, sample quality remains the central aspect that determines the attainable resolution in cryo-EM. Accordingly, single-particle cryo-EM will benefit from a more general use of customized biochemical approaches, such as the use of Fabs and nanobodies for imaging of small macromolecules, and the use of detergent-free systems like amphipols, nanodiscs and SMALPs for the study of membrane proteins. In regard to grid preparation, freezing robots are under development, which aim primarily to enhance reproducibility and reduce the required amount of sample, but might also offer advantages on problems related with the protein interaction with the air-water interface. In addition, several strategies are being pursued for the implementation of time-resolved cryo-EM for visualization of short-lived states not accessible to standard cryo-EM analysis.

Important breakthroughs will also take place in other fields of cryo-EM. In particular, cryo-electron tomography and subtomogram averaging are expected to move towards higher resolutions and, more relevantly, more complex targets. The use of auxiliary techniques such as focused ion beam (FIB) milling and correlative light electron microscopy (CLEM) will be fundamental in this process.

Lastly, it will be fundamental to make cryo-EM widely accessible to the scientific community, but the price of specialized cryo-EM equipment (microscopes, cameras and freezing apparatus) is prohibitive for most individual laboratories. Numerous national and international imaging centers are now in place or being set up, which provide both access to high-end microscopes and expert support to less experienced users. Nonetheless, more affordable microscopes are required, to be used for in-house sample and specimen optimization before data collection at a high-end facility.

Single-particle cryo-EM will continue in this way to revolutionize the field of structural biology, with more biological targets falling within the scope of this technique. The use of single-particle analysis for structural-based drug design will also continue to grow. What is more, we will progressively move towards the

analysis of conformational and energetic landscapes of the macromolecules that can provide a comprehensive view of the dynamics of the system, making cryo-EM the structural biology technique for the 21th century.

18. APPENDICES

Appendix A – Sequence conservation in ActC. Residues from the putative proton half-channels and quinol-binding site are highlighted with asterisks (*) and pink dots (•), respectively. The residue involved in subunit cross-talk (S245) is indicated by a green square (■). Sequence alignments were performed by Filipa Calisto and Dr. Patrícia N. Refojo, ITQB.

Appendix B – Sequence conservation in ActF. Residues forming the putative proton half-channels are marked by black triangles (▲). The residue involved in subunit cross-talk (Y284) is indicated by a green square (■). Sequence alignments were performed by Filipa Calisto and Dr. Patrícia N. Refojo, ITQB.

Appendix C – Sequence conservation in ActD. The residue involved in subunit cross-talk (E122) is indicated by a green square (■). Sequence alignments were performed by Filipa Calisto and Dr. Patrícia N. Refojo, ITQB.

Appendix A
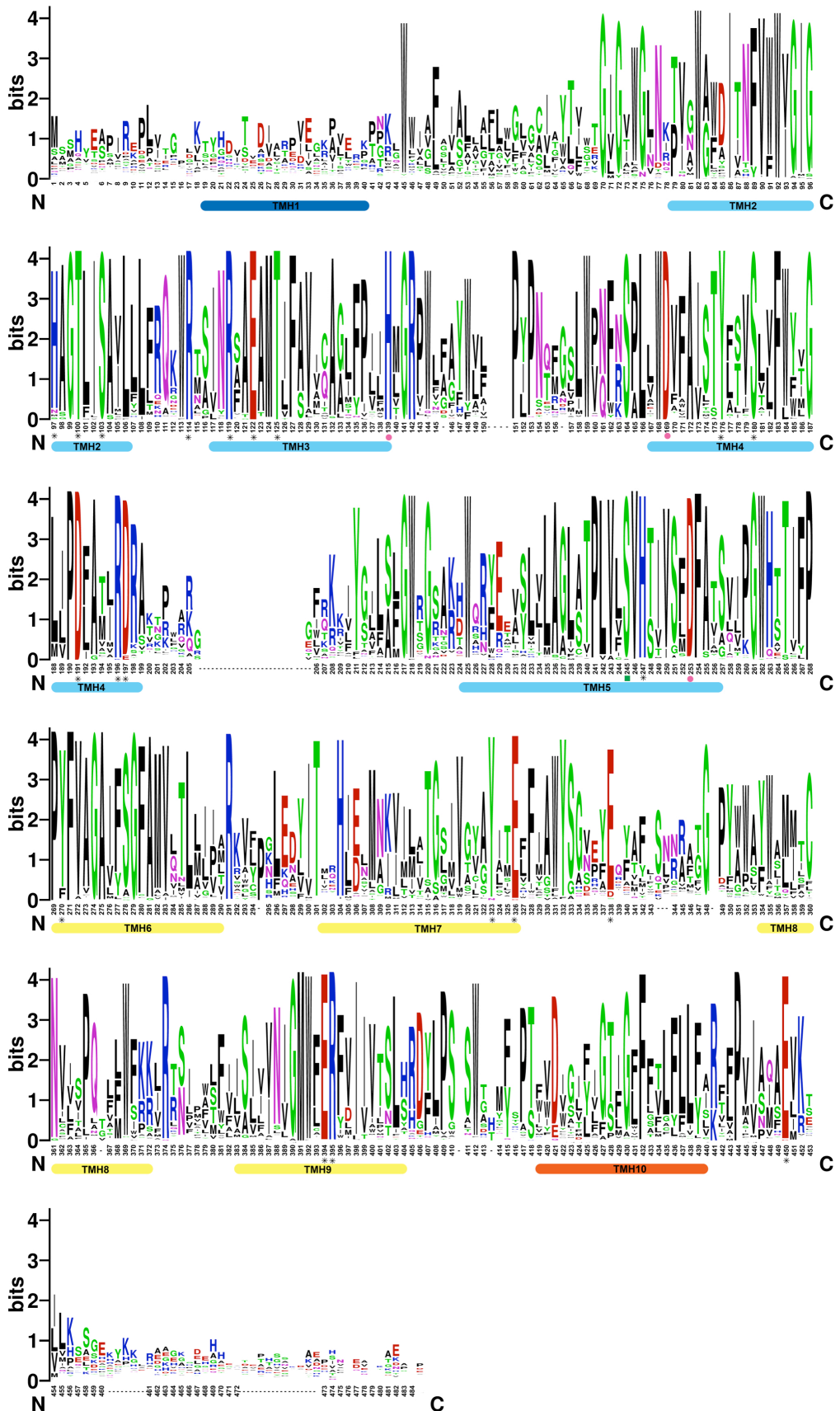
Appendix B

Appendix C

III. References

Abramson, J., Riistama, S., Larsson, G., Jasaitis, A., Svensson-Ek, M., Laakkonen, L., Puustinen, A., Iwata, S., and Wikström, M. (2000). The structure of the ubiquinol oxidase from *Escherichia coli* and its ubiquinone binding site. *Nature Structural Biology 7*, 910–917.

Acín-Pérez, R., Bayona-Bafaluy, M.P., Fernández-Silva, P., Moreno-Loshuertos, R., Pérez-Martos, A., Bruno, C., Moraes, C.T., and Enríquez, J.A. (2004). Respiratory complex III is required to maintain complex I in mammalian mitochondria. *Molecular Cell 13*, 805–815.

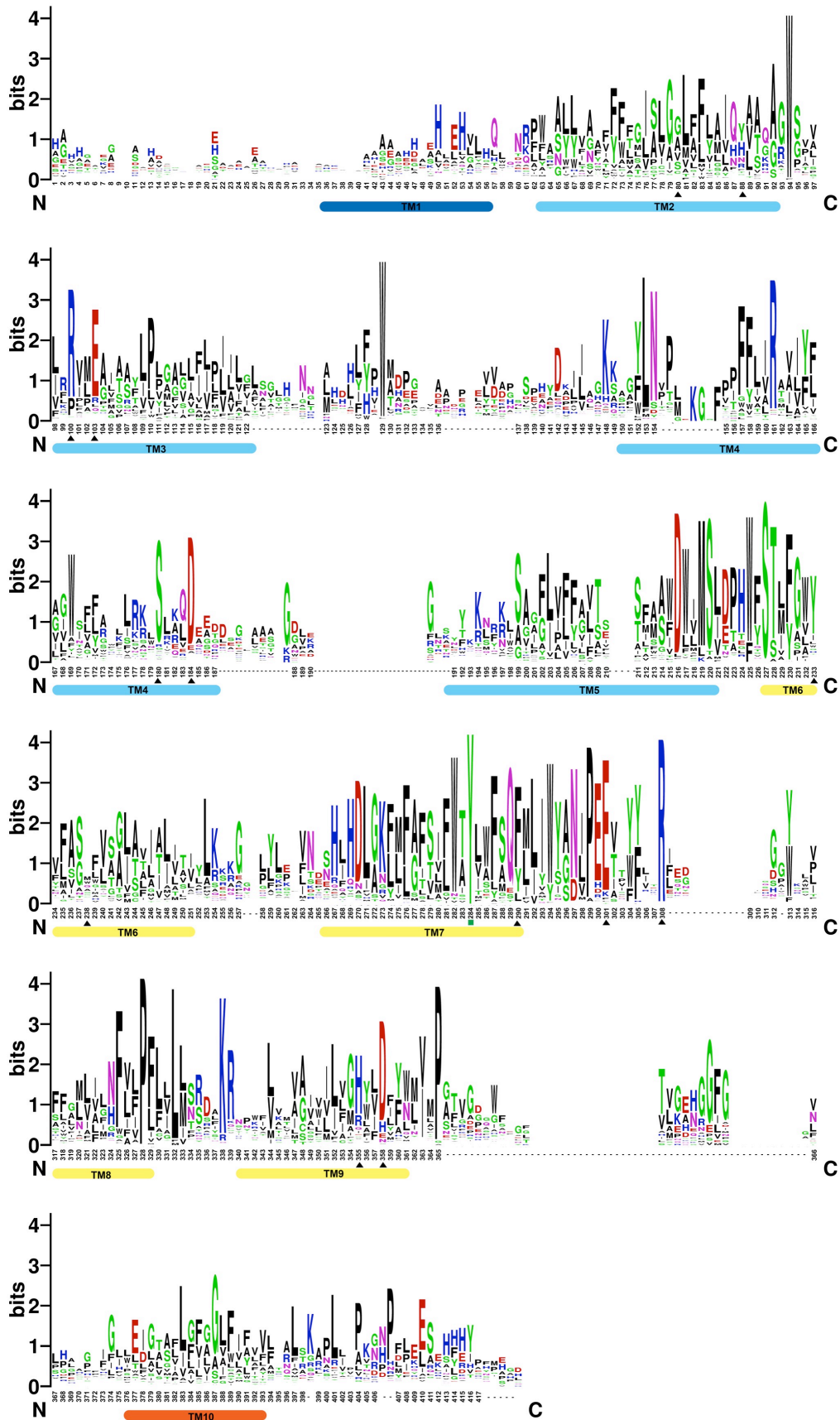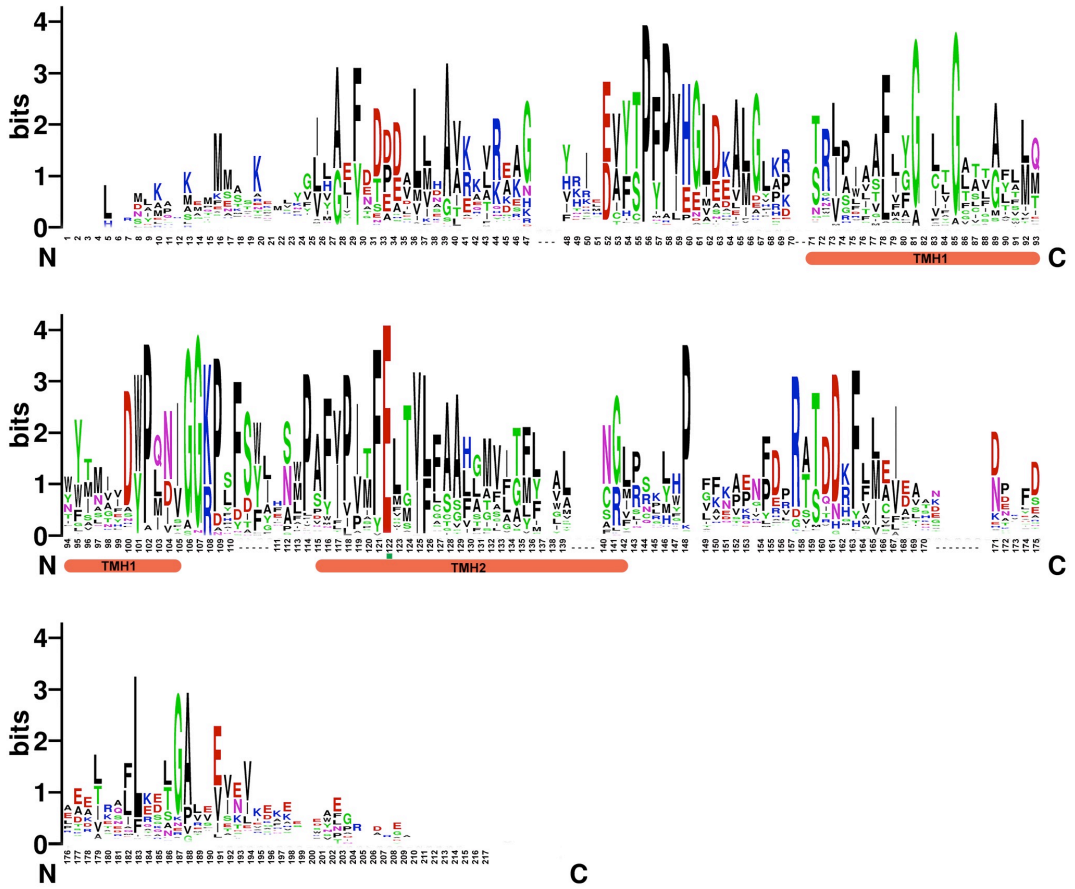Acín-Pérez, R., Fernández-Silva, P., Peleato, M.L., Pérez-Martos, A., and Enriquez, J.A. (2008). Respiratory active mitochondrial supercomplexes. *Molecular Cell 32*, 529–539.

Adams, P.D., Afonine, P.V., Bunkóczi, G., Chen, V.B., Davis, I.W., Echols, N., Headd, J.J., Hung, L.W., Kapral, G.J., Grosse-Kunstleve, R.W., et al. (2012). *PHENIX*: a comprehensive Python-based system for macromolecular structure solution. In International Tables for Crystallography: Crystallography of Biological Macromolecules, E. Arnold, D.M. Himmel, and M.G. Rossmann, eds. (Chester, England: International Union of Crystallography), pp. 539–547.

Adrian, M., Dubochet, J., Lepault, J., and McDowall, A.W. (1984). Cryo-electron microscopy of viruses. *Nature 308*, 32–36.

Agip, A.-N.A., Blaza, J.N., Bridges, H.R., Viscomi, C., Rawson, S., Muench, S.P., and Hirst, J. (2018). Cryo-EM structures of complex I from mouse heart mitochondria in two biochemically defined states. *Nature Structural & Molecular Biology 25*, 548–556.

Alfredsson, G.A., Kristjansson, J.K., Hjorleifsdottir, S., and Stetter, K.O. (1988). *Rhodothermus marinus*, gen. nov., sp. nov., a thermophilic, halophilic bacterium from submarine hot springs in Iceland. *Journal of Microbiology Research 134*, 299–306.

Alnajjar, K.S., Hosler, J., and Prochaska, L. (2014). Role of the N-terminus of subunit III in proton uptake in cytochrome *c* oxidase of *Rhodobacter sphaeroides*. *Biochemistry 53*, 496–504.

Althoff, T., Mills, D.J., Popot, J.L., and Kühlbrandt, W. (2011). Arrangement of electron transport chain components in bovine mitochondrial supercomplex $I_1III_2IV_1$. *The EMBO Journal 30*, 4652–4664.

Arnold, S., and Kadenbach, B. (1997). Cell respiration is controlled by ATP, an allosteric inhibitor of cytochrome-*c* oxidase. *European Journal of Biochemistry / FEBS 249*, 350–354.

Arnold, S., Goglia, F., and Kadenbach, B. (1998). 3,5-Diiodothyronine binds to subunit Va of cytochrome-*c* oxidase and abolishes the allosteric inhibition of respiration by ATP. *European Journal of Biochemistry / FEBS 252*, 325–330.

Bai, X., Rajendra, E., Yang, G., Shi, Y., and Scheres, S.H.W. (2015). Sampling the conformational space of the catalytic subunit of human γ-secretase. *ELife 4*, e11182.

Bai, X.-C., Fernandez, I.S., McMullan, G., and Scheres, S.H.W. (2013). Ribosome structures to near-atomic resolution from thirty thousand cryo-EM particles. *ELife 2*, e00461.

Barad, B.A., Echols, N., Wang, R.Y.-R., Cheng, Y., DiMaio, F., Adams, P.D., and Fraser, J.S. (2015). EMRinger: side chain-directed model and map validation for 3D cryo-electron microscopy. *Nature Methods 12*, 943–946.

Berger, I., Hershkovitz, E., Shaag, A., Edvardson, S., Saada, A., and Elpeleg, O. (2008). Mitochondrial complex I deficiency caused by a deleterious NDUFA11 mutation. *Annals of Neurology 63*, 405–408.

Berry, E.A., De Bari, H., and Huang, L.S. (2013). Unanswered questions about the structure of cytochrome bc_1 complexes. *Biochimica et Biophysica Acta 1827*, 1258–1277.

Bianchi, C., Fato, R., Genova, M.L., Castelli, G.P., and Lenaz, G. (2003). Structural

and functional organization of Complex I in the mitochondrial respiratory chain. *BioFactors (Oxford, England) 18*, 3–9.

Bianchi, C., Genova, M.L., Parenti Castelli, G., and Lenaz, G. (2004). The mitochondrial respiratory chain is partially organized in a supercomplex assembly: kinetic evidence using flux control analysis. *The Journal of Biological Chemistry 279*, 36562–36569.

Bjornsdottir, S.H., Blondal, T., Hreggvidsson, G.O., Eggertsson, G., Petursdottir, S., Hjorleifsdottir, S., Thorbjarnardottir, S.H., and Kristjansson, J.K. (2006). *Rhodothermus marinus*: physiology and molecular biology. *Extremophiles: Life Under Extreme Conditions 10*, 1–16.

Blaza, J.N., Serreli, R., Jones, A.J.Y., Mohammed, K., and Hirst, J. (2014). Kinetic evidence against partitioning of the ubiquinone pool and the catalytic relevance of respiratory-chain supercomplexes. *Proceedings of the National Academy of Sciences of the United States of America 111*, 15735–15740.

Blum, T.B., Hahn, A., Meier, T., Davies, K.M., and Kühlbrandt, W. (2019). Dimers of mitochondrial ATP synthase induce membrane curvature and self-assemble into rows. *Proceedings of the National Academy of Sciences of the United States of America*.

Bonne, G., Seibel, P., Possekel, S., Marsac, C., and Kadenbach, B. (1993). Expression of human cytochrome *c* oxidase subunits during fetal development. *European Journal of Biochemistry / FEBS 217*, 1099–1107.

Booth, I.R. (1985). Regulation of cytoplasmic pH in bacteria. *Microbiological Reviews 49*, 359–378.

Booth, C., and Mooney, P. (2013). Applications of electron-counting direct-detection cameras in high-resolution cryo-electron microscopy. *Microsopy and Analysis 27*, 13–21.

Brenner, S., and Horne, R.W. (1959). A negative staining method for high resolution electron microscopy of viruses. *Biochimica et Biophysica Acta 34*, 103–

110.

Brilot, A.F., Chen, J.Z., Cheng, A., Pan, J., Harrison, S.C., Potter, C.S., Carragher, B., Henderson, R., and Grigorieff, N. (2012). Beam-induced motion of vitrified specimen on holey carbon film. *Journal of Structural Biology 177*, 630–637.

Bruno, C., Santorelli, F.M., Assereto, S., Tonoli, E., Tessa, A., Traverso, M., Scapolan, S., Bado, M., Tedeschi, S., and Minetti, C. (2003). Progressive exercise intolerance associated with a new muscle-restricted nonsense mutation (G142X) in the mitochondrial cytochrome *b* gene. *Muscle & Nerve 28*, 508–511.

Brzezinski, P., and Adelroth, P. (1998). Pathways of proton transfer in cytochrome *c* oxidase. *Journal of Bioenergetics and Biomembranes 30*, 99–107.

Buschmann, S., Warkentin, E., Xie, H., Langer, J.D., Ermler, U., and Michel, H. (2010). The structure of cbb_3 cytochrome oxidase provides insights into proton pumping. *Science 329*, 327–330.

Campbell, S.L., Schwartz, O., Axelrod, J.J., TUrnbaugh, C., Glaeser, R.M., and Muller, H. (2018). A laser-based phase plate for phase contrast transmission electron microscopy. In Frontiers in Optics / Laser Science, (Washington, D.C.: OSA), p. FW7B.5.

Cao, E., Liao, M., Cheng, Y., and Julius, D. (2013a). TRPV1 structures in distinct conformations reveal activation mechanisms. *Nature 504*, 113–118.

Cao, Y., Pan, Y., Huang, H., Jin, X., Levin, E.J., Kloss, B., and Zhou, M. (2013b). Gating of the TrkH ion channel by its associated RCK protein TrkA. *Nature 496*, 317–322.

Carroll, J., Shannon, R.J., Fearnley, I.M., Walker, J.E., and Hirst, J. (2002). Definition of the nuclear encoded protein composition of bovine heart mitochondrial complex I. Identification of two new subunits. *The Journal of Biological Chemistry 277*, 50311–50317.

Castellani, M., Covian, R., Kleinschroth, T., Anderka, O., Ludwig, B., and Trumpower, B.L. (2010). Direct demonstration of half-of-the-sites reactivity in

the dimeric cytochrome bc_1 complex: enzyme with one inactive monomer is fully active but unable to activate the second ubiquinol oxidation site in response to ligand binding at the ubiquinone reduction site. *The Journal of Biological Chemistry 285*, 502–510.

Chance, B., and Williams, G.R. (1955). Respiratory enzymes in oxidative phosphorylation. III. The steady state. *The Journal of Biological Chemistry 217*, 409–427.

Chen, Y.-C., Taylor, E.B., Dephoure, N., Heo, J.-M., Tonhato, A., Papandreou, I., Nath, N., Denko, N.C., Gygi, S.P., and Rutter, J. (2012). Identification of a protein mediating respiratory supercomplex stability. *Cell Metabolism 15*, 348–360.

Cheng, Y. (2015). Single-particle cryo-EM at crystallographic resolution. *Cell 161*, 450–457.

Cheng, A., Tan, Y.Z., Dandey, V.P., Potter, C.S., and Carragher, B. (2016). Strategies for automated cryo-EM data collection using direct detectors. *Methods in Enzymology 579*, 87–102.

Cheng, Y., Grigorieff, N., Penczek, P.A., and Walz, T. (2015). A primer to single-particle cryo-electron microscopy. *Cell 161*, 438–449.

Cogliati, S., Calvo, E., Loureiro, M., Guaras, A.M., Nieto-Arellano, R., Garcia-Poyatos, C., Ezkurdia, I., Mercader, N., Vázquez, J., and Enriquez, J.A. (2016). Mechanism of super-assembly of respiratory complexes III and IV. *Nature 539*, 579–582.

Collins, M.D., and Jones, D. (1981). Distribution of isoprenoid quinone structural types in bacteria and their taxonomic implication. *Microbiological Reviews 45*, 316–354.

Conn, G.L., Gittis, A.G., Lattman, E.E., Misra, V.K., and Draper, D.E. (2002). A compact RNA tertiary structure contains a buried backbone-K^+ complex. *Journal of Molecular Biology 318*, 963–973.

Coombs, D.H., and Watts, N.R. (1985). Generating sucrose gradients in three

minutes by tilted tube rotation. *Analytical Biochemistry 148*, 254–259.

Costa, T.R.D., Ignatiou, A., and Orlova, E.V. (2017). Structural analysis of protein complexes by cryo electron microscopy. *Methods in Molecular Biology 1615*, 377–413.

Covian, R., and Trumpower, B.L. (2008). Regulatory interactions in the dimeric cytochrome bc_1 complex: the advantages of being a twin. *Biochimica et Biophysica Acta 1777*, 1079–1091.

Crofts, A.R., Hong, S., Ugulava, N., Barquera, B., Gennis, R., Guergova-Kuras, M., and Berry, E.A. (1999). Pathways for proton release during ubihydroquinone oxidation by the bc_1 complex. *Proceedings of the National Academy of Sciences of the United States of America 96*, 10021–10026.

Cui, C. (1996). Effect of mutation of potassium-efflux system, KefA, on mechanosensitive channels in the cytoplasmic membrane of *Escherichia coli*. *Journal of Membrane Biology 150*, 143–152.

Cukierman, S. (2006). Et tu, Grotthuss! and other unfinished stories. *Biochimica et Biophysica Acta 1757*, 876–885.

Danev, R., and Baumeister, W. (2016). Cryo-EM single particle analysis with the Volta phase plate. *ELife 5*, e13046.

Darrouzet, E., Valkova-Valchanova, M., Moser, C.C., Dutton, P.L., and Daldal, F. (2000). Uncovering the [2Fe2S] domain movement in cytochrome bc_1 and its implications for energy conversion. *Proceedings of the National Academy of Sciences of the United States of America 97*, 4567–4572.

D'Aurelio, M., Gajewski, C.D., Lenaz, G., and Manfredi, G. (2006). Respiratory chain supercomplexes set the threshold for respiration defects in human mtDNA mutant cybrids. *Human Molecular Genetics 15*, 2157–2169.

Davies, K.M., Blum, T.B., and Kühlbrandt, W. (2018). Conserved *in situ* arrangement of complex I and III$_2$ in mitochondrial respiratory chain supercomplexes of mammals, yeast, and plants. *Proceedings of the National*

Academy of Sciences of the United States of America 115, 3024–3029.

De Rosier, D.J., and Klug, A. (1968). Reconstruction of three dimensional structures from electron micrographs. *Nature 217*, 130–134.

Diaz, F., Fukui, H., Garcia, S., and Moraes, C.T. (2006). Cytochrome *c* oxidase is required for the assembly/stability of respiratory complex I in mouse fibroblasts. *Molecular and Cellular Biology 26*, 4872–4881.

Dieteren, C.E.J., Koopman, W.J.H., Swarts, H.G., Peters, J.G.P., Maczuga, P., van Gemst, J.J., Masereeuw, R., Smeitink, J.A.M., Nijtmans, L.G.J., and Willems, P.H.G.M. (2012). Subunit-specific incorporation efficiency and kinetics in mitochondrial complex I homeostasis. *The Journal of Biological Chemistry 287*, 41851–41860.

D'Imprima, E., Floris, D., Joppe, M., Sánchez, R., Grininger, M., and Kühlbrandt, W. (2018). The deadly touch: protein denaturation at the water-air interface and how to prevent it. *BioRxiv* 400432.

Diskowski, M., Mikusevic, V., Stock, C., and Hänelt, I. (2015). Functional diversity of the superfamily of K^+ transporters to meet various requirements. *Biological Chemistry 396*, 1003–1014.

Doyle, D.A., Morais Cabral, J., Pfuetzner, R.A., Kuo, A., Gulbis, J.M., Cohen, S.L., Chait, B.T., and MacKinnon, R. (1998). The structure of the potassium channel: molecular basis of K^+ conduction and selectivity. *Science 280*, 69–77.

Dubochet, J., Adrian, M., Chang, J.J., Homo, J.C., Lepault, J., McDowall, A.W., and Schultz, P. (1988). Cryo-electron microscopy of vitrified specimens. *Quarterly Reviews of Biophysics 21*, 129–228.

Dudkina, N.V., Eubel, H., Keegstra, W., Boekema, E.J., and Braun, H.-P. (2005). Structure of a mitochondrial supercomplex formed by respiratory-chain complexes I and III. *Proceedings of the National Academy of Sciences of the United States of America 102*, 3225–3229.

Dudkina, N.V., Kudryashev, M., Stahlberg, H., and Boekema, E.J. (2011). Interaction of complexes I, III, and IV within the bovine respirasome by single

particle cryo electron tomography. *Proceedings of the National Academy of Sciences of the United States of America 108*, 15196–15200.

Efremov, R.G., and Sazanov, L.A. (2011). Structure of the membrane domain of respiratory complex I. *Nature 476*, 414–420.

Elmlund, D., and Elmlund, H. (2012). SIMPLE: Software for ab initio reconstruction of heterogeneous single-particles. *Journal of Structural Biology 180*, 420–427.

Emsley, P., Lohkamp, B., Scott, W.G., and Cowtan, K. (2010). Features and development of Coot. *Acta Crystallographica. Sect. D, Biological Crystallography 66*, 486–501.

Enríquez, J.A. (2016). Supramolecular organization of respiratory complexes. *Annual Review of Physiology 78*, 533–561.

Epstein, W. (2003). The roles and regulation of potassium in bacteria. (Elsevier), pp. 293–320.

Epstein, W. (2016). The KdpD sensor kinase of *Escherichia coli* responds to several distinct signals to turn on expression of the Kdp transport system. *Journal of Bacteriology 198*, 212–220.

Ewart, G.D., Zhang, Y.Z., and Capaldi, R.A. (1991). Switching of bovine cytochrome *c* oxidase subunit VIa isoforms in skeletal muscle during development. *FEBS Letters 292*, 79–84.

Fedor, J.G., and Hirst, J. (2018). Mitochondrial supercomplexes do not enhance catalysis by quinone channeling. *Cell Metabolism 28*, 525–531.e4.

Fendler, K., Dröse, S., Altendorf, K., and Bamberg, E. (1996). Electrogenic K^+ transport by the Kdp-ATPase of *Escherichia coli*. *Biochemistry 35*, 8009–8017.

Fendler, K., Dröse, S., Epstein, W., Bamberg, E., and Altendorf, K. (1999). The Kdp-ATPase of *Escherichia coli* mediates an ATP-dependent, K^+-independent electrogenic partial reaction. *Biochemistry 38*, 1850–1856.

Fernandes, A.S., Pereira, M.M., and Teixeira, M. (2001). The succinate dehydrogenase from the thermohalophilic bacterium *Rhodothermus marinus*: redox–Bohr effect on heme b_L. *Journal of Bioenergetics and Biomembranes 33*, 343–352.

Fernandes, A.S., Pereira, M.M., and Teixeira, M. (2002). Purification and characterization of the Complex I from the respiratory chain of *Rhodothermus marinus*. *Journal of Bioenergetics and Biomembranes 34*, 413–421.

Fiedorczuk, K., and Sazanov, L.A. (2018). Mammalian mitochondrial Complex I structure and disease-causing mutations. *Trends in Cell Biology 28*, 835–867.

Fisher, N., and Rich, P.R. (2000). A motif for quinone binding sites in respiratory and photosynthetic systems. *Journal of Molecular Biology 296*, 1153–1162.

Frank, J. (1975). Averaging of low exposure electron micrographs of non-periodic objects. *Ultramicroscopy 1*, 159–162.

Frank, J. (2006). Three-dimensional electron microscopy of macromolecular assemblies: visualization of biological molecules in their native state (Oxford University Press).

Fujiyoshi, Y. (1998). The structural study of membrane proteins by electron crystallography. *Advances in Biophysics 35*, 25–80.

Gao, X., Xin, Y., Bell, P.D., Wen, J., and Blankenship, R.E. (2010). Structural analysis of alternative complex III in the photosynthetic electron transfer chain of *Chloroflexus aurantiacus*. *Biochemistry 49*, 6670–6679.

Gao, X., Majumder, E.W., Kang, Y., Yue, H., and Blankenship, R.E. (2013). Functional analysis and expression of the mono-heme containing cytochrome *c* subunit of alternative complex III in *Chloroflexus aurantiacus*. *Archives of Biochemistry and Biophysics 535*, 197–204.

Garrity, G.M., Bell, J.A., and Lilburn, T.G. (2004). Taxonomic outline of the prokaryotes. Bergey's manual of systematic bacteriology. *Springer.*

Glaeser, R.M. (2016). Specimen behavior in the electron beam. *Methods in Enzymology 579*, 19–50.

Grad, L.I., and Lemire, B.D. (2006). Riboflavin enhances the assembly of mitochondrial cytochrome *c* oxidase in *C. elegans* NADH-ubiquinone oxidoreductase mutants. *Biochimica et Biophysica Acta 1757*, 115–122.

Gralla, J.D., and Vargas, D.R. (2006). Potassium glutamate as a transcriptional inhibitor during bacterial osmoregulation. *The EMBO Journal 25*, 1515–1521.

Grant, T., and Grigorieff, N. (2015a). Measuring the optimal exposure for single particle cryo-EM using a 2.6 Å reconstruction of rotavirus VP6. *ELife 4*, e06980.

Grant, T., and Grigorieff, N. (2015b). Automatic estimation and correction of anisotropic magnification distortion in electron microscopes. *Journal of Structural Biology 192*, 204–208.

Grant, T., Rohou, A., and Grigorieff, N. (2018). cisTEM, user-friendly software for single-particle image processing. *ELife 7*, e35383.

de Grotthuss, C.J.T. (2006). Memoir on the decomposition of water and of the bodies that it holds in solution by means of galvanic electricity. *Biochimica et Biophysica Acta 1757*, 871–875.

Guarás, A., Perales-Clemente, E., Calvo, E., Acín-Pérez, R., Loureiro-Lopez, M., Pujol, C., Martínez-Carrascoso, I., Nuñez, E., García-Marqués, F., Rodríguez-Hernández, M.A., et al. (2016). The coqh2/coq ratio serves as a sensor of respiratory chain efficiency. *Cell Reports 15*, 197–209.

Guerrero-Castillo, S., Baertling, F., Kownatzki, D., Wessels, H.J., Arnold, S., Brandt, U., and Nijtmans, L. (2017). The assembly pathway of mitochondrial respiratory chain complex I. *Cell Metabolism 25*, 128–139.

Gundlach, J., Herzberg, C., Kaever, V., Gunka, K., Hoffmann, T., Weiß, M., Gibhardt, J., Thürmer, A., Hertel, D., Daniel, R., et al. (2017). Control of potassium homeostasis is an essential function of the second messenger cyclic di-AMP in *Bacillus subtilis. Science Signaling 10*, eaal3011.

Guo, R., Zong, S., Wu, M., Gu, J., and Yang, M. (2017). Architecture of human mitochondrial respiratory megacomplex $I_2III_2IV_2$. *Cell 170*, 1247–1257.e12.

Hackenbrock, C.R., Chazotte, B., and Gupte, S.S. (1986). The random collision model and a critical assessment of diffusion and collision in mitochondrial electron transport. *Journal of Bioenergetics and Biomembranes 18*, 331–368.

Hägerhäll, C. (1997). Succinate: quinone oxidoreductases: variations on a conserved theme. *Biochimica et Biophysica Acta (BBA)-Bioenergetics 1320*, 107–141.

Haro, R., Sainz, L., Rubio, F., and Rodríguez-Navarro, A. (1999). Cloning of two genes encoding potassium transporters in *Neurospora crassa* and expression of the corresponding cDNAs in *Saccharomyces cerevisiae*. *Molecular Microbiology 31*, 511–520.

van Heel, M., and Frank, J. (1981). Use of multivariate statistics in analysing the images of biological macromolecules. *Ultramicroscopy 6*, 187–194.

Heinemeyer, J., Braun, H.P., Boekema, E.J., and Kouril, R. (2007). A structural model of the cytochrome *c* reductase/oxidase supercomplex from yeast mitochondria. *The Journal of Biological Chemistry 282*, 12240–12248.

Henderson, R. (2013). Avoiding the pitfalls of single particle cryo-electron microscopy: Einstein from noise. *Proceedings of the National Academy of Sciences of the United States of America 110*, 18037–18041.

Henderson, R., Baldwin, J.M., Ceska, T.A., Zemlin, F., Beckmann, E., and Downing, K.H. (1990). Model for the structure of bacteriorhodopsin based on high-resolution electron cryo-microscopy. *Journal of Molecular Biology 213*, 899–929.

Henderson, R., Chen, S., Chen, J.Z., Grigorieff, N., Passmore, L.A., Ciccarelli, L., Rubinstein, J.L., Crowther, R.A., Stewart, P.L., and Rosenthal, P.B. (2011). Tilt-pair analysis of images from a range of different specimens in single-particle electron cryomicroscopy. *Journal of Molecular Biology 413*, 1028–1046.

Herzik, M.A., Wu, M., and Lander, G.C. (2017). Achieving better-than-3-Å

resolution by single-particle cryo-EM at 200 keV. *Nature Methods 14*, 1075–1078.

Ho, B.K., and Gruswitz, F. (2008). HOLLOW: generating accurate representations of channel and interior surfaces in molecular structures. *BMC Structural Biology 8*, 49.

Horie, T., Yoshida, K., Nakayama, H., Yamada, K., Oiki, S., and Shinmyo, A. (2001). Two types of HKT transporters with different properties of Na$^+$ and K$^+$ transport in *Oryza sativa*. *The Plant Journal: For Cell and Molecular Biology 27*, 129–138.

Hovers, J., Potschies, M., Polidori, A., Pucci, B., Raynal, S., Bonneté, F., Serrano-Vega, M.J., Tate, C.G., Picot, D., Pierre, Y., et al. (2011). A class of mild surfactants that keep integral membrane proteins water-soluble for functional studies and crystallization. *Molecular Membrane Biology 28*, 171–181.

Hüttemann, M., Schmidt, T., and Grossman, L. (2003a). A third isoform of cytochrome *c* oxidase subunit VIII is present in mammals. *Gene 312*, 95–102.

Hüttemann, M., Jaradat, S., and Grossman, L.I. (2003b). Cytochrome *c* oxidase of mammals contains a testes-specific isoform of subunit VIb - the counterpart to testes-specific cytochrome *c*? *Molecular Reproduction and Development 66*, 8–16.

Iwasaki, T., Matsuura, K., and Oshima, T. (1995). Resolution of the aerobic respiratory system of the thermoacidophilic archaeon, *Sulfolobus* sp. strain 7. I. The archaeal terminal oxidase supercomplex is a functional fusion of respiratory complexes III and IV with no *c*-type cytochromes. *The Journal of Biological Chemistry 270*, 30881–30892.

Iwata, S., Lee, J.W., Okada, K., Lee, J.K., Iwata, M., Rasmussen, B., Link, T.A., Ramaswamy, S., and Jap, B.K. (1998). Complete structure of the 11-subunit bovine mitochondrial cytochrome bc_1 complex. *Science 281*, 64–71.

Jormakka, M., Yokoyama, K., Yano, T., Tamakoshi, M., Akimoto, S., Shimamura, T., Curmi, P., and Iwata, S. (2008). Molecular mechanism of energy conservation in polysulfide respiration. *Nature Structural & Molecular Biology 15*, 730–737.

Jungnickel, K.E.J., Parker, J.L., and Newstead, S. (2018). Structural basis for amino

acid transport by the CAT family of SLC7 transporters. *Nature Communications 9*, 550.

Kelley, L.A., Mezulis, S., Yates, C.M., Wass, M.N., and Sternberg, M.J.E. (2015). The Phyre2 web portal for protein modeling, prediction and analysis. *Nature Protocols 10*, 845–858.

Keshavan, N., and Rahman, S. (2018). Natural history of mitochondrial disorders: a systematic review. *Essays in Biochemistry 62*, 423–442.

Kim, H., Youn, S.J., Kim, S.O., Ko, J., Lee, J.O., and Choi, B.S. (2015). Structural studies of potassium transport protein KtrA regulator of conductance of K$^+$ (RCK) C domain in complex with cyclic diadenosine monophosphate (c-di-AMP). *The Journal of Biological Chemistry 290*, 16393–16402.

Kimanius, D., Forsberg, B.O., Scheres, S.H., and Lindahl, E. (2016). Accelerated cryo-EM structure determination with parallelisation using GPUs in RELION-2. *ELife 5*, e18722.

Konstantinov, A.A., Siletsky, S., Mitchell, D., Kaulen, A., and Gennis, R.B. (1997). The roles of the two proton input channels in cytochrome *c* oxidase from *Rhodobacter sphaeroides* probed by the effects of site-directed mutations on time-resolved electrogenic intraprotein proton transfer. *Proceedings of the National Academy of Sciences of the United States of America 94*, 9085–9090.

Krause, F., Reifschneider, N.H., Goto, S., and Dencher, N.A. (2005). Active oligomeric ATP synthases in mammalian mitochondria. *Biochemical and Biophysical Research Communications 329*, 583–590.

Krishnamurthy, H., Piscitelli, C.L., and Gouaux, E. (2009). Unlocking the molecular secrets of sodium-coupled transporters. *Nature 459*, 347–355.

Krivanek, O.L., and Mooney, P.E. (1993). Applications of slow-scan CCD cameras in transmission electron microscopy. *Ultramicroscopy 49*, 95–108.

Kröning, N., Willenborg, M., Tholema, N., Hänelt, I., Schmid, R., and Bakker, E.P. (2007). ATP binding to the KTN/RCK subunit KtrA from the K$^+$-uptake system

KtrAB of *Vibrio alginolyticus*: its role in the formation of the KtrAB complex and its requirement in vivo. *The Journal of Biological Chemistry 282*, 14018–14027.

Kucukelbir, A., Sigworth, F.J., and Tagare, H.D. (2014). Quantifying the local resolution of cryo-EM density maps. *Nature Methods 11*, 63–65.

Kühlbrandt, W., Wang, D.N., and Fujiyoshi, Y. (1994). Atomic model of plant light-harvesting complex by electron crystallography. *Nature 367*, 614–621.

Kuonen, D.R., Roberts, P.J., and Cottingham, I.R. (1986). Purification and analysis of mitochondrial membrane proteins on nondenaturing gradient polyacrylamide gels. *Analytical Biochemistry 153*, 221–226.

Lamantea, E., Carrara, F., Mariotti, C., Morandi, L., Tiranti, V., and Zeviani, M. (2002). A novel nonsense mutation (Q352X) in the mitochondrial cytochrome *b* gene associated with a combined deficiency of complexes I and III. *Neuromuscular Disorders 12*, 49–52.

Lanciano, P., Lee, D.W., Yang, H., Darrouzet, E., and Daldal, F. (2011). Intermonomer electron transfer between the low-potential *b* hemes of cytochrome bc_1. *Biochemistry 50*, 1651–1663.

Lapuente-Brun, E., Moreno-Loshuertos, R., Acín-Pérez, R., Latorre-Pellicer, A., Colás, C., Balsa, E., Perales-Clemente, E., Quirós, P.M., Calvo, E., Rodríguez-Hernández, M.A., et al. (2013). Supercomplex assembly determines electron flux in the mitochondrial electron transport chain. *Science 340*, 1567–1570.

Lazarou, M., McKenzie, M., Ohtake, A., Thorburn, D.R., and Ryan, M.T. (2007). Analysis of the assembly profiles for mitochondrial- and nuclear-DNA-encoded subunits into complex I. *Molecular and Cellular Biology 27*, 4228–4237.

Leif, H., Sled, V.D., Ohnishi, T., Weiss, H., and Friedrich, T. (1995). Isolation and characterization of the proton-translocating NADH: ubiquinone oxidoreductase from *Escherichia coli*. *European Journal of Biochemistry / FEBS 230*, 538–548.

Lenaz, G. (2012). Mitochondria and reactive oxygen species. Which role in physiology and pathology? *Advances in Experimental Medicine and Biology 942*,

93–136.

Lenaz, G., Tioli, G., Falasca, A.I., and Genova, M.L. (2016). Complex I function in mitochondrial supercomplexes. *Biochimica et Biophysica Acta 1857*, 991–1000.

Lenaz, G., Tioli, G., Falasca, A.I., and Genova, M.L. (2018). Coenzyme Q and respiratory supercomplexes: physiological and pathological implications. *Rendiconti Lincei 29*, 383–395.

Leschziner, A.E., and Nogales, E. (2006). The orthogonal tilt reconstruction method: an approach to generating single-class volumes with no missing cone for *ab initio* reconstruction of asymmetric particles. *Journal of Structural Biology 153*, 284–299.

Letts, J.A., Fiedorczuk, K., and Sazanov, L.A. (2016). The architecture of respiratory supercomplexes. *Nature 537*, 644–648.

Levin, E.J., and Zhou, M. (2014). Recent progress on the structure and function of the TrkH/KtrB ion channel. *Current Opinion in Structural Biology 27*, 95–101.

Li, X., Mooney, P., Zheng, S., Booth, C.R., Braunfeld, M.B., Gubbens, S., Agard, D.A., and Cheng, Y. (2013). Electron counting and beam-induced motion correction enable near-atomic-resolution single-particle cryo-EM. *Nature Methods 10*, 584–590.

Liao, M., Cao, E., Julius, D., and Cheng, Y. (2013). Structure of the TRPV1 ion channel determined by electron cryo-microscopy. *Nature 504*, 107–112.

Ludtke, S.J., Baldwin, P.R., and Chiu, W. (1999). EMAN: semiautomated software for high-resolution single-particle reconstructions. *Journal of Structural Biology 128*, 82–97.

Lyons, J.A., Aragão, D., Slattery, O., Pisliakov, A.V., Soulimane, T., and Caffrey, M. (2012). Structural insights into electron transfer in caa_3-type cytochrome oxidase. *Nature 487*, 514–518.

Majumder, E.L.W., King, J.D., and Blankenship, R.E. (2013). Alternative Complex

III from phototrophic bacteria and its electron acceptor auracyanin. *Biochimica et Biophysica Acta 1827*, 1383–1391.

Maranzana, E., Barbero, G., Falasca, A.I., Lenaz, G., and Genova, M.L. (2013). Mitochondrial respiratory supercomplex association limits production of reactive oxygen species from complex I. *Antioxidants & Redox Signaling 19*, 1469–1480.

Marreiros, B.C., Calisto, F., Castro, P.J., Duarte, A.M., Sena, F.V., Silva, A.F., Sousa, F.M., Teixeira, M., Refojo, P.N., and Pereira, M.M. (2016). Exploring membrane respiratory chains. *Biochimica et Biophysica Acta 1857*, 1039–1067.

Mäser, P., Hosoo, Y., Goshima, S., Horie, T., Eckelman, B., Yamada, K., Yoshida, K., Bakker, E.P., Shinmyo, A., Oiki, S., et al. (2002). Glycine residues in potassium channel-like selectivity filters determine potassium selectivity in four-loop-per-subunit HKT transporters from plants. *Proceedings of the National Academy of Sciences of the United States of America 99*, 6428–6433.

Matias, P.M., Morais, J., Coelho, A.V., Meijers, R., Gonzalez, A., Thompson, A.W., Sieker, L., LeGall, J., and Carrondo, M.A. (1997). A preliminary analysis of the three-dimensional structure of dimeric di-haem split-Soret cytochrome *c* from *Desulfovibrio desulfuricans* ATCC 27774 at 2.5-Å resolution using the MAD phasing method: a novel cytochrome fold with a stacked-haem arrangement. *Journal of Biological Inorganic Chemistry 2*, 507–514.

Matsuda, N., Kobayashi, H., Katoh, H., Ogawa, T., Futatsugi, L., Nakamura, T., Bakker, E.P., and Uozumi, N. (2004). Na^+-dependent K^+ uptake Ktr system from the cyanobacterium *Synechocystis* sp. PCC 6803 and its role in the early phases of cell adaptation to hyperosmotic shock. *The Journal of Biological Chemistry 279*, 54952–54962.

McLaggan, D., Jones, M.A., Gouesbet, G., Levina, N., Lindey, S., Epstein, W., and Booth, I.R. (2002). Analysis of the kefA2 mutation suggests that KefA is a cation-specific channel involved in osmotic adaptation in *Escherichia coli. Molecular Microbiology 43*, 521–536.

McMullan, G., Chen, S., Henderson, R., and Faruqi, A.R. (2009a). Detective quantum efficiency of electron area detectors in electron microscopy. *Ultramicroscopy 109*, 1126–1143.

McMullan, G., Faruqi, A.R., Henderson, R., Guerrini, N., Turchetta, R., Jacobs, A., and van Hoften, G. (2009b). Experimental observation of the improvement in MTF from backthinning a CMOS direct electron detector. *Ultramicroscopy 109*, 1144–1147.

McMullan, G., Faruqi, A.R., Clare, D., and Henderson, R. (2014). Comparison of optimal performance at 300keV of three direct electron detectors for use in low dose electron microscopy. *Ultramicroscopy 147*, 156–163.

McMullan, G., Faruqi, A.R., and Henderson, R. (2016). Direct Electron Detectors. *Methods in Enzymology 579*, 1–17.

Meunier, B., Fisher, N., Ransac, S., Mazat, J.P., and Brasseur, G. (2013). Respiratory complex III dysfunction in humans and the use of yeast as a model organism to study mitochondrial myopathy and associated diseases. *Biochimica et Biophysica Acta 1827*, 1346–1361.

Mileykovskaya, E., and Dowhan, W. (2014). Cardiolipin-dependent formation of mitochondrial respiratory supercomplexes. *Chemistry and Physics of Lipids 179*, 42–48.

Mills, D.J., Vitt, S., Strauss, M., Shima, S., and Vonck, J. (2013). *De novo* modeling of the F(420)-reducing [NiFe]-hydrogenase from a methanogenic archaeon by cryo-electron microscopy. *ELife 2*, e00218.

Mindell, J.A., and Grigorieff, N. (2003). Accurate determination of local defocus and specimen tilt in electron microscopy. *Journal of Structural Biology 142*, 334–347.

Mitchell, P. (1974). Chemiosmotic coupling in energy transduction: A logical development of biochemical knowledge. In Membrane Structure and Mechanisms of Biological Energy Transduction, J. Avery, ed. (Boston, MA:

Springer US), pp. 5–24.

Mitchell, P. (1976). Possible molecular mechanisms of the protonmotive function of cytochrome systems. *Journal of Theoretical Biology 62*, 327–367.

Moreira, L., Nobre, F.M., Sa-Correia, I., and Da Costa, M.S. (1996). Genomic typing and fatty acid composition of *Rhodothermus marinus*. *Systematic and Applied Microbiology 19*, 83–90.

Moreno-Lastres, D., Fontanesi, F., García-Consuegra, I., Martín, M.A., Arenas, J., Barrientos, A., and Ugalde, C. (2012). Mitochondrial complex I plays an essential role in human respirasome assembly. *Cell Metabolism 15*, 324–335.

Moriya, T., Saur, M., Stabrin, M., Merino, F., Voicu, H., Huang, Z., Penczek, P.A., Raunser, S., and Gatsogiannis, C. (2017). High-resolution single particle analysis from electron cryo-microscopy images using SPHIRE. *Journal of Visualized Experiments*.

Muramoto, K., Ohta, K., Shinzawa-Itoh, K., Kanda, K., Taniguchi, M., Nabekura, H., Yamashita, E., Tsukihara, T., and Yoshikawa, S. (2010). Bovine cytochrome *c* oxidase structures enable O_2 reduction with minimization of reactive oxygens and provide a proton-pumping gate. *Proceedings of the National Academy of Sciences of the United States of America 107*, 7740–7745.

Murata, K., Mitsuoka, K., Hirai, T., Walz, T., Agre, P., Heymann, J.B., Engel, A., and Fujiyoshi, Y. (2000). Structural determinants of water permeation through aquaporin-1. *Nature 407*, 599–605.

Nakane, T., Kimanius, D., Lindahl, E., and Scheres, S.H. (2018). Characterisation of molecular motions in cryo-EM single-particle data by multi-body refinement in RELION. *ELife 7*, e36861.

Nehls, U., Friedrich, T., Schmiede, A., Ohnishi, T., and Weiss, H. (1992). Characterization of assembly intermediates of NADH:ubiquinone oxidoreductase (complex I) accumulated in *Neurospora* mitochondria by gene disruption. *Journal of Molecular Biology 227*, 1032–1042.

Nirody, J.A., Sun, Y.-R., and Lo, C.-J. (2017). The biophysicist's guide to the bacterial flagellar motor. *Advances in Physics: X 2*, 324–343.

Noble, A.J., Wei, H., Dandey, V.P., Zhang, Z., Tan, Y.Z., Potter, C.S., and Carragher, B. (2018). Reducing effects of particle adsorption to the air-water interface in cryo-EM. *Nature Methods 15*, 793–795.

Nogales, E., Wolf, S.G., and Downing, K.H. (1998). Correction: Structure of the αβ tubulin dimer by electron crystallography. *Nature 393*, 191.

Nunes, O.C., Donato, M.M., and Da Costa, M.S. (1992). Isolation and characterization of *Rhodothermus* strains from S. Miguel, Azores. *Systematic and Applied Microbiology 15*, 92–97.

Ohi, M., Li, Y., Cheng, Y., and Walz, T. (2004). Negative staining and image classification - powerful tools in modern electron microscopy. *Biological Procedures Online 6*, 23–34.

Orlova, E.V., and Saibil, H.R. (2011). Structural analysis of macromolecular assemblies by electron microscopy. *Chemical Reviews 111*, 7710–7748.

Parsons, W.J., Williams, R.S., Shelton, J.M., Luo, Y., Kessler, D.J., and Richardson, J.A. (1996). Developmental regulation of cytochrome oxidase subunit VIa isoforms in cardiac and skeletal muscle. *The American Journal of Physiology 270*, H567-74.

Passmore, L.A., and Russo, C.J. (2016). Specimen preparation for high-resolution cryo-EM. *Methods in Enzymology 579*, 51–86.

Penczek, P.A. (2010a). Single-particle reconstruction.

Penczek, P.A. (2010b). Resolution measures in molecular electron microscopy. In Cryo-EM, Part B: 3-D Reconstruction, (Elsevier), pp. 73–100.

Pereira, M.M., Antunes, A.M., Nunes, O.C., da Costa, M.S., and Teixeira, M. (1994). A membrane-bound HIPIP type center in the thermohalophile *Rhodothermus marinus*. *FEBS Letters 352*, 327–330.

Pereira, M.M., Carita, J.N., and Teixeira, M. (1999a). Membrane-bound electron transfer chain of the thermohalophilic bacterium *Rhodothermus marinus*: a novel multihemic cytochrome *bc*, a new complex III. *Biochemistry 38*, 1268–1275.

Pereira, M.M., Carita, J.N., and Teixeira, M. (1999b). Membrane-bound electron transfer chain of the thermohalophilic bacterium *Rhodothermus marinus*: characterization of the iron-sulfur centers from the dehydrogenases and investigation of the high-potential iron-sulfur protein function by *in vitro* reconstitution of the respiratory chain. *Biochemistry 38*, 1276–1283.

Pereira, M.M., Santana, M., Soares, C.M., Mendes, J., Carita, J.N., Fernandes, A.S., Saraste, M., Carrondo, M.A., and Teixeira, M. (1999c). The caa_3 terminal oxidase of the thermohalophilic bacterium *Rhodothermus marinus*: a HiPIP:oxygen oxidoreductase lacking the key glutamate of the D-channel. *Biochimica et Biophysica Acta (BBA) - Bioenergetics 1413*, 1–13.

Pereira, M.M., Carita, J.N., Anglin, R., and Saraste, M. (2000a). Heme centers of *Rhodothermus marinus* respiratory chain. Characterization of its cbb_3 oxidase. *Journal of Bioenergetics and Biomembranes 32*, 143–152.

Pereira, M.M., Verkhovskaya, M.L., Teixeira, M., and Verkhovsky, M.I. (2000b). The caa_3 terminal oxidase of *Rhodothermus marinus* lacking the key glutamate of the D-channel is a proton pump. *Biochemistry 39*, 6336–6340.

Pereira, M.M., Refojo, P.N., Hreggvidsson, G.O., Hjorleifsdottir, S., and Teixeira, M. (2007). The alternative complex III from *Rhodothermus marinus* - a prototype of a new family of quinol:electron acceptor oxidoreductases. *FEBS Letters 581*, 4831–4835.

Pettersen, E.F., Goddard, T.D., Huang, C.C., Couch, G.S., Greenblatt, D.M., Meng, E.C., and Ferrin, T.E. (2004). UCSF Chimera—a visualization system for exploratory research and analysis. *Journal of Computational Chemistry 25*, 1605–1612.

Poole, R.K., and Cook, G.M. (2000). Redundancy of aerobic respiratory chains in bacteria? Routes, reasons and regulation. *Advances in Microbial Physiology 43*,

165–224.

Prince, W.S., and Villarejo, M.R. (1990). Osmotic control of proU transcription is mediated through direct action of potassium glutamate on the transcription complex. *The Journal of Biological Chemistry 265*, 17673–17679.

Punjani, A., Rubinstein, J.L., Fleet, D.J., and Brubaker, M.A. (2017). cryoSPARC: algorithms for rapid unsupervised cryo-EM structure determination. *Nature Methods 14*, 290–296.

Radermacher, M., Wagenknecht, T., Verschoor, A., and Frank, J. (1987). Three-dimensional reconstruction from a single-exposure, random conical tilt series applied to the 50S ribosomal subunit of *Escherichia coli. Journal of Microscopy 146*, 113–136.

Rak, M., Bénit, P., Chrétien, D., Bouchereau, J., Schiff, M., El-Khoury, R., Tzagoloff, A., and Rustin, P. (2016). Mitochondrial cytochrome *c* oxidase deficiency. *Clinical Science 130*, 393–407.

Razinkov, I., Dandey, V., Wei, H., Zhang, Z., Melnekoff, D., Rice, W.J., Wigge, C., Potter, C.S., and Carragher, B. (2016). A new method for vitrifying samples for cryoEM. *Journal of Structural Biology 195*, 190–198.

Refojo, P.N., Teixeira, M., and Pereira, M.M. (2010a). The alternative complex III of *Rhodothermus marinus* and its structural and functional association with caa_3 oxygen reductase. *Biochimica et Biophysica Acta 1797*, 1477–1482.

Refojo, P.N., Sousa, F.L., Teixeira, M., and Pereira, M.M. (2010b). The alternative complex III: a different architecture using known building modules. *Biochimica et Biophysica Acta 1797*, 1869–1876.

Refojo, P.N., Teixeira, M., and Pereira, M.M. (2012). The Alternative complex III: properties and possible mechanisms for electron transfer and energy conservation. *Biochimica et Biophysica Acta 1817*, 1852–1859.

Refojo, P.N., Calisto, F., Ribeiro, M.A., Teixeira, M., and Pereira, M.M. (2017). The monoheme cytochrome *c* subunit of Alternative Complex III is a direct electron

donor to *caa*$_3$ oxygen reductase in *Rhodothermus marinus. Biological Chemistry 398*, 1037–1044.

Rhoads, D.B., and Epstein, W. (1977). Energy coupling to net K$^+$ transport in *Escherichia coli* K-12. *The Journal of Biological Chemistry 252*, 1394–1401.

Rich, P.R., and Maréchal, A. (2013). Functions of the hydrophilic channels in protonmotive cytochrome *c* oxidase. *Journal of the Royal Society, Interface 10*, 20130183.

Rodenburg, R.J. (2016). Mitochondrial complex I-linked disease. *Biochimica et Biophysica Acta 1857*, 938–945.

Rohou, A., and Grigorieff, N. (2015). CTFFIND4: Fast and accurate defocus estimation from electron micrographs. *Journal of Structural Biology 192*, 216–221.

Rosenthal, P.B., and Henderson, R. (2003). Optimal determination of particle orientation, absolute hand, and contrast loss in single-particle electron cryomicroscopy. *Journal of Molecular Biology 333*, 721–745.

Ruska, E. (1987). The development of the electron microscope and of electron microscopy. *Reviews of Modern Physics 59*, 627–638.

Russo, C.J., and Passmore, L.A. (2014). Electron microscopy: Ultrastable gold substrates for electron cryomicroscopy. *Science 346*, 1377–1380.

Santa-María, G.E., Oliferuk, S., and Moriconi, J.I. (2018). KT-HAK-KUP transporters in major terrestrial photosynthetic organisms: A twenty years tale. *Journal of Plant Physiology 226*, 77–90.

Sato, Y., Nanatani, K., Hamamoto, S., Shimizu, M., Takahashi, M., Tabuchi-Kobayashi, M., Mizutani, A., Schroeder, J.I., Souma, S., and Uozumi, N. (2014). Defining membrane spanning domains and crucial membrane-localized acidic amino acid residues for K$^+$ transport of a Kup/HAK/KT-type *Escherichia coli* potassium transporter. *Journal of Biochemistry 155*, 315–323.

Sazanov, L.A., and Hinchliffe, P. (2006). Structure of the hydrophilic domain of respiratory complex I from *Thermus thermophilus*. *Science 311*, 1430–1436.

Schäfer, E., Seelert, H., Reifschneider, N.H., Krause, F., Dencher, N.A., and Vonck, J. (2006). Architecture of active mammalian respiratory chain supercomplexes. *The Journal of Biological Chemistry 281*, 15370–15375.

Schäfer, E., Dencher, N.A., Vonck, J., and Parcej, D.N. (2007). Three-dimensional structure of the respiratory chain supercomplex $I_1III_2IV_1$ from bovine heart mitochondria. *Biochemistry 46*, 12579–12585.

Schägger, H., and Pfeiffer, K. (2000). Supercomplexes in the respiratory chains of yeast and mammalian mitochondria. *The EMBO Journal 19*, 1777–1783.

Schägger, H., and Pfeiffer, K. (2001). The ratio of oxidative phosphorylation complexes I-V in bovine heart mitochondria and the composition of respiratory chain supercomplexes. *The Journal of Biological Chemistry 276*, 37861–37867.

Schägger, H., Link, T.A., Engel, W.D., and von Jagow, G. (1986). Isolation of the eleven protein subunits of the bc_1 complex from beef heart. *Methods in Enzymology 126*, 224–237.

Schägger, H., de Coo, R., Bauer, M.F., Hofmann, S., Godinot, C., and Brandt, U. (2004). Significance of respirasomes for the assembly/stability of human respiratory chain complex I. *The Journal of Biological Chemistry 279*, 36349–36353.

Scheres, S.H. (2014). Beam-induced motion correction for sub-megadalton cryo-EM particles. *ELife 3*, e03665.

Scheres, S.H.W. (2012). RELION: implementation of a Bayesian approach to cryo-EM structure determination. *Journal of Structural Biology 180*, 519–530.

Scheres, S.H.W. (2015). Semi-automated selection of cryo-EM particles in RELION-1.3. *Journal of Structural Biology 189*, 114–122.

Scheres, S.H.W. (2016). Processing of structurally heterogeneous cryo-EM data in

RELION. *Methods in Enzymology 579*, 125–157.

Schlerf, A., Droste, M., Winter, M., and Kadenbach, B. (1988). Characterization of two different genes (cDNA) for cytochrome *c* oxidase subunit VIa from heart and liver of the rat. *The EMBO Journal 7*, 2387–2391.

Schrempf, H., Schmidt, O., Kümmerlen, R., Hinnah, S., Müller, D., Betzler, M., Steinkamp, T., and Wagner, R. (1995). A prokaryotic potassium ion channel with two predicted transmembrane segments from *Streptomyces lividans*. *The EMBO Journal 14*, 5170–5178.

Screpanti, E., and Hunte, C. (2007). Discontinuous membrane helices in transport proteins and their correlation with function. *Journal of Structural Biology 159*, 261–267.

Shepherd, M., and Poole, R.K. (2013). Bacterial respiratory chains. *Encyclopedia of Biophysics*.

Shi, Y. (2013). Common folds and transport mechanisms of secondary active transporters. *Annual Review of Biophysics 42*, 51–72.

Silva, Z., Horta, C., da Costa, M.S., Chung, A.P., and Rainey, F.A. (2000). Polyphasic evidence for the reclassification of *Rhodothermus obamensis* Sako et al. 1996 as a member of the species *Rhodothermus marinus* Alfredsson et al. 1988. *International Journal of Systematic and Evolutionary Microbiology 50*, 1457–1461.

Smart, O.S., Neduvelil, J.G., Wang, X., Wallace, B.A., and Sansom, M.S. (1996). HOLE: a program for the analysis of the pore dimensions of ion channel structural models. *Journal of Molecular Graphics 14*, 354–360, 376.

Sousa, J.S., D'Imprima, E., and Vonck, J. (2018a). Mitochondrial respiratory chain complexes. *Sub-Cellular Biochemistry 87*, 167–227.

Sousa, J.S., Calisto, F., Langer, J.D., Mills, D.J., Refojo, P.N., Teixeira, M., Kühlbrandt, W., Vonck, J., and Pereira, M.M. (2018b). Structural basis for energy transduction by respiratory alternative complex III. *Nature Communications 9*, 1728.

Srinivasan, V., Rajendran, C., Sousa, F.L., Melo, A.M.P., Saraiva, L.M., Pereira, M.M., Santana, M., Teixeira, M., and Michel, H. (2005). Structure at 1.3 Å resolution of *Rhodothermus marinus caa*$_3$ cytochrome *c* domain. *Journal of Molecular Biology 345*, 1047–1057.

Stark, H., Zemlin, F., and Boettcher, C. (1996). Electron radiation damage to protein crystals of bacteriorhodopsin at different temperatures. *Ultramicroscopy 63*, 75–79.

Stelter, M., Melo, A.M.P., Pereira, M.M., Gomes, C.M., Hreggvidsson, G.O., Hjorleifsdottir, S., Saraiva, L.M., Teixeira, M., and Archer, M. (2008). A novel type of monoheme cytochrome *c*: biochemical and structural characterization at 1.23 Å resolution of *Rhodothermus marinus* cytochrome *c*. *Biochemistry 47*, 11953–11963.

Strauss, M., Hofhaus, G., Schröder, R.R., and Kühlbrandt, W. (2008). Dimer ribbons of ATP synthase shape the inner mitochondrial membrane. *The EMBO Journal 27*, 1154–1160.

Suelter, C.H. (1970). Enzymes activated by monovalent cations. *Science 168*, 789–795.

Sun, C., Benlekbir, S., Venkatakrishnan, P., Wang, Y., Hong, S., Hosler, J., Tajkhorshid, E., Rubinstein, J.L., and Gennis, R.B. (2018). Structure of the alternative complex III in a supercomplex with cytochrome oxidase. *Nature 557*, 123–126.

Suomalainen, A., and Battersby, B.J. (2018). Mitochondrial diseases: the contribution of organelle stress responses to pathology. *Nature Reviews. Molecular Cell Biology 19*, 77–92.

Tan, Y.Z., Baldwin, P.R., Davis, J.H., Williamson, J.R., Potter, C.S., Carragher, B., and Lyumkis, D. (2017). Addressing preferred specimen orientation in single-particle cryo-EM through tilting. *Nature Methods 14*, 793–796.

Tang, G., Peng, L., Baldwin, P.R., Mann, D.S., Jiang, W., Rees, I., and Ludtke, S.J.

(2007). EMAN2: an extensible image processing suite for electron microscopy. *Journal of Structural Biology 157*, 38–46.

Tholema, N., Bakker, E.P., Suzuki, A., and Nakamura, T. (1999). Change to alanine of one out of four selectivity filter glycines in KtrB causes a two orders of magnitude decrease in the affinities for both K$^+$ and Na$^+$ of the Na$^+$-dependent K$^+$ uptake system KtrAB from *Vibrio alginolyticus. FEBS Letters 450*, 217–220.

Tholema, N., Vor der Brüggen, M., Mäser, P., Nakamura, T., Schroeder, J.I., Kobayashi, H., Uozumi, N., and Bakker, E.P. (2005). All four putative selectivity filter glycine residues in KtrB are essential for high affinity and selective K$^+$ uptake by the KtrAB system from *Vibrio alginolyticus. The Journal of Biological Chemistry 280*, 41146–41154.

Thompson, A.N., and Nimigean, C.M. (2013). Potassium Channel Diversity, Regulation of Potassium Flux across Pores. In Encyclopedia of Metalloproteins, R.H. Kretsinger, V.N. Uversky, and E.A. Permyakov, eds. (New York, NY: Springer New York), pp. 1781–1785.

Tindall, B.J. (1991). Lipid composition of *Rhodothermus marinus. FEMS Microbiology Letters 80*, 65–68.

Trumpower, B.L. (1990). Cytochrome *bc*$_1$ complexes of microorganisms. *Microbiological Reviews 54*, 101–129.

Tsukihara, T., Aoyama, H., Yamashita, E., Tomizaki, T., Yamaguchi, H., Shinzawa-Itoh, K., Nakashima, R., Yaono, R., and Yoshikawa, S. (1996). The whole structure of the 13-subunit oxidized cytochrome *c* oxidase at 2.8 Å. *Science 272*, 1136–1144.

Unwin, P.N., and Henderson, R. (1975). Molecular structure determination by electron microscopy of unstained crystalline specimens. *Journal of Molecular Biology 94*, 425–440.

Van Heel, M. (1987). Angular reconstitution: a posteriori assignment of projection directions for 3D reconstruction. *Ultramicroscopy 21*, 111–123.

Varanasi, L., and Hosler, J.P. (2012). Subunit III-depleted cytochrome *c* oxidase provides insight into the process of proton uptake by proteins. *Biochimica et Biophysica Acta 1817*, 545–551.

Vastermark, A., Wollwage, S., Houle, M.E., Rio, R., and Saier, M.H. (2014). Expansion of the APC superfamily of secondary carriers. *Proteins 82*, 2797–2811.

Vempati, U.D., Han, X., and Moraes, C.T. (2009). Lack of cytochrome *c* in mouse fibroblasts disrupts assembly/stability of respiratory complexes I and IV. *The Journal of Biological Chemistry 284*, 4383–4391.

Venceslau, S.S., Lino, R.R., and Pereira, I.A.C. (2010). The Qrc membrane complex, related to the alternative complex III, is a menaquinone reductase involved in sulfate respiration. *The Journal of Biological Chemistry 285*, 22774–22783.

Veríssimo, A.F., Pereira, M.M., Melo, A.M.P., Hreggvidsson, G.O., Kristjansson, J.K., and Teixeira, M. (2007). A ba_3 oxygen reductase from the thermohalophilic bacterium *Rhodothermus marinus*. *FEMS Microbiology Letters 269*, 41–47.

Vinothkumar, K.R., Zhu, J., and Hirst, J. (2014). Architecture of mammalian respiratory complex I. *Nature 515*, 80–84.

Voss, N.R., Yoshioka, C.K., Radermacher, M., Potter, C.S., and Carragher, B. (2009). DoG Picker and TiltPicker: software tools to facilitate particle selection in single particle electron microscopy. *Journal of Structural Biology 166*, 205–213.

Vukotic, M., Oeljeklaus, S., Wiese, S., Vögtle, F.N., Meisinger, C., Meyer, H.E., Zieseniss, A., Katschinski, D.M., Jans, D.C., Jakobs, S., et al. (2012). Rcf1 mediates cytochrome oxidase assembly and respirasome formation, revealing heterogeneity of the enzyme complex. *Cell Metabolism 15*, 336–347.

Wagner, T., Merino, F., Stabrin, M., Moriya, T., Gatsogiannis, C., and Raunser, S. (2018). SPHIRE-crYOLO: A fast and well-centering automated particle picker for cryo-EM. *BioRxiv*.

Walker, J.E. (1992). The NADH:ubiquinone oxidoreductase (complex I) of respiratory chains. *Quarterly Reviews of Biophysics 25*, 253–324.

Wang, L.J., and Zhou, Z.H. (2014). Seeing molecular interactions of large complexes by cryo electron microscopy at atomic resolution. *AMERICAN LABORATORY*.

Wikstrom, M.K. (1977). Proton pump coupled to cytochrome *c* oxidase in mitochondria. *Nature 266*, 271–273.

Wikström, M., Sharma, V., Kaila, V.R.I., Hosler, J.P., and Hummer, G. (2015). New perspectives on proton pumping in cellular respiration. *Chemical Reviews 115*, 2196–2221.

Williams, C.J., Headd, J.J., Moriarty, N.W., Prisant, M.G., Videau, L.L., Deis, L.N., Verma, V., Keedy, D.A., Hintze, B.J., Chen, V.B., et al. (2018). MolProbity: More and better reference data for improved all-atom structure validation. *Protein Science 27*, 293–315.

Wittig, I., Braun, H.-P., and Schägger, H. (2006). Blue native PAGE. *Nature Protocols 1*, 418–428.

Wu, M., Gu, J., Guo, R., Huang, Y., and Yang, M. (2016). Structure of mammalian respiratory supercomplex $I_1III_2IV_1$. *Cell 167*, 1598–1609.e10.

Xia, D., Yu, C.A., Kim, H., Xia, J.Z., Kachurin, A.M., Zhang, L., Yu, L., and Deisenhofer, J. (1997). Crystal structure of the cytochrome bc_1 complex from bovine heart mitochondria. *Science 277*, 60–66.

Yang, X.H., and Trumpower, B.L. (1986). Purification of a three-subunit ubiquinol-cytochrome *c* oxidoreductase complex from *Paracoccus denitrificans*. *The Journal of Biological Chemistry 261*, 12282–12289.

Yang, W.L., Iacono, L., Tang, W.M., and Chin, K.V. (1998). Novel function of the regulatory subunit of protein kinase A: regulation of cytochrome *c* oxidase activity and cytochrome *c* release. *Biochemistry 37*, 14175–14180.

Yang, Z., Fang, J., Chittuluru, J., Asturias, F.J., and Penczek, P.A. (2012). Iterative stable alignment and clustering of 2D transmission electron microscope images. *Structure 20*, 237–247.

Yanyushin, M.F. (2002). Fractionation of cytochromes of phototrophically grown *Chloroflexus aurantiacus*. Is there a cytochrome *bc* complex among them? *FEBS Letters 512*, 125–128.

Yanyushin, M.F., del Rosario, M.C., Brune, D.C., and Blankenship, R.E. (2005). New class of bacterial membrane oxidoreductases. *Biochemistry 44*, 10037–10045.

Yu, G., Li, K., Liu, Y., Chen, Z., Wang, Z., Yan, R., Klose, T., Tang, L., and Jiang, W. (2016). An algorithm for estimation and correction of anisotropic magnification distortion of cryo-EM images without need of pre-calibration. *Journal of Structural Biology 195*, 207–215.

Zakharyan, E., and Trchounian, A. (2001). K^+ influx by Kup in *Escherichia coli* is accompanied by a decrease in H^+ efflux. *FEMS Microbiology Letters 204*, 61–64.

Zara, V., Conte, L., and Trumpower, B.L. (2007). Identification and characterization of cytochrome bc_1 subcomplexes in mitochondria from yeast with single and double deletions of genes encoding cytochrome bc_1 subunits. *The FEBS Journal 274*, 4526–4539.

Zhang, K. (2016). Gctf: Real-time CTF determination and correction. *Journal of Structural Biology 193*, 1–12.

Zhang, X., and Zhou, Z.H. (2011). Limiting factors in atomic resolution cryo electron microscopy: no simple tricks. *Journal of Structural Biology 175*, 253–263.

Zhang, C., Cantara, W., Jeon, Y., Musier-Forsyth, K., Grigorieff, N., and Lyumkis, D. (2018). Analysis of discrete local variability and structural covariance in macromolecular assemblies using Cryo-EM and focused classification. *Ultramicroscopy*.

Zheng, S., Palovcak, E., Armache, J.-P., Cheng, Y., and Agard, D. (2016). Anisotropic correction of beam-induced motion for improved single-particle electron cryo-microscopy. *BioRxiv* 061960.

Zhou, M., Li, Y., Hu, Q., Bai, X.-C., Huang, W., Yan, C., Scheres, S.H.W., and Shi, Y.

(2015). Atomic structure of the apoptosome: mechanism of cytochrome *c*- and dATP-mediated activation of Apaf-1. *Genes & Development 29*, 2349–2361.

Zhu, J., Vinothkumar, K.R., and Hirst, J. (2016). Structure of mammalian respiratory complex I. *Nature 536*, 354–358.

Zivanov, J., Nakane, T., Forsberg, B.O., Kimanius, D., Hagen, W.J., Lindahl, E., and Scheres, S.H. (2018). New tools for automated high-resolution cryo-EM structure determination in RELION-3. *ELife 7*.

Zulkifli, L., Akai, M., Yoshikawa, A., Shimojima, M., Ohta, H., Guy, H.R., and Uozumi, N. (2010). The KtrA and KtrE subunits are required for Na^+-dependent K^+ uptake by KtrB across the plasma membrane in *Synechocystis* sp. strain PCC 6803. *Journal of Bacteriology 192*, 5063–5070.

IV. Declaration of scientific collaborations

Except where stated otherwise by reference or acknowledgment, the work presented was generated by myself under the supervision of my advisors during my doctoral studies. All contributions from colleagues are explicitly referenced in the thesis. The material listed below was obtained in the context of collaborative research.

Figure 34. Peptide mass fingerprinting was performed by Dr. Julian D. Langer from the Department of Molecular Membrane Biology, at the Max Planck Institute of Biophysics.

Figure 40. ITC experiments were performed by Filipa Calisto from the group of Dr. Manuela Pereira, at ITQB Universidade Nova de Lisboa.

Figure 43. Peptide mass fingerprinting was performed by Dr. Julian D. Langer, from the Department of Molecular Membrane Biology, at the Max Planck Institute of Biophysics. Identification and modeling of ActH was performed by Dr. Janet Vonck from the Department of Structural Biology, at the Max Planck Institute of Biophysics.

Figure 55. Pore calculations were performed by Dr. Igor Tascón from the group of Dr. Inga Hänelt, at the Institute of Biochemistry, Biocenter, Goethe University Frankfurt.

Figure 57. Transport assays were performed by Dr. Igor Tascón from the group of Dr. Inga Hänelt, at the Institute of Biochemistry, Biocenter, Goethe University Frankfurt.

Appendices A, B and C. Sequence alignments were performed by Filipa Calisto and Dr. Patrícia N. Refojo from the group of Dr. Manuela Pereira, at ITQB Universidade Nova de Lisboa.

Whenever a figure, table or text is identical to a previous publication, it is stated explicitly in the thesis that copyright permission and/or co-author agreement has been obtained.

The following parts of the thesis have been previously published:

Figures 20b, 21, 22, 23, 24, 25, 32, 33, 34, 35, 36, 37, 38, 39, 40, 41, 42, 43, 44, 45.

V. Acknowledgements

I want to take this opportunity to express my gratitude to everyone that supported me during my doctoral studies.

First and foremost, I would like to thank Werner Kühlbrandt for the privilege of working in his department and for his continuous support of my research. I am grateful for all the insightful comments, the stimulating atmosphere and the outstanding resources he has put in place, without which this work would not have been possible.

I am sincerely grateful to Janet Vonck for her generosity as a supervisor. Her guidance, motivation and immense knowledge were fundamental for my growth as a scientist. Thank you for consistently allowing me to find my way in this work while steering me in the right direction. I could not imagine having a better mentor during these years.

I would also like to thank Deryck Mills for all his help with the microscopes. And thank you for the contagious joy that you share with everyone.

I am grateful to Natalie Bärland, Filipa Calisto, Manuela Pereira, Igor Tascón and Inga Hänelt, with whom I had the pleasure to work during my doctorate and that contributed to the success of these projects.

I also want to thank Thomas Ellinghaus for his help with the translation to German of the summary in this thesis.

Finally, I want to thank my boyfriend Matteo for all his encouragement, kindness and support in the good and bad days, and to my family for their support at every step of the way that lead me to this moment.

VI. *Curriculum vitae*

Personal information

First name(s) / Surname(s)	**Joana Sofia de Sousa Simões**
Address(es)	Eschersheimer Landstraße 218
	60320 Frankfurt am Main
	Germany
Telephone(s)	+351 96 753 95 92, +49 (0) 1515 8365 467
E-mail	jsosusa@gmail.com, joana.sousa@biophys.mpg.de
Nationality	Portuguese
Date of birth	22.09.1988
Gender	Female

Work experience

Dates	From October 2014
Occupation or position held	PhD student at the department of Structural Biology, Max Planck Institute of Biophysics
Main activities and responsibilities	Structural investigation of membrane proteins by single-particle cryo-EM
Name and address of employer	Structural Biology - MPI of Biophysics, Max-von-Laue-Straße 3, 60438 Frankfurt am Main, Germany
Dates	From April 2013 to September 2014
Occupation or position held	Junior researcher for the project ITRANS from the Marie Curie Actions FP7-PEOPLE-2012-CIG
Main activities and responsibilities	Study of the NuoL subunit of Complex I of the respiratory chain and of the dynamics behind ion transport (of H^+ and Na^+)
Name and address of employer	Biological Energy Transduction - Metalloproteins and Bioenergetics Unit, Instituto de Tecnologia Química e Biológica António Xavier, Universidade Nova de Lisboa Av. da República, Estação Agronómica Nacional 2780-157 Oeiras, Portugal
Dates	From December 2011 to August 2012
Occupation or position held	IEFP Professional Internship
Main activities and responsibilities	Discover of the molecular and cellular mechanisms by which low-dose IR induces angiogenesis (*in vitro* and *in vivo*) and validation of these results in material from patients with rectal cancer that received preoperative radiotherapy
Name and address of employer	Angiogenesis Unit, Instituto de Medicina Molecular, Universidade de Lisboa Av. Prof. Egas Moniz-Edifício Egas Moniz -1649-028 Lisboa, Portugal

Education and training

Dates	September 2017
Title of qualification awarded	**EMBO practical course – Image processing for cryo-electron microscopy**

Name and type of organisation providing education and training	Birkbeck - University of London, London, UK
Dates	October 2015
Title of qualification awarded	**Workshop on single-particle reconstruction, structural variability and modelling**
Name and type of organisation providing education and training	National Center for Macromolecular Imaging, Houston, TX
Dates	July 2014
Title of qualification awarded	First Certificate in English
Name and type of organisation providing education and training	Cambridge University, UK
Level in national or international classification	A
Dates	November 2013
Title of qualification awarded	MembStruct2013
Principal subjects/occupational skills covered	Structure and Function of Membrane Proteins (NMR, X-ray crystallography, Mass spectrometry, Electron microscopy)
Name and type of organisation providing education and training	ITQB, Portugal
Dates	July 2013
Title of qualification awarded	**Certificate in Mathematics** (30 ECTS)
Principal subjects/occupational skills covered	Mathematics and modeling Calculus Probability and statistics
Name and type of organisation providing education and training	The Open University, UK
Dates	April 2011
Title of qualification awarded	Laboratory animal science (according to FELASA cat.B)
Principal subjects/occupational skills covered	Legislation, ethics and the 3R's Biology and husbandry of laboratory rodents and fish Animal health, welfare and scientific integrity Anesthesia, analgesia and basic principles of surgery Pratical sessions, rodents and fish
Name and type of organisation providing education and training	Instituto de Medicina Molecular, Universidade de Lisboa

Dates	2011 to 2014
Title of qualification awarded	Mathematics courses (The story of maths – 5 ECTS, Pure mathematics – 30 ECTS, Applications of probability – 15 ECTS, Introducing statistics – 15 ECTS)
Name and type of organisation	The Open University, UK
Dates	2009-2011
Title of qualification awarded	**MSc in Medical Biochemistry**
Principal subjects/occupational skills covered	Molecular biophysics Biomolecules structure and function Biochemical systems regulation Molecular biotechnology
Name and type of organisation providing education and training	Faculdade de Ciências da Universidade de Lisboa Campo Grande, Edifício C5 1749-016 Lisboa
Level in national or international classification	**18 (in 20)** (Thesis title: *Molecular Mechanisms and relevance of angiogenesis induced by low-dose ionizing radiation*; **Thesis grade: 20 (in 20)**)
Dates	2006-2009
Title of qualification awarded	**Degree in Biochemistry**
Principal subjects/occupational skills covered	Biochemistry I and II Biochemical regulation Cellular biology Molecular genetics Enzymology Physiology Immunology
Name and type of organisation providing education and training	Faculdade de Ciências da Universidade de Lisboa Campo Grande, Edifício C5 1749-016 Lisboa
Level in national or international classification	**15 (in 20)**

Personal skills and competences

Mother tongue(s)	Portuguese
Other language(s)	

Self-assessment	Understanding		Speaking		Writing
European level (*)	Listening	Reading	Spoken interaction	Spoken production	
English	C1 Proficient user	C1 Proficient user	C1 Proficient user	C1 Proficient user	C1 Proficient user

(*) [Common European Framework of Reference for Languages](#)

Social skills and competences	Team spirit acquired in the involvement in extra-curricular activities. Ability to adapt to different situations and groups acquired throughout the academic / vocational course. Good communication skills gained in curricular and extra-curricular context.

Technical skills and competences	Experience in cell culture (endothelial cells), in the *E.coli* protein expression system, with animal models (zebrafish). Knowledge and troubleshooting skills in: design of protein constructs, techniques of molecular biology (qRT-PCR, western-blot, immunohisto/cytochemistry, DNA gels, among others), fluorescence microscopy, purification of membrane proteins. General knowledge in bioinformatics tools (ExPasy, UniProt, BLAST). Experience in negative-staining and single-particle cryo-electron microscopy, from sample preparation, microscope alignment and data acquisition (Tecnai spirit, Tecnai Polara, Titan krios) to image processing (Relion, cisTEM, Sphire, cryoSPARC, EMAN2, IMAGIC, Gautomatch, ctffind, GCTF, MotionCor, Unblur, LocScale, ResMap) and *de novo* model building and refinement (coot, Phenix). Knowledge in molecular visualization software (PyMol, Chimera).
Computer skills and competences	Advanced user in Office applications (word processor, spreadsheets, presentations). Knowledge in the use of image editing software (Photoshop, ImageJ). Experience on Linux operating system and use of computing clusters by queuing systems (Slurm).
Driving licence	Category B
Additional information	Publications: - Joana S. Sousa and Janet Vonck. *Respiratory supercomplexes III$_2$IV$_2$ come into focus*. Nature structural & molecular biology (2019): 1. - Joana S. Sousa, Filipa Calisto, Julian D. Langer, Deryck J. Mills, Patrícia N. Refojo, Miguel Teixeira, Werner Kühlbrandt, Janet Vonck, and Manuela M. Pereira. *Structural basis for energy transduction by respiratory alternative complex III*. Nature communications 9 (2018). - Joana S. Sousa, Edoardo D'Imprima and Janet Vonck. *Mitochondrial respiratory chain complexes – Membrane Protein Complexes: Structure and Function*. Springer, Singapore (2018): 167-227. - Joana S. Sousa, Deryck J. Mills, Janet Vonck, and Werner Kühlbrandt. *Functional asymmetry and electron flow in the bovine respirasome.* eLife 5 (2016): e21290 - Joana S. Sousa, Afonso M.S. Duarte, Ana P. Batista and Manuela M. Pereira. *Insights into the antiporterlike subunits of respiratory Complex I*. BBA 1837 (2014) e1–e10. doi:10.1016/j.bbabio.2014.05.113 - Joana S. Sousa, Afonso M.S. Duarte, Ana P. Batista, Bruno C. Marreiros and Manuela M. Pereira. *Investigation of the dynamics of ion translocation subunits from respiratory complex I*. Eur Biophys J (2013) 42 (Suppl 1):S182. Communications: - Joana S. Sousa, Igor Tascón, Inga Hänelt and Janet Vonck. *Cryo-EM structure of a high-affinity potassium-proton symporter*. Cryo-EM in industry and academia. EMBL Heidelberg, Germany. February 6-8, 2019.

- Joana S. Sousa, Filipa Calisto, Deryck J. Mills, Patricia N. Refojo, Miguel Teixeira, Werner Kühlbrandt, Manuela M. Pereira and Janet Vonck. *Structural basis for energy transduction by respiratory alternative complex III.* Three dimensional electron microscopy conference GRC. Newport, RI, USA. June 3-8, 2018.

- Joana S. Sousa, Filipa Calisto, Deryck J. Mills, Patricia N. Refojo, Miguel Teixeira, Werner Kühlbrandt, Manuela M. Pereira and Janet Vonck. *Near-atomic structure of the Alternative Complex III from Rhodothermus marinus by single-particle cryo-EM*. Revolutions in structural biology: Celebrating the 100th anniversary of Sir John Kendrew. EMBL Heidelberg, Germany. November 16-17, 2017.

- Joana S. Sousa, Filipa Calisto, Deryck J. Mills, Patricia N. Refojo, Miguel Teixeira, Werner Kühlbrandt, Manuela M. Pereira and Janet Vonck. *Near-atomic structure of the Alternative Complex III from Rhodothermus marinus by single-particle cryo-EM*. EMBO practical course – Image processing for cryo-electron microscopy. Birkbeck University of London, UK. September 5-15, 2017.

- Joana S. Sousa, Filipa Calisto, Deryck J. Mills, Patricia N. Refojo, Miguel Teixeira, Manuela M. Pereira and Janet Vonck. *Near-atomic structure of the Alternative Complex III from Rhodothermus marinus by single-particle cryo-EM*. EBSA. Edinburgh, UK. July 16-20, 2017.

- Joana S. Sousa, Deryck J. Mills, Janet Vonck, and Werner Kühlbrandt. *Functional asymmetry and electron flow in the bovine respirasome.* Molecular Machines – EMBO. EMBL Heidelberg, Germany. November 20-23, 2016.

- Joana S. Sousa, Filipa Calisto, Deryck J. Mills, Patricia N. Refojo, Miguel Teixeira, Manuela M. Pereira and Janet Vonck. *Structural Investigation of the Alternative Complex III from Rhodothermus marinus by single particle cryo-EM*. EBEC. Riva del Garda, Italy. July 2-7, 2016.

- Joana S. de Sousa, Raquel J. Nunes, Isabel Monteiro Grillo and Susana Constantino. *Molecular mechanisms whereby low doses of ionizing radiation induce angiogenesis.* Molecular and Cellular Mechanisms in Angiogenesis. Capri (Naples), Italy. October 14-17, 2012.

- Joana S. de Sousa, Pedro Faísca, Inês S. Vala, Isabel Monteiro Grillo, Susana Constantino Rosa Santos. *Low doses of ionizing radiation enhance the invasiveness of cancer cells*. Hepatic Metastases-Clinic and Biology. Lisbon, Portugal. May 11-12, 2012.

- Joana S. de Sousa, Isabel Monteiro Grillo, Susana Constantino Rosa Santos. *Molecular mechanisms whereby low doses of ionizing radiation induce angiogenesis*. Hepatic Metastases-Clinic and Biology. Lisbon, Portugal. May 11-12, 2012.

- Joana S. de Sousa, Isabel Monteiro Grillo, Susana Constantino Rosa Santos. *Molecular mechanisms whereby low doses of ionizing radiation induce angiogenesis*. Advances in the cellular and molecular biology of angiogenesis. Birmingham, UK. June 27-29, 2011